

2011

Growth and Characterization of Carbon Nanomaterials

Jay Patel
Wright State University

Follow this and additional works at: https://corescholar.libraries.wright.edu/etd_all



Part of the [Physics Commons](#)

Repository Citation

Patel, Jay, "Growth and Characterization of Carbon Nanomaterials" (2011). *Browse all Theses and Dissertations*. 462.

https://corescholar.libraries.wright.edu/etd_all/462

This Thesis is brought to you for free and open access by the Theses and Dissertations at CORE Scholar. It has been accepted for inclusion in Browse all Theses and Dissertations by an authorized administrator of CORE Scholar. For more information, please contact library-corescholar@wright.edu.

GROWTH AND CHARACTERIZATION OF CARBON NANOMATERIALS

A thesis submitted in partial fulfillment
of the requirements for the degree of
Master of Science

By

JAY N. PATEL
B.S., WAKE FOREST UNIVERSITY, 2008

2011
Wright State University

**WRIGHT STATE UNIVERSITY
SCHOOL OF GRADUATE STUDIES**

March 6, 2011

I HEREBY RECOMMEND THAT THE THESIS PREPARED UNDER MY SUPERVISION BY Jay Patel ENTITLED Growth and Characterization of Carbon Nanomaterials BE ACCEPTED IN PARTIAL FULFILLMENT OF THE REQUIREMENT FOR THE DEGREE OF Master of Science.

Gregory Kozlowski, Ph.D.
Thesis advisor

Lok Lew Yan Voon, Ph.D.
Chair, Department of Physics
College of Science and Mathematics

Committee on
Final Examination

Jason Deibel Ph.D.

Jerry Clark, Ph.D.

Andrew Hsu, Ph.D.
Dean, School of Graduate Studies

ABSTRACT

Patel, Jay, M.S., Department of Physics, Wright State University, 2011.
Growth and Characterization of Carbon Nanomaterials.

In this thesis, single and multi-layered graphene films were epitaxially grown on either Si-face or C-face of SiC single crystal substrates. The film growth conditions, such as decomposition temperatures and pressures, and their surface morphologies were optimized. These films were then characterized by using surface analysis tools including SEM, TEM, AFM evanescent wave microscopy and electron energy loss spectroscopy. In addition to studying graphene decomposed from SiC crystals, carbon nanotube material was fabricated using a floating catalyst technique. These carbon nanotube material was then studied for potential cathode applications in this thesis. Field emission properties of these cathodes was measured and compared between carbon nanotubes grown by the floating catalyst technique and carbon nanotube material fabricated from a super acid solution spinning process. The result found that carbon nanotube material produced from the floating catalyst method supported the highest emission currents. As a result of this research, carbon nanotube field emitters fabricated from this method are now being studied in a wide range of vacuum electronic applications.

TABLE OF CONTENTS

CHAPTER 1: INTRODUCTION.....	1
1.1 CARBON NANOTUBE BACKGROUND.....	2
1.2 CARBON NANOTUBE SYNTHESIS.....	4
1.2.1 FLOATING CATALYST CNT MATERIAL.....	4
1.2.2 SUPER ACID SOLUTION SPINNING.....	5
1.2.3 DECOMPOSITION OF SIC.....	6
1.3 FABRICATION OF BULK CNT MATERIALS.....	8
CHAPTER 2: EVANESCENT MICROWAVE MICROSCOPY.....	12
2.1 EVANESCENT MICROWAVE MICROSCOPY THEORY.....	12
CHAPTER 3: FABRICATION OF CARBON NANOTUBE MATERIALS.....	16
3.1 UNIVERSITY OF CAMBRIDGE FLOATING CATALYST METHOD.....	16
3.1.1 EXTRACTION OF CNT FIBERS.....	18
3.1.2 EXTRACTION OF CNT MATS.....	22
3.2 CARBON NANOTUBE POST GROWTH TREATMENTS.....	26
CHAPTER 4: FABRICATION OF GRAPHENE FROM SIC.....	34
4.1 GROWTH FROM SIC.....	34
4.1.1 SURFACE IMPURITIES.....	34
4.2 SURFACE MORPHOLOGY CONTROL.....	37
4.3 PHYSICAL CHARACTERIZATION.....	42
4.3.1 TRANSMISSION ELECTRON MICROSCOPE ANALYSIS.....	42
4.3.2 ATOMIC FORCE MICROSCOPY.....	44
4.3.3 X-RAY DIFFRACTION.....	47
4.3.4 EVANESCENT MICROWAVE MICROSCOPY.....	50
4.4 ELECTRON BEAM INDUCED CURRENT SPECTROSCOPY.....	53

CHAPTER 5: FIELD EMISSION	59
5.1 THEORY OF FIELD EMISSION	59
5.2 PRINCIPLES OF THERMIONIC EMISSION	62
5.3 PRINCIPLES OF FIELD EMISSION	64
5.4 GEOMETRY EFFECTS	66
5.5 FIELD EMISSION RESULTS	69
CHAPTER 6: CONCLUSION.....	82
REFERENCES.....	85

LIST OF FIGURES

Figure 1. Schematic of how graphene can be rolled into various chiralities of CNTs [1].	2
Figure 2. Visual representation of CNT defining chirality vector \mathbf{C} and translation vector \mathbf{T} .	3
Figure 3. Illustration of vertical CVD and two CNT material collection techniques. (A) Extraction of fiber and (B) extraction of highly aligned film [15].	5
Figure 4. Schematic of a traditional Super Acid Solution Spinning Layout [8].	6
Figure 5. Growth mechanisms of CNT material from decomposition of SiC [5].	7
Figure 6. SEM images of CNT material from decomposition of SiC [13].	7
Figure 7. Resistance vs. temperature of MWNT fiber.	9
Figure 8. Schematic of evanescent microwave microscope system.	12
Figure 9. Diagram of image charge problem.	14
Figure 10. Cambridge furnace. (A) Feed system control, (B) vertical furnace tube and (C) collection area.	16
Figure 11. Chemical reaction to form CNT.	17
Figure 12. (A) Spinning spindle used to collect CNT material from Cambridge furnace. (B) Densification process of CNT directly from Cambridge furnace [23].	18
Figure 13. SEM of uncondensed and condensed fibers [16].	19
Figure 14. Optical time lapse of densification of CNT fiber when in contact by acetone.	19
Figure 15. Two fibers that are twisted and condensed using acetone.	20
Figure 16. SEM micrograph of two twisted together fibers.	21
Figure 17. Live picture of fiber collection to a spinning mandril.	22
Figure 18. SEM of carbon nanotube mats made from Cambridge CVD process. High levels of iron can be easily seen in SEM image.	23
Figure 19. SEM of carbon nanotube mats made from Cambridge CVD process. High levels of iron can be easily seen in SEM image.	24
Figure 20. SEM of carbon nanotube mats made from Cambridge CVD process. High levels of iron can be easily seen in SEM image.	25
Figure 21. SEM of carbon nanotube mats made from Cambridge process. Cluster ball in the image is residual iron catalysts.	26
Figure 22. Resistance vs. temperature measurement of Cambridge fiber.	27
Figure 23. Schematic of a four probe setup.	28
Figure 24. PPMS measurement resistance vs. temperature of Cambridge fiber.	28
Figure 25. Optical characterization set-up.	29
Figure 26. Evanescent microwave microscopy (A,B) and optical measurements of CNT film in designated area "1-3".	30
Figure 27. Evanescent microwave microscopy (A,B) and optical measurements of CNT film in designated area "2-3".	31
Figure 28. Evanescent microwave microscopy (A,B) and optical measurements of CNT film in designated area "1-5".	32
Figure 29. AFM of C-face (A) and Si-face (B) of RCA treated SiC wafers.	35
Figure 30. Mass current flow on SiC during sublimation.	36
Figure 31. Illustration of terraces and step heights.	36
Figure 32. AFM of SiC surface depicting step-bunching.	37

Figure 33. OxyGon furnace at AFRL.	38
Figure 34. Tungsten heating elements.	39
Figure 35. Pictures of CMP.	41
Figure 36. Possible planarization can be accomplished by CMP.	42
Figure 37. TEM of decomposed SiC at various annealing temperatures.	43
Figure 38. Cross-section of CNT decomposed from SiC wafer [13].	44
Figure 39. AFM of graphene on SiC without CMP treatment at various annealing temperatures (2 μm x 2 μm).	45
Figure 40. Comparison between non-CMP and CMP treated wafer (2 μm x 2 μm).	46
Figure 41. AFM showing increase of graphene thickness as a function of dwell time.	46
Figure 42. SiC Si-face after annealing at 1700°C for 30 minutes.	48
Figure 43. SiC Si-face after annealing at 1700°C for 60 minutes.	49
Figure 44. Si-face after annealing at 1700°C for 120 minutes.	50
Figure 45. Q-factor plots of graphene - CNT boundary.	52
Figure 46. Schematic of EBIC system.	54
Figure 47. Traditional SEM of graphene in four-probe set-up.	55
Figure 48. EBIC (A) and SEM (B) image of the same area.	56
Figure 49. EBIC (A) and SEM (B) image of the same area.	57
Figure 50. EBIC (A) and SEM (B) image of the same area.	58
Figure 51. Electron in front of conducting plane e^- is mirrored by the image charge e^+ . Distance between two image charges from the conducting surface is the same.	60
Figure 52. (A) Potential $U(x)$ as a function of position from the surface and (B) Fermi-Dirac distribution as a function of energy.	62
Figure 53. Potential barrier field emission (A) without and (B) with an imposed electric field. .	64
Figure 54. 2-D absolute E-field values for three different geometries. (A) Flat rectangular surface, (B) curved surface of radius R, and (C) cone.	68
Figure 55. Schematic of field emission chamber set-up.	69
Figure 56. Field emission of CNT film [20].	70
Figure 57. SEM of CNT film grown at 1700°C under 10^{-3} Torr for 3 hours [20].	70
Figure 58. Image of SWNT fiber mounted on a graphite puck.	72
Figure 59. SWNT Rice fiber in field emission chamber. The fiber is placed about 500 μm from anode.	73
Figure 60. Voltage vs. time of SWNT Rice fiber test with a 500 μm gap distance.	74
Figure 61. Field emission current vs. time of SWNT Rice fiber test a 500 μm gap distance.	74
Figure 62. MWNT Cambridge fiber in field emission chamber. The fiber is placed about 650 μm from anode.	75
Figure 63. Voltage vs. time of MWNT Cambridge fiber test with a 650 μm gap distance.	76
Figure 64. Field emission current vs. time of MWNT Cambridge fiber test with a 650 μm gap distance.	76
Figure 65. MWNT Cambridge fiber in field emission chamber. The fiber is placed about 815 μm from anode.	77
Figure 66. Voltage vs. time of MWNT Cambridge fiber test with a 815 μm gap distance.	78
Figure 67. Field emission current vs. time of MWNT Cambridge fiber test with a 815 μm gap distance.	78

Figure 68. Current vs. time of MWNT Cambridge fiber field emission 615 μm at 1000 V. 79
Figure 69. Current vs. time of MWNT Cambridge fiber field emission 815 μm at 1000 V. 79
Figure 70. SEM of MWNT Cambridge fiber. (A) Fiber tip after mechanical clipping and (B)
alignment of CNTs in fiber. 80
Figure 71. Live images of field emission process..... 81

LIST OF TABLES

Table I. Solution spinning fiber performance parameters.	10
Table II. Solid state spinning performance parameters.	10
Table III. Comparison of work function and ionizations for various metals and metal surfaces [9].	61

ACKNOWLEDGEMENTS

It is truly impossible to complete this effort alone. There are many people who helped me accomplish this work and are due my heartfelt thanks. To my advisor and friend Professor Gregory Kozlowski for his endless guidance and never ending enthusiasm throughout my studies, I truly look forward to work with him outside of Academia for many more years to come. Also, to Dr. Jason Deibel, for his patience and advice over the years. In addition, to Dr. Krzysztof Koziol for welcoming me to his research group. To all the friends that I have made at AFRL especially Dr. John Boeckl. Lastly, to all the Professors at Wright State who have helped me along the way.

I would also like to express my sincerest gratitude to my classmates at Wright State. I have learned much and their help and support is truly appreciated.

CHAPTER 1: INTRODUCTION

As the transition is made towards the incorporation of nanomaterials in devices, specific challenges have been identified in the fabrication processes of these materials. The lack of precise, repeatable fabrication methods resulting from lack of understanding and control of growth mechanisms at an atomic scale has hindered the commercial uses of nanomaterials. Sensitivity to growth condition variations makes bulk manufacturability an issue that must be overcome. The goal of this thesis is to understand growth mechanisms to drive efforts of achieving single atomic layer growth and translate this control to increased bulk material quality. By addressing initial surface conditions as well as chamber conditions, recipes for carbon nanomaterials fabrication are optimized in this thesis. These materials are then studied to correlate physical uniformity to their bulk electrical properties. By developing uniform nanomaterials, device performance can be maximized substantially.

One method of carbon nanomaterial growth is a decomposition process of SiC crystals. Decomposition of SiC has shown to result in carbon nanotube and/or graphene materials. SiC work presented in this thesis will primarily focus on graphene fabrication optimization. Effects of various decomposition variables of SiC will be studied and characterized in Chapter 4. The goal is to optimize conditions such that to develop a standardized process for accurate, precise and repeatable growths. Material characterization techniques such as evanescent microwave microscopy and electron beam induced current spectroscopy will be used to correlate structural homogeneity to electrical performance.

Along with studying graphene, carbon nanotube material from University of Rice's super acid solution process and carbon nanotube material from University of Cambridge's floating

catalysts methods will be studied. General background of carbon nanotube material and the fabrication processes of these materials will be discussed in subsequent sections of this Chapter.

1.1 CARBON NANOTUBE BACKGROUND

Since their discovery, there has been much interest in studying carbon nanotubes. Carbon nanotube structures can be thought up as rolled up sheets of graphene.

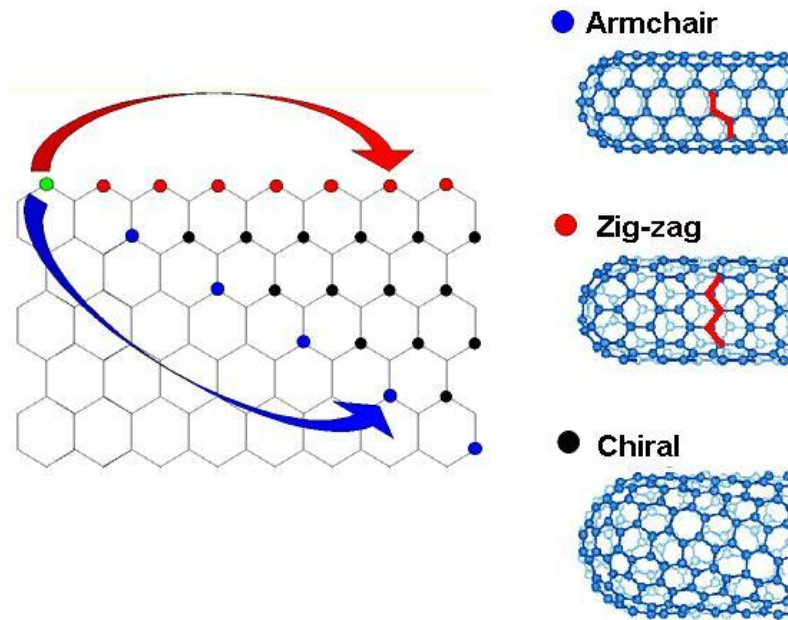


Figure 1. Schematic of how graphene can be rolled into various chiralities of CNTs [1]. Depending on how the graphene sheet is rolled, the tube can take on three possible structures or chiralities: armchair, zigzag or chiral. Chirality of the tubes plays an important role in the electric properties of the carbon nanotube (CNT); it dictates whether the tubes will act like a metal or a semiconductor or a combination of the two.

In Figure 1, green to blue connection will produce an armchair chirality, if the CNT is rolled green to red this will produce a zigzag, and if the CNT is rolled green to black this will

produce an intermediated zigzag. Single walled carbon nanotubes can be defined by introducing a Chiral Vector, \vec{C} , and a Translation Vector, \vec{T} , as shown in Figure 2.

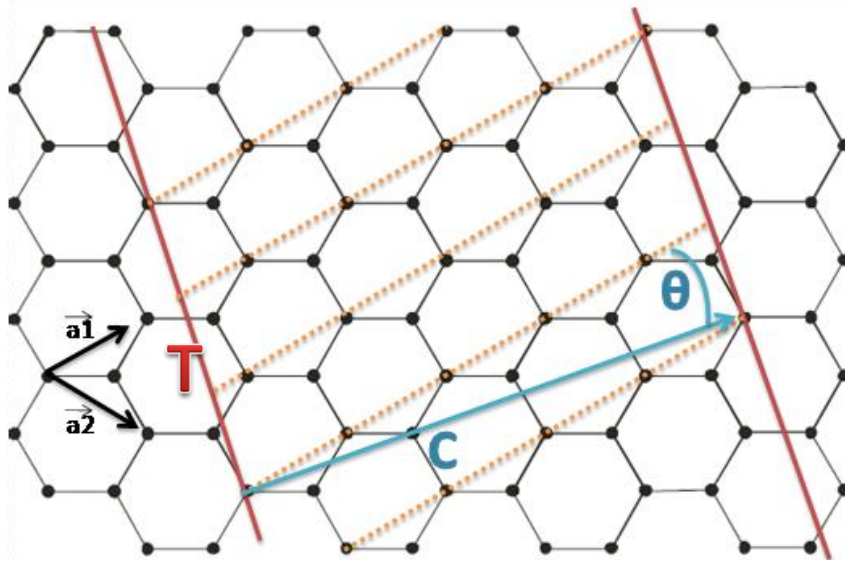


Figure 2. Visual representation of CNT defining chirality vector \vec{C} and translation vector \vec{T} .

The band gap energy can be related directly to the geometry of the Brillouin zone, therefore the energy spectrum of a single CNT can be related to the chirality and translation vectors. The physical folding of the CNT through this relationship is directly whether the CNT will be metallic or semiconducting in nature. This demonstrates the importance in studying the chirality whenever discussing fundamental electric properties of CNT [24,25,26].

1.2 CARBON NANOTUBE SYNTHESIS

After the initial discovery of CNTs, various fabrication processes to create bulk CNT materials have been explored. Laser ablation [2], arc discharge [3], solid state spinning from aligned CNT forests [4], floating catalyst chemical vapor depositions [5], super acid solution spinning [6] or various other material decomposition techniques [7] are just few techniques utilized to create carbon nanotube structures. Each of these methods has advantages and disadvantages and each process will create unique bulk CNT structures. Few of these growth techniques that pertain to this thesis will be discussed in the following sections.

1.2.1 FLOATING CATALYST CNT MATERIAL

The floating catalyst method is a form of solid state spinning using a special chemical vapor deposition (CVD) process. Typically, a CVD process consists of mixing a carbon source gas, iron catalyst and growth promoters together inside a CVD chamber's heat zone around 1000°C-1200°C in the presence of a carrier gas to create CNT material. Unlike a traditional CVD process, the CNTs do not grow and align themselves on a substrate but rather grow in a hot vapor pocket called an aerogel pocket.

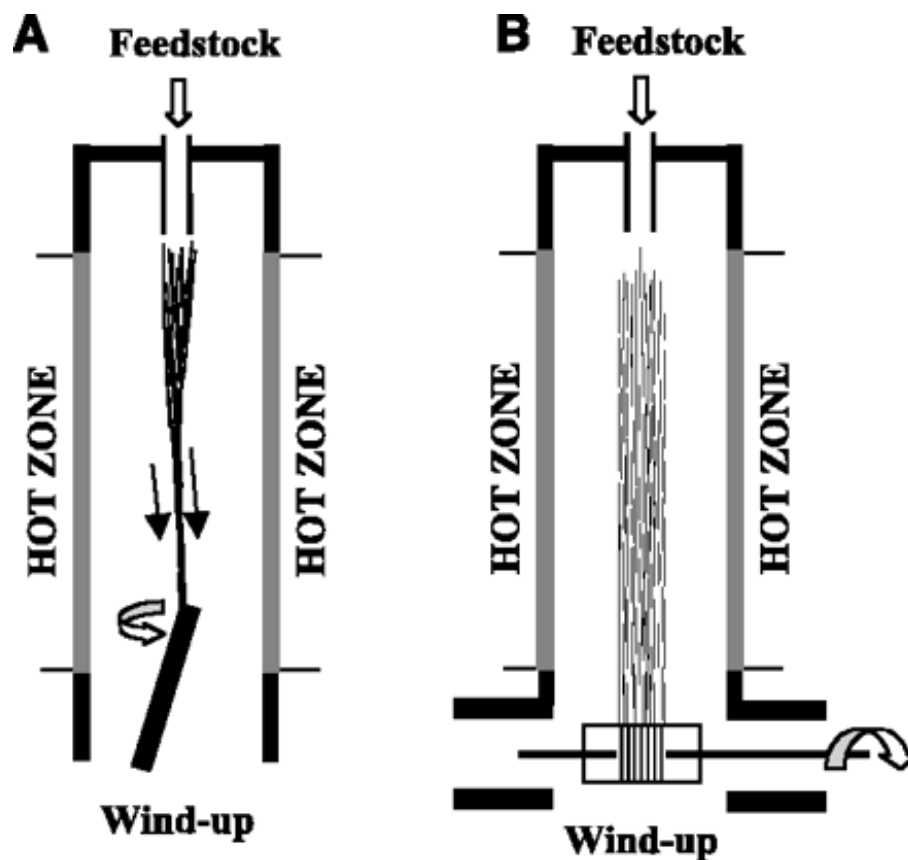


Figure 3. Illustration of vertical CVD and two CNT material collection techniques. (A) Extraction of fiber and (B) extraction of highly aligned film [15].

Figure 3 is an example of a vertical CVD furnace, liquid feedstock is fed into the system creating an aerogel inside the heat zone. The aerogel is captured and wound out of the hot zone continuously as a fiber or film. In Figure 3A, wind up is done by rotating spindle, resulting in a CNT fiber, versus Fig.3B where the aerogel is collected by a rotating winder creating a highly aligned film.

1.2.2 SUPER ACID SOLUTION SPINNING

The super acid solution spinning process such as the one utilized by Rice University [8], produces SWNT fibers using conventional spinning techniques with rigid rod polymers. The process uses SWNTs produced by using a HiPco process, which are washed and purified by a

acid wash to remove excess of metal catalysts. These purified SWNT are then suspended in solution of sulfuric acid, which is then loaded into a syringe. The SWNT acidic solution is then extruded through a small capillary tube creating a SWNT fiber, which is wound on a rotating stage.

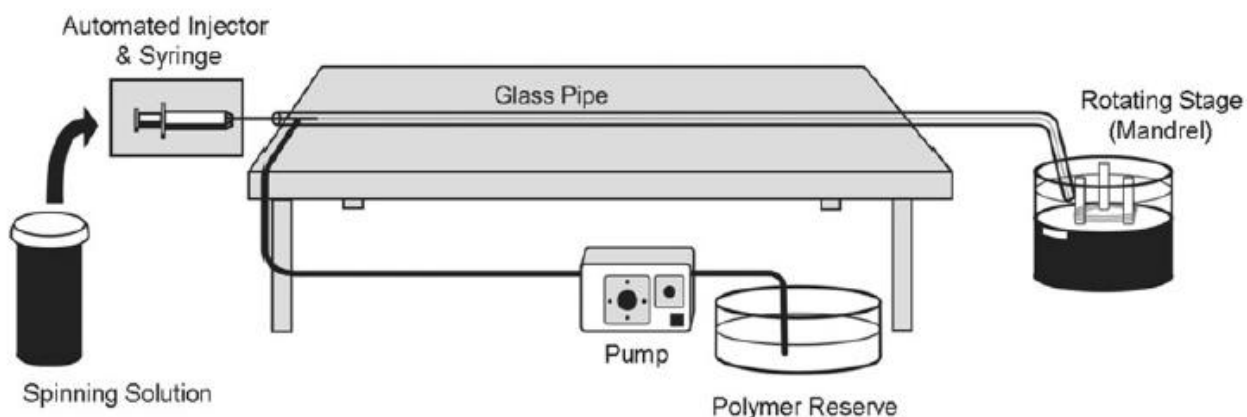


Figure 4. Schematic of a traditional Super Acid Solution Spinning Layout [8].

This process can create a limited range of fiber diameters, less than 100 μm . However, this process is able to create very densely packed SWNT fibers that are free from iron catalysts.

1.2.3 DECOMPOSITION OF SiC

The formation of tightly packed and vertically aligned multi-walled carbon nanotubes (MWNTs) has been observed after annealing SiC wafers at high temperatures (1200°C – 1700°C) and at pressures ranging from 10^{-3} Torr to 10^{-5} Torr. Specifically, these CNTs lack the presence of catalyst metals, regarded as an impurity, which can be difficult and costly to remove. Though the decomposition is not fully understood, one of the current theories in decompositions is illustrated in Figure 5. In Figure 5A, around 1000°C sheets of graphene form parallel to the SiC surface, as the temperature is increased Si decomposing from the surface forms bubbles that

pushes the graphene sheets upwards. The graphene sheets then are bent outward in SiC (001) plane and the CNTs growth inward towards the center for the SiC as Si evaporates.

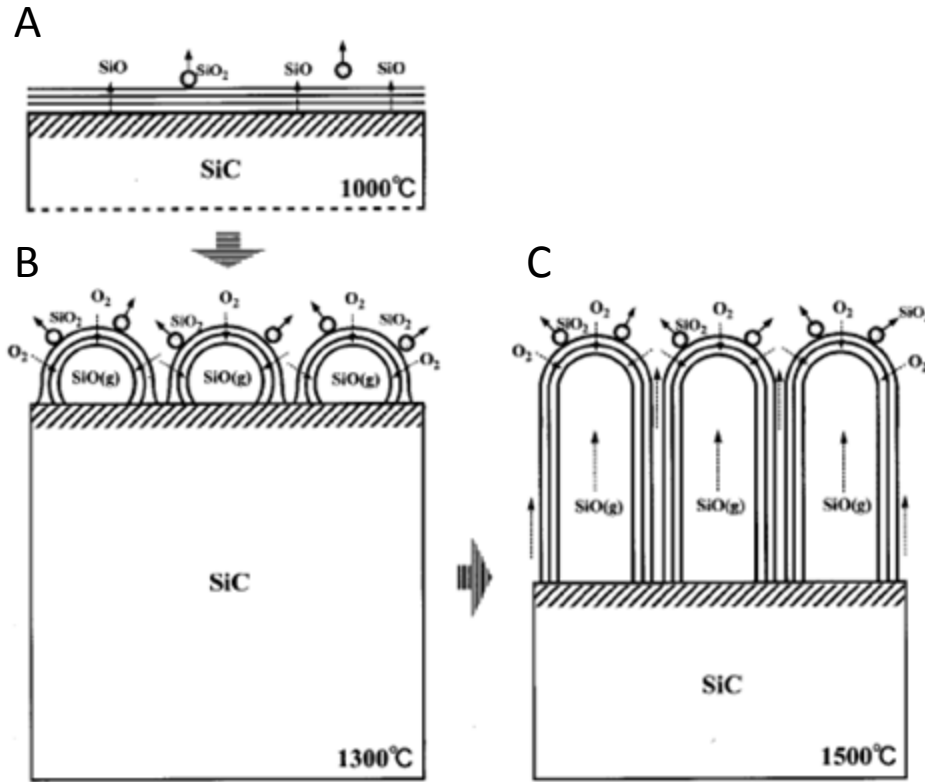


Figure 5. Growth mechanisms of CNT material from decomposition of SiC [5].

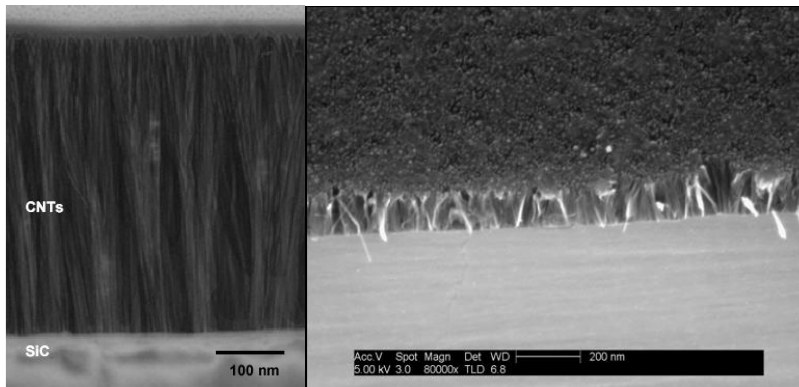


Figure 6. SEM images of CNT material from decomposition of SiC [13].

1.3 FABRICATION OF BULK CNT MATERIALS

The quality and performance of CNT material is highly dependent on the synthesis techniques. Moreover, when creating bulk macrostructures from these nanomaterials, distribution, alignment and uniformity will drastically alter the mechanical and electrical properties of the material. Theoretically, a single CNT has physically properties much different than their bulk counterparts. Literature has shown that taking the same SWNT material and forming thick carbon mats versus bundles the resistance and other their properties are going to be drastically changed. This drastic change is attributed to various vacancy defects, interconnections and tangled regions of CNTs [22].

Also, when creating bulk materials it is not guaranteed that all CNTs are identical as far as chirality is concerned. If chirality is not controlled, as pointed out earlier, the carbon nanotubes in bulk form could be either semiconducting or metallic in nature. The goal of any nanotube growth is accuracy and repeatability. Furthermore, combining unlike material into a single macroscopic structure will create irregular performance. It has been shown[18] by taking resistance vs. temperature measurements of bulk CNT fibers where the same material could have both metallic and semiconducting properties.

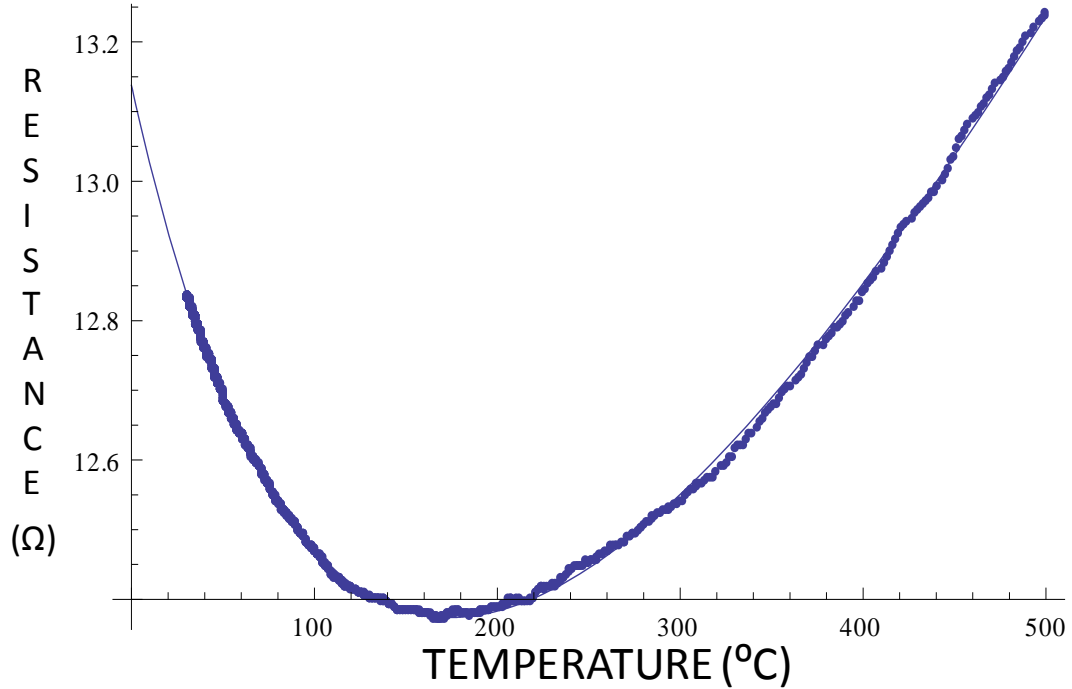


Figure 7. Resistance vs. temperature of MWNT fiber.

This measurement was fitted to the equation

$$\rho(T) = \alpha T + \rho_0 e^{-\beta T} \quad (1)$$

The first term in Equation 1, represents a metallic term and the second corresponds to fluctuations induced tunneling between metallic regions. In metals, as temperature is increased the number of inter ballistic collisions increases therefore increasing the metal's resistivity. In semiconductors, as temperature is decreased the resistance of the material increases. Figure 7 shows a measurement of resistance as a function of temperature, if the MWNT fibers acted only as a semiconductor or a metal, resistance will not have local minimum. Since there is a local minimum, it can be extracted that the MWNT exhibits a combination of metallic and semiconducting properties. The α and β in Equation 1 are material dependent constants. This measurement shows a MWNT without chirality control will both as a metal or a semiconductor.

Chirality is only example of the lack of control during the nanomaterials fabrication process. There are many variables that go into creating CNTs and even larger number of variables that go into creating bulk materials. Some properties of materials grown using solution spinning and solid-state spinning are listed in Table I and Table II.

Table I. Solution spinning fiber performance parameters.

Solution Spinning								
Spinning Technique	Type	Length	Diameter		Modulus (GPa)	Strength (GPa)	Toughness (J/g)	Electric Resistivity (mΩ X cm)
Surfactant dispersion coagulated in water	SWNT	< 1μm	~ 1 nm	as-spun	15	0.15	2.25	10
stretched				40	23	0.82		
annealed				-	-	-		
stretched				80	1.8	570		
Surfactant dispersion coagulated in ethanol				as-spun	2	0	-	150
Surfactant dispersion coagulated in acid or base				as-spun	12	0.065	-	150
Sulfuric acid dispersion coagulated in water	SWNT	<1μm	~1nm	annealed	120	0.116	-	0.2

Table II. Solid state spinning performance parameters.

Solid State Spinning								
Spinning Technique	Type	Length (μm)	Diameter (nm)		Modulus (GPa)	Strength (GPa)	Toughness (J/g)	Electric Resistivity (mΩ X cm)
Gas-Phase CVD	MWNT	30	30	as-spun	-	0.1-1	-	0.12
	DWNT	1000	10	vapor	78	1.3	13	0.2
	MWNT	100	10	twisted	5-30	150-460	11-20	3.3
	MWNT	650	10		275	275	-	5.8
Vertical grown CNT Array	MWNT	-	5-15	methanol	37	37	13	0.2

For electrical studies, the most important property of interest is the electric resistance. The rows highlighted in blue reflect Rice SWNT (Solution Spinning) and Cambridge MWNT (Solid State Spinning) fiber properties, respectively.

Before the optimization of fabrication processes of the carbon nanotube and graphene material are discussed, it is important to discuss the characterization techniques used to analyze these materials. Chapter 2 will discuss a unique measurement system that exploits near field interactions to extract material parameters such as conductivity, and permittivity.

CHAPTER 2: EVANESCENT MICROWAVE MICROSCOPY

2.1 EVANESCENT MICROWAVE MICROSCOPY THEORY

A non-destructive way to measure local complex permittivity parameters is evanescent microwave microscopy [19]. Using a perturbation technique, the local properties of a sample near microscope tip can be extracted by analysis the frequency shift of the evanescent wave. Using a network analyzer, a signal is generated and coupled to a coaxial transmission line which ends in a sharpened tip. The transmission line acts as a quarter resonator and is able to generate evanescent waves in the near field. When the transmission line is placed near a conductive or dielectric material, there is a perturbation in the resonance of the transmission line. The frequency and quality factor perturbation is measured which then is correlated to material parameters.

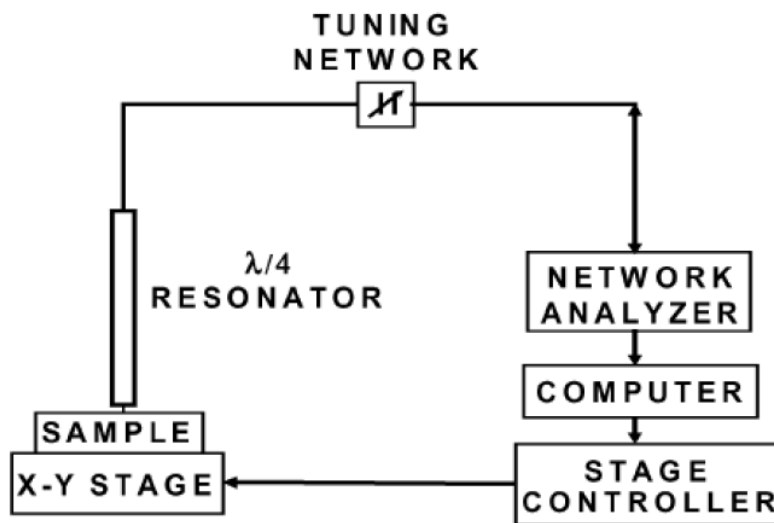


Figure 8. Schematic of evanescent microwave microscope system.

Figure 8 represents is a simple schematic of the evanescent microwave system at Wright State University Physics Department. The theory behind this system is a potential perturbation. Suppose the probe tip has a certain known potential, V_o . When the probe is moved close to the sample under test, charges on the probe will induce a polarization response in the sample. This interaction induces a frequency shift in the resonator (probe). The frequency perturbation can be equated in terms of physical properties using Maxwell's equations. First by taking the difference of two pairs of modified Maxwell's equations respectively where $[E_o, H_o, \omega_o]$ represent the original resonator fields and $[E, H, \omega]$ represent perturbed parameters

$$\mathbf{E}^* [\nabla \times \mathbf{H} = i\omega(\epsilon + \Delta\epsilon)\mathbf{E}] \quad (2)$$

$$\mathbf{E}[\nabla \times \mathbf{H}_o = i\omega_o\mathbf{E}_o] \quad (3)$$

$$\mathbf{H} [\nabla \times \mathbf{E}_o = -i\omega_o\mu\mathbf{H}_o]^* \quad (4)$$

$$\mathbf{H}^*[\nabla \times \mathbf{E} = -i\omega(\mu + \Delta\mu)\mathbf{H}] \quad (5)$$

and exploiting the vector identity of $\vec{\nabla} \cdot (\vec{A} \times \vec{B}) = \vec{B} \cdot (\vec{\nabla} \times \vec{A}) - \vec{A} \cdot (\vec{\nabla} \times \vec{B})$, Equation (4) and (2) will read,

$$\nabla(\mathbf{E}_o^* \times \mathbf{H}) = i\omega_o\mu\mathbf{H}\mathbf{H}_o^* - i\omega(\epsilon + \nabla\epsilon)\mathbf{E}_o^*\mathbf{E} \quad (6)$$

Using the same vector identity, Equation (3) and (5) will read,

$$\nabla(\mathbf{E} \times \mathbf{H}_o^*) = i\omega\epsilon\mathbf{E}\mathbf{E}_o^* - i\omega(\mu + \nabla\mu)\mathbf{H}_o^*\mathbf{H} \quad (7)$$

Taking Equation (6) and (7), the divergence theorem can be written as

$$\int \nabla(\mathbf{E}_o^* \times \mathbf{H} + \mathbf{E} \times \mathbf{H}_o^*) dV = \oint (\mathbf{E}_o^* \times \mathbf{H} + \mathbf{E} \times \mathbf{H}_o^*) dS = 0 \quad (8)$$

$$0 = i \int \{[\omega_o\epsilon - \omega(\epsilon + \Delta\epsilon)]\mathbf{E}_o^*\mathbf{E} + [\omega_o\mu - \omega(\mu + \Delta\mu)]\mathbf{H}_o^*\mathbf{H}\} dV \quad (9)$$

Since $\omega = 2\pi f$ and $\omega_o = 2\pi f_o$ the relationship can be made in terms of frequency

$$\frac{\Delta f}{f_o} = \frac{f - f_o}{f_o} = \frac{\int [(\Delta\epsilon)(\mathbf{E}_o^*\mathbf{E}) + (\Delta\mu)(\mathbf{H}_o^*\mathbf{H})] dV}{\int [\epsilon_o\mathbf{E}_o^2 + \mu_o\mathbf{H}_o^2] dV} \quad (10)$$

To complete Equation (10), the perturbed electric field has to be calculated. In Figure 9, a schematic for an image charge problem, and using cylindrical coordinates, is drawn and the potential a distance \mathbf{d} away from the tip can be calculated.

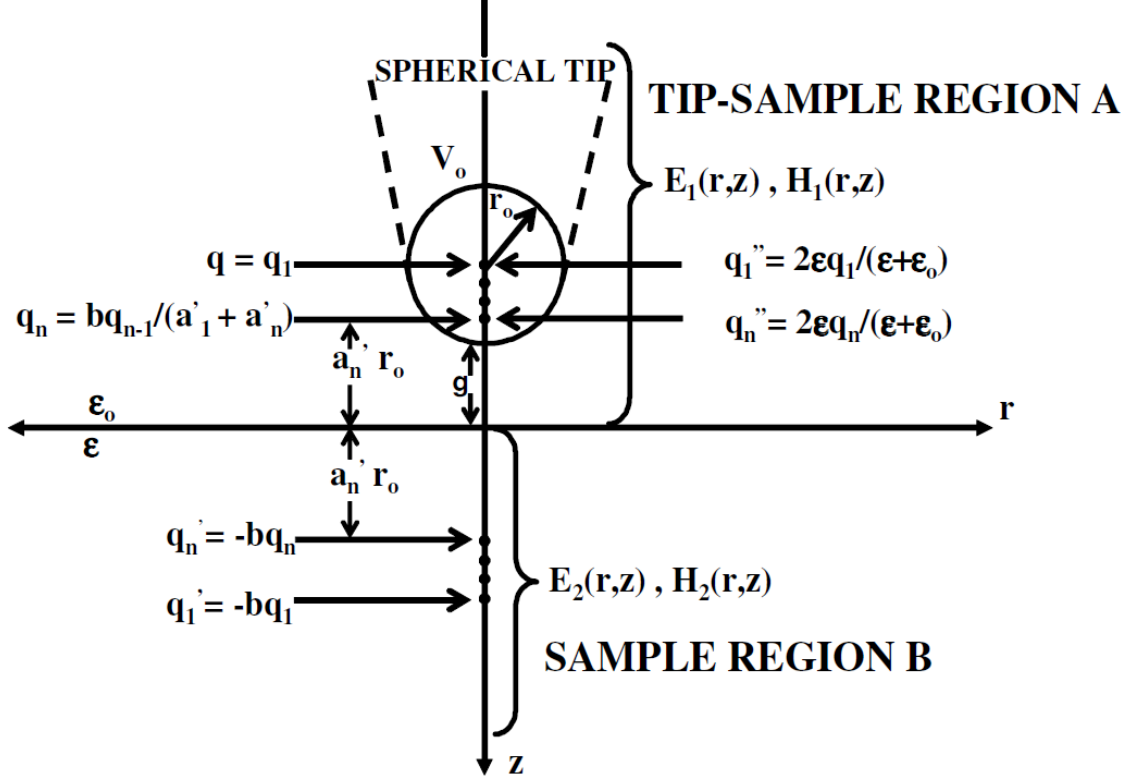


Figure 9. Diagram of image charge problem.

The potential is given by the equation

$$V(r, z) = \frac{1}{4\pi\epsilon_0} [d]^{-1/2} \quad (11)$$

where $\vec{\mathbf{d}}$, in cylindrical coordinates (r, θ, z) , is defined by $\vec{\mathbf{d}} = r\vec{\mathbf{r}} + (z + r_o + g)\vec{\mathbf{z}}$. Now that the perturbed electric fields using the method of images can be calculated as [21]

$$\mathbf{E}_1 = \frac{q}{4\pi\epsilon_0} \sum_{n=1}^{\infty} q_n \left\{ \frac{[r\hat{\mathbf{r}} + (z + a_n r_o)\hat{\mathbf{z}}]}{[r^2 + (z + a_n r_o)^2]^{3/2}} - b \frac{[r\hat{\mathbf{r}} + (z - a_n r_o)\hat{\mathbf{z}}]}{[r^2 + (z - a_n r_o)^2]^{3/2}} \right\} \quad (12)$$

$$\mathbf{E}_2 = \frac{1}{2\pi(\epsilon + \epsilon_0)} \sum_{n=1}^{\infty} q_n \left\{ \frac{[r\hat{\mathbf{r}} + (z + a_n r_o)\hat{\mathbf{z}}]}{[r^2 + (z + a_n r_o)^2]^{3/2}} \right\} \quad (13)$$

$$a_n = a_1 - \frac{1}{a_1 + a_{n-1}} \quad (14)$$

$$q_n = t_n q \quad (15)$$

$$t_n = \frac{t_{n-1} b}{a_1 + a_{n-1}} \quad (16)$$

$$b = \frac{\varepsilon - \varepsilon_0}{\varepsilon + \varepsilon_0} \quad (17)$$

where \mathbf{E}_1 and \mathbf{E}_2 represent the perturbed electric field in the tip-sample region and the sample volume, respectively. By using Equations (12) – (17), the total relative frequency shift can be determined

$$\left(\frac{\Delta f}{f_0}\right)_1 + \left(\frac{\Delta f}{f_0}\right)_2 = \sum_{n=1}^{\infty} t_n \left[1 - \frac{(1-b)}{2(a_1 + a_n)}\right] \quad (18)$$

This technique is a unique way to determine local properties of materials. Since evanescent waves are utilized, only the volume near the probe tip is active and therefore micron sized area of the sample can be measured. This is particular useful studying CNT fibers and tapes because evanescent spectroscopy will give localized properties of the material.

CHAPTER 3: FABRICATION OF CARBON NANOTUBE MATERIALS

3.1 UNIVERSITY OF CAMBRIDGE FLOATING CATALYST METHOD

The floating catalyst vertical CVD process is the trademark CNT fabrication process used by Windle's and Koziol's Research Group at the Materials Science Department of Cambridge University. Their bulk CNT fibers have been widely published [14,23]. Notable features of their CNT materials are their strong mechanical properties including their ability to extract continuous uniform fibers from their vertical CVD furnace.

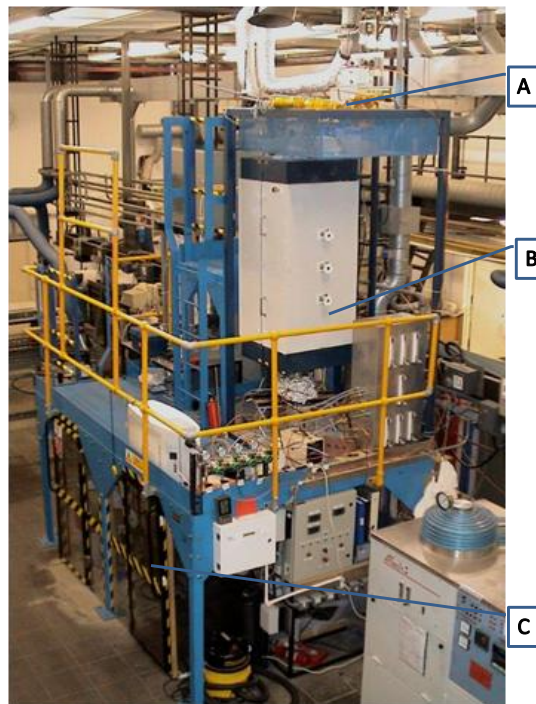


Figure 10. Cambridge furnace. (A) Feed system control, (B) vertical furnace tube and (C) collection area.

Even though most CVD furnaces are horizontal, Cambridge uses a vertical two-story split level CVD furnace. The top consists of reaction chamber and feed network, the bottom is a collection zone area. Figure 10A points to the top unit which controls the feedstock, gas rates and temperature during the growth. (B) is pointing to the large alumina reinforced quartz tube which

acts very similar to any CVD heat zone. This heat zone is open on the top for feedstock input and the other end is open and leads to a small enclosed room labeled by (C). In this room, collection of CNT material from the heat zone is made.

The composition of the feedstock is very important to CNT product. The fibers are produced from a liquid feedstock of 1.8/.25/97.95 wt % of ferrocene/thiophene/ethanol injected into the reactor at a rate of 6 mL/h (Figure 10). This is injected into the reactor around 1300 °C coupled with a hydrogen flow rate of about 2.5 L/min. Even though many scientific groups have published extensively on their fibers, they have only recently been able to use ethanol as a liquid carbon source.

Iron in the form of ferrocene, plays a very important role in the synthesis process and must be present in the correct amount and particle size for carbon nanotubes nucleation to occur. If too much is present, the tubes will have very irregular diameters and if too little is present the carbon will simply not form homogeneous structures.

The addition of sulfur and thiophene is used in the feedstock which is an unconventional addition. Sulfur enhances the catalytic properties of the iron in the feedstock and results in CNT materials with longer lengths in comparison to material growth without sulfur.

Needless to say, the carbon source is crucial in the feedstock. The carbon source plays an important role of a stabilizer in creating the feedstock made out of the iron and sulfur. Various carbon sources have been used, such as hexane, ethanol and methanol in the past.

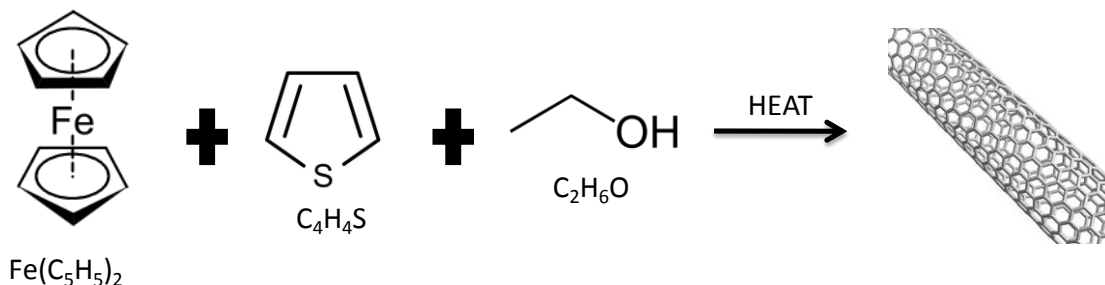


Figure 11. Chemical reaction to form CNT.

3.1.1 EXTRACTION OF CNT FIBERS

Using this CVD process, multiple types of bulk CNT material can be extracted. The aerogel pocket of CNT material in the reactor can be pierced by a mechanical arm which is used to draw CNT material out. The temperature difference of the mechanical arm and the aerogel sock will attract the CNT material to the arm end. If done under the right conditions, this process will extract a single continuous fiber consisting of densely packed highly oriented CNTs. This fiber can then be further condensed and spun by a rotating spindle (Figure 12).

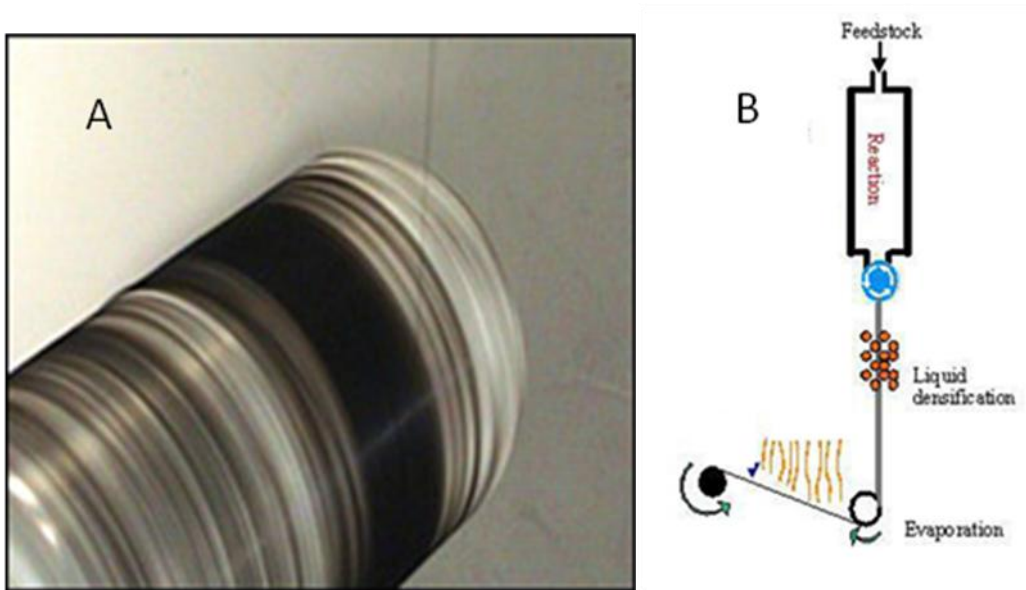


Figure 12. (A) Spinning spindle used to collect CNT material from Cambridge furnace. (B) Densification process of CNT directly from Cambridge furnace [23].

These fibers can be further densified by using acetone to create an ultra dense fiber. It has been shown in literature that when in contact with liquids CNT fibers will collapse upon themselves to create ultra dense fibers. Studies performed by Koziol et al., [16] have shown in a matter of seconds with contact of acetone that Cambridge fibers will condense to a fraction of the size (Figure 13 and Figure 14).

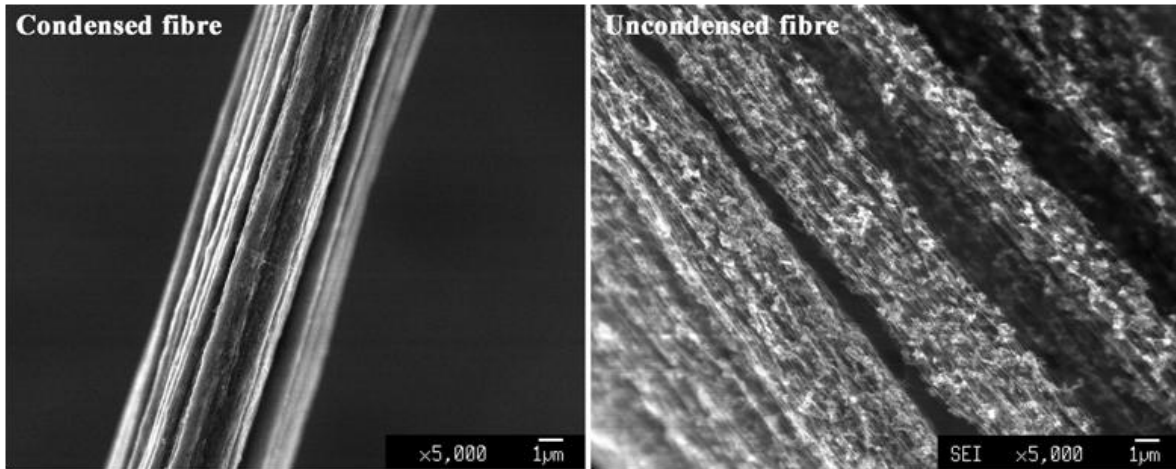


Figure 13. SEM of uncondensed and condensed fibers [16].

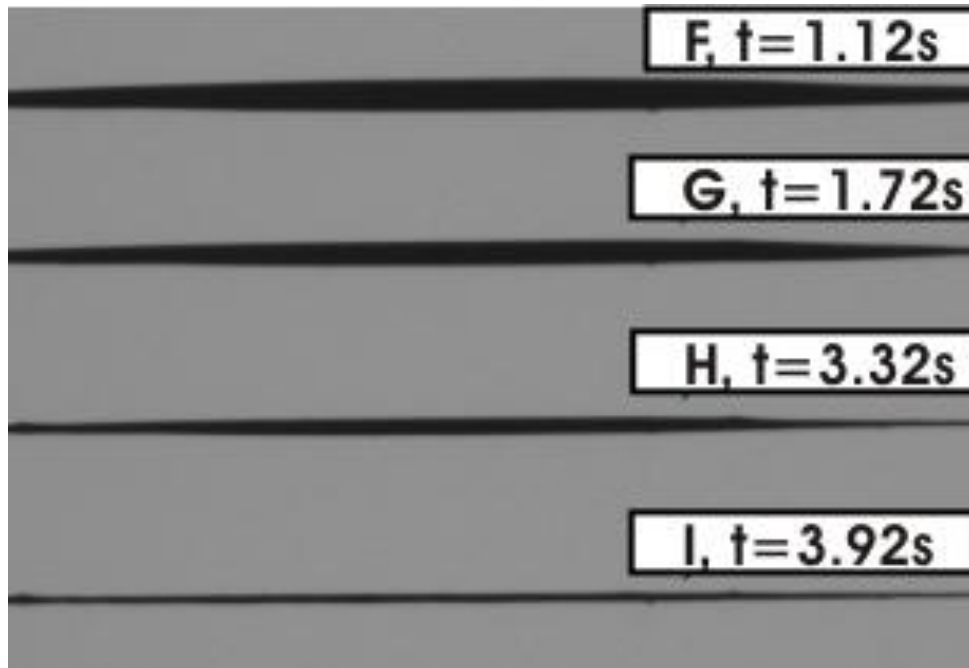


Figure 14. Optical time lapse of densification of CNT fiber when in contact by acetone.

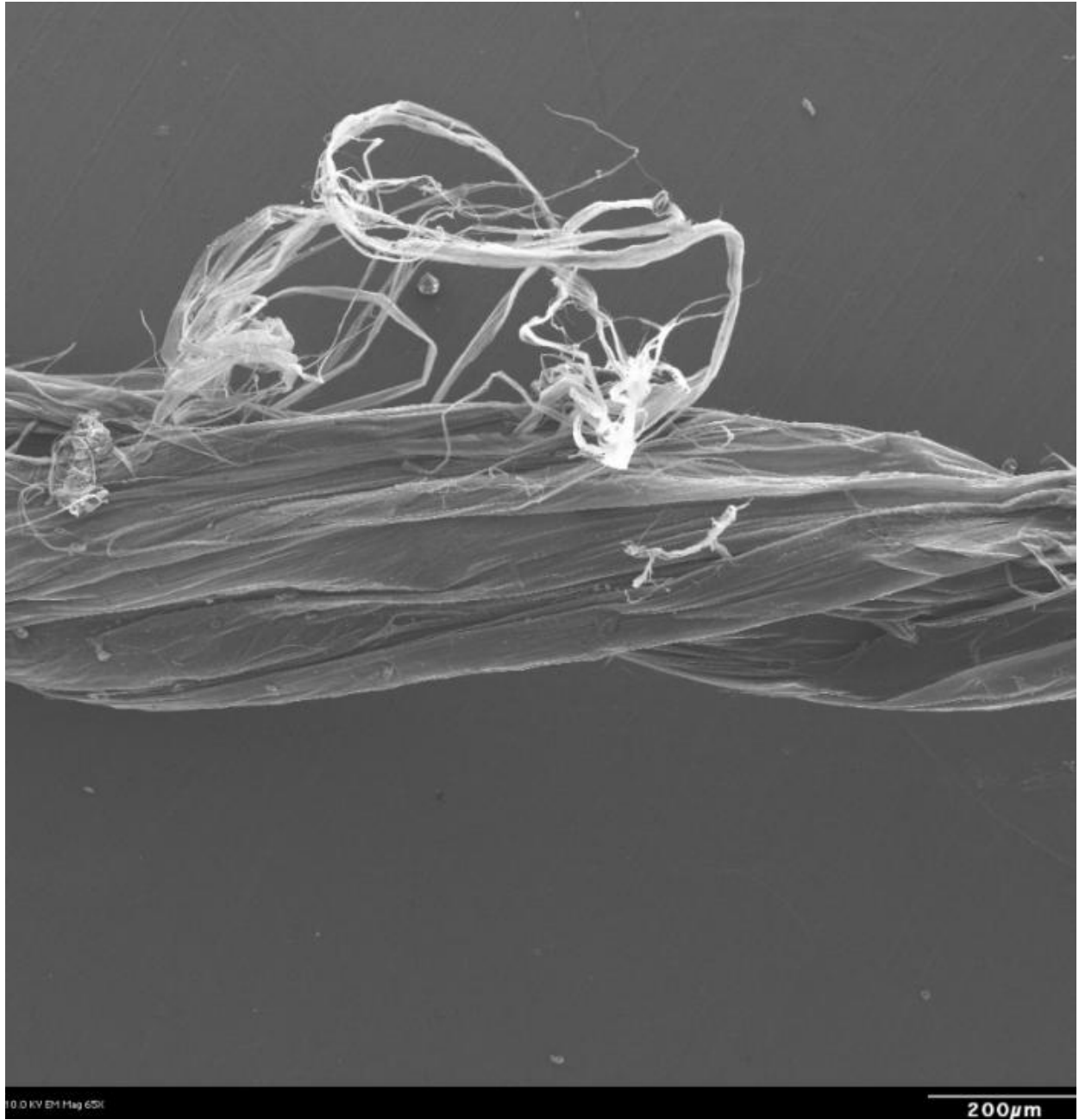


Figure 15. Two fibers that are twisted and condensed using acetone.

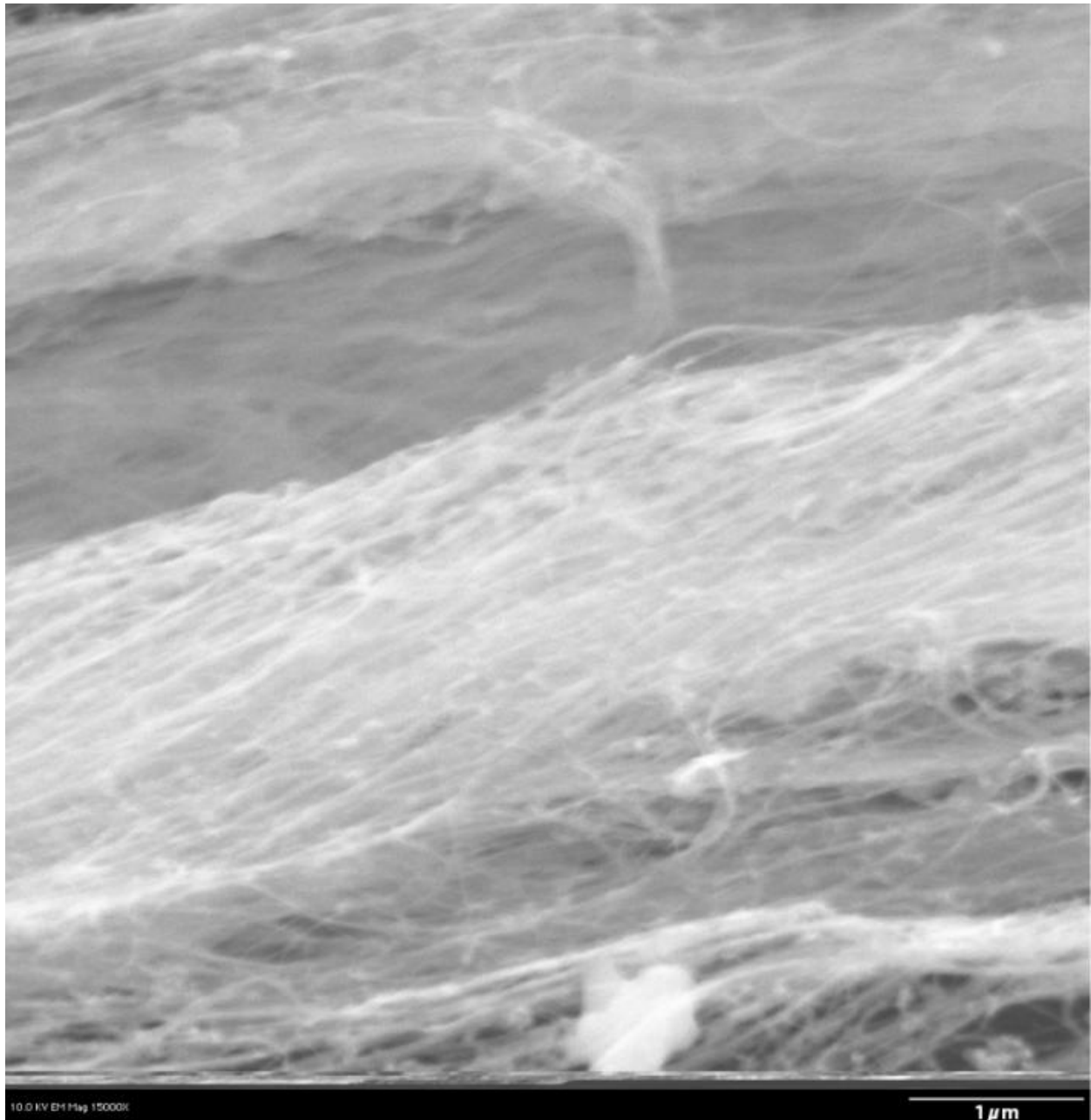


Figure 16. SEM micrograph of two twisted together fibers.

Since these fibers are liquid spun, the fibers are highly flexible and not prone to be brittle. Multiple fibers can be spun together (Figure 15) and condensed to create higher order macroscopic forms. This technique is used when fibers of large radius need to be made.

3.1.2 EXTRACTION OF CNT MATS

Instead of using a mechanical arm, a horizontal spindle can be placed right below the furnace's heat zone. Now instead of using a mechanical arm, hydrogen gas flows down the chamber at an increased rate and the aerogel over time will slowly leak out of the bottom and begin to coat the horizontal spindle. Though this process does not create highly aligned material, it can be used to coat thin film of CNT material over large areas (Figure 17).

Using this method, increased level of hydrogen is introduced to the system, which under high concentration could be combustible. To compensate, ferrocene concentration is slightly increased. This tends to result in higher concentration of residual iron catalysts in the final material (Figure 18, Figure 19, Figure 20, Figure 21).



Figure 17. Live picture of fiber collection to a spinning mandril.

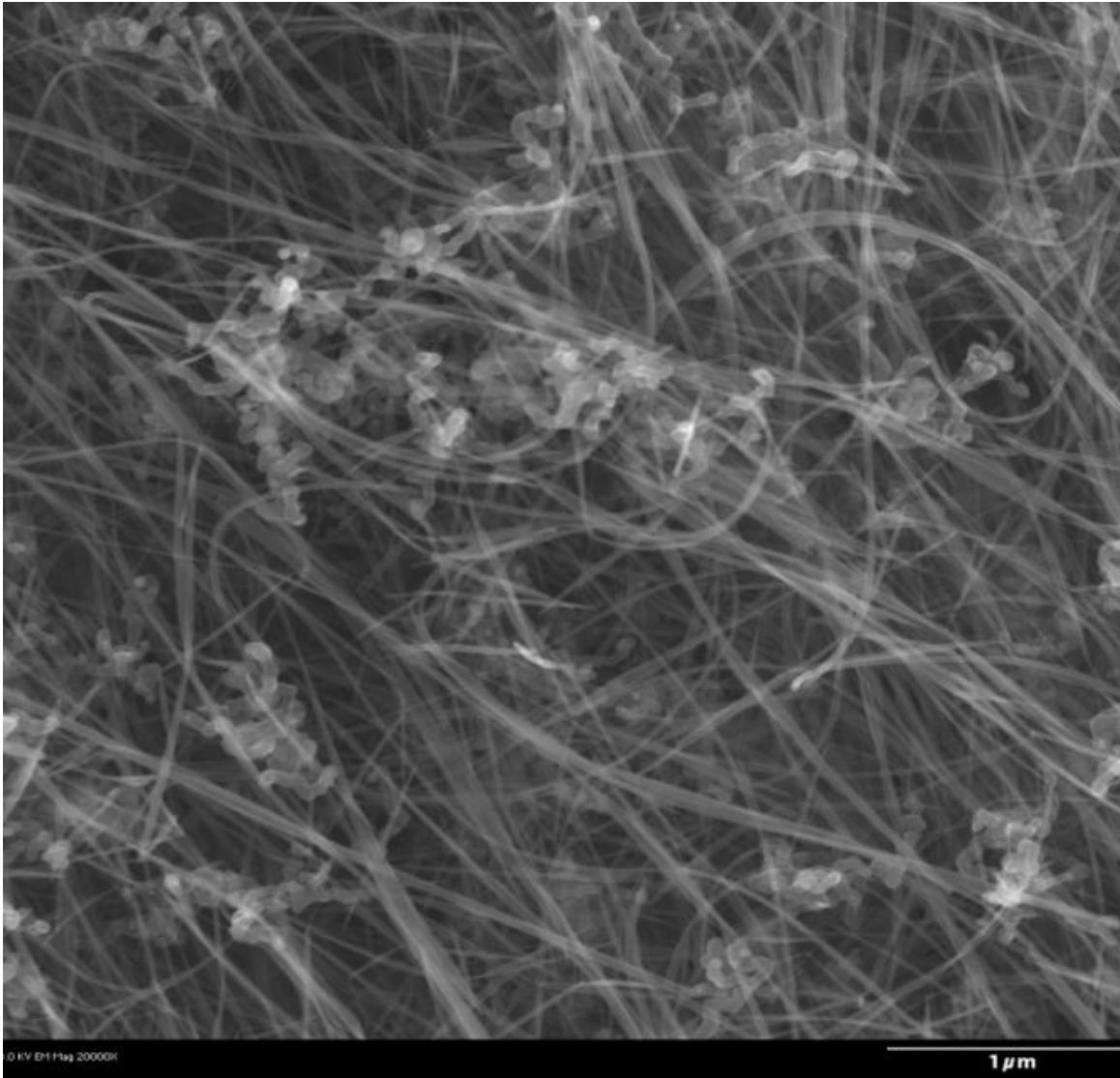


Figure 18. SEM of carbon nanotube mats made from Cambridge CVD process. High levels of iron can be easily seen in SEM image.

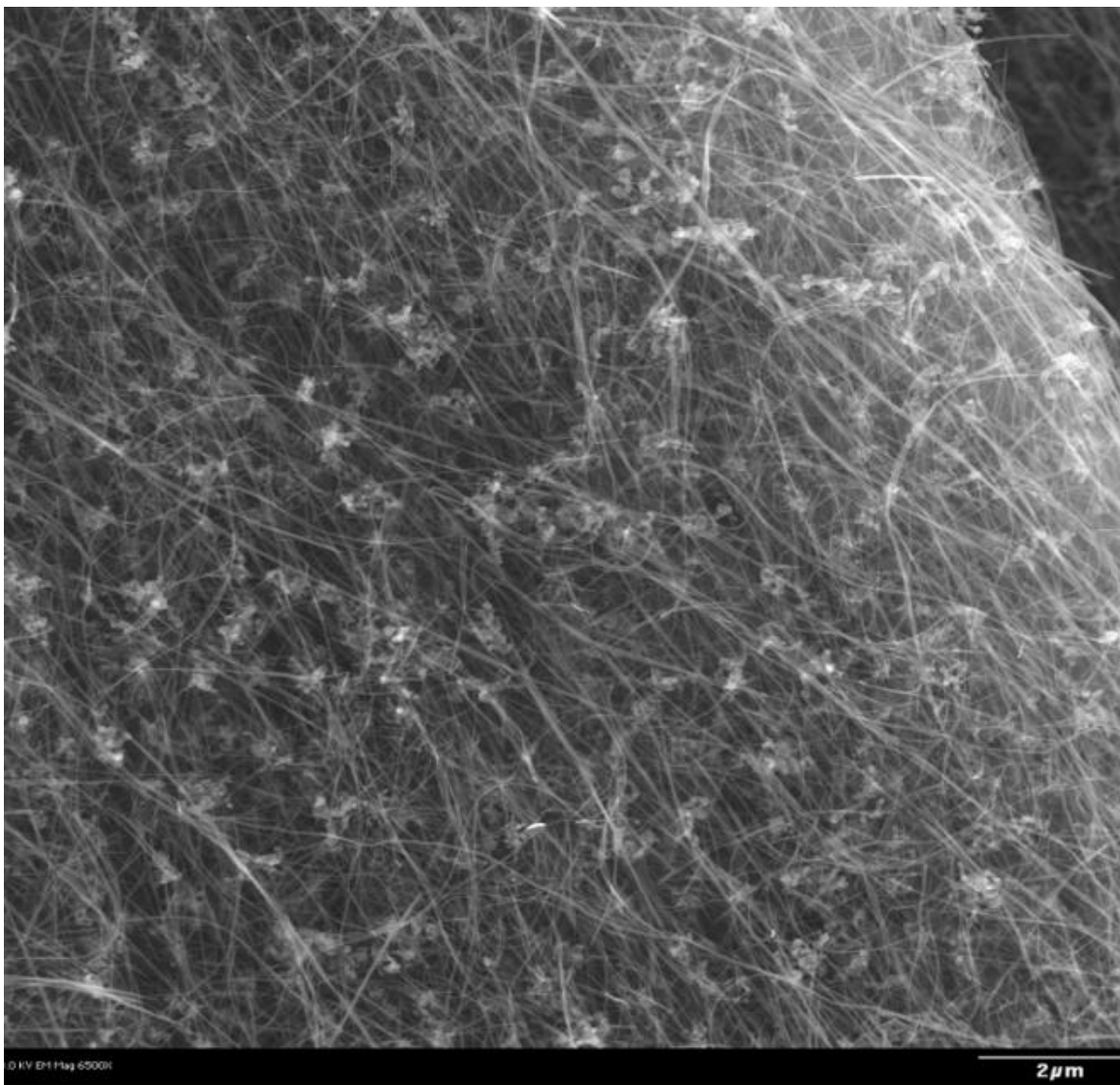


Figure 19. SEM of carbon nanotube mats made from Cambridge CVD process. High levels of iron can be easily seen in SEM image.

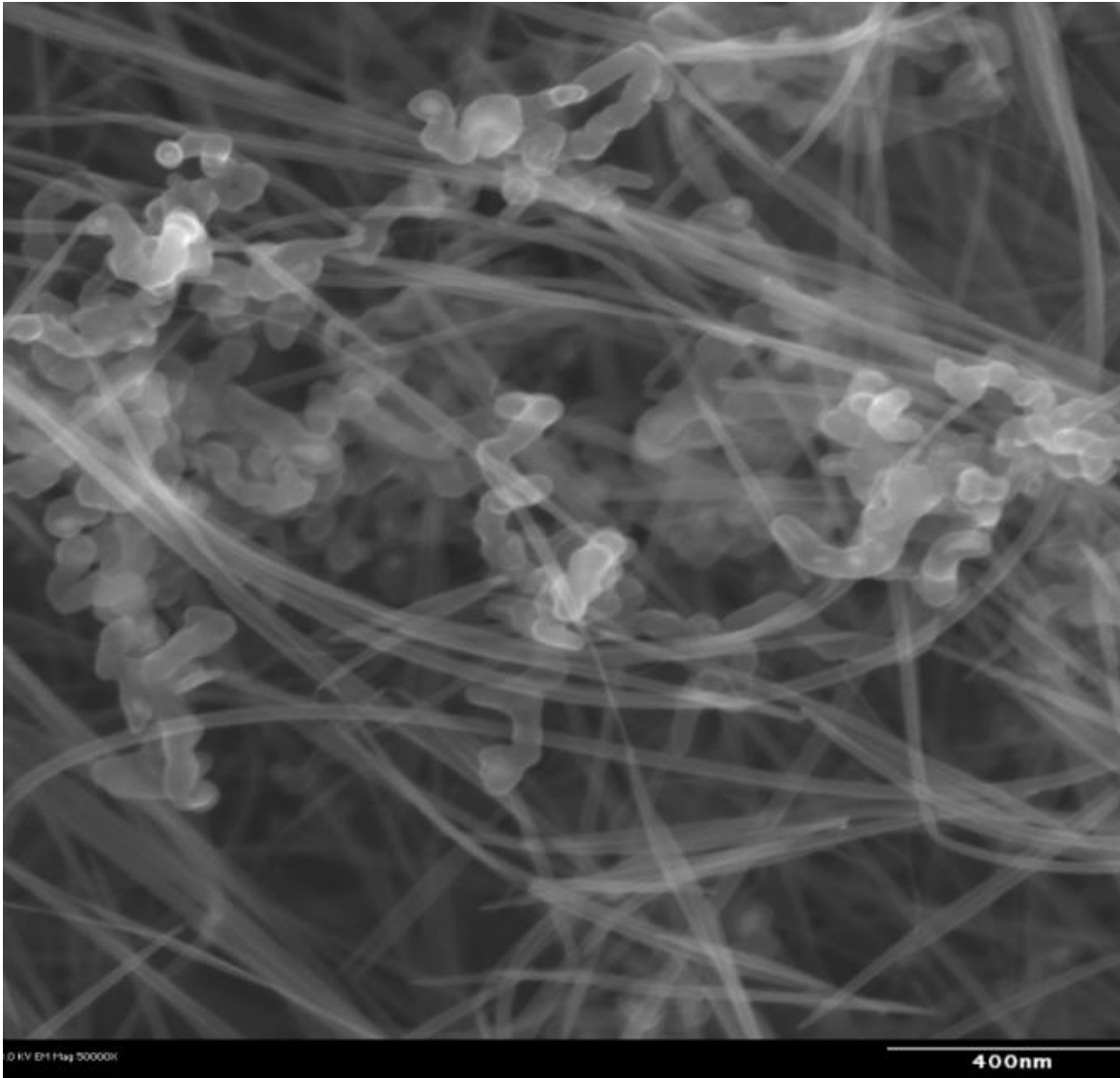


Figure 20. SEM of carbon nanotube mats made from Cambridge CVD process. High levels of iron can be easily seen in SEM image.

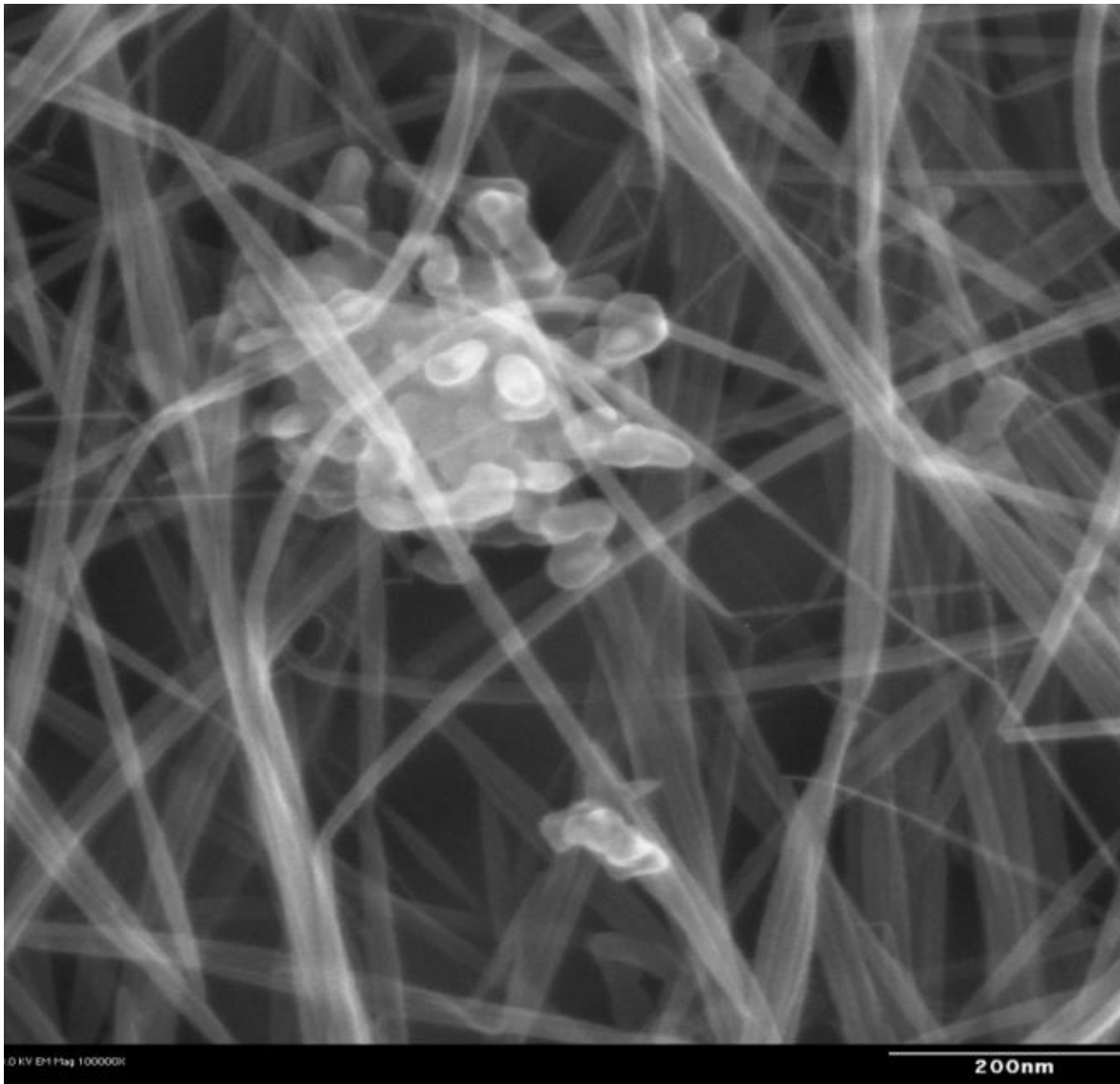


Figure 21. SEM of carbon nanotube mats made from Cambridge process. Cluster ball in the image is residual iron catalysts.

3.2 CARBON NANOTUBE POST GROWTH TREATMENTS

In traditional CNT fabrication techniques, an unwanted product in the material is the iron catalysts. In literature, there have been various techniques developed to attempt the removal of these unwanted particles. Moreover, CNT have been found to be prone to oxidation and contain amorphous carbon residual from the growth process.

A technique that is explored in order to remove amorphous carbon material, oxidation and other defects is low temperature annealing of the CNT fibers. Measurements of the resistance of the material subjected to annealing process can provide a better picture on the benefits and effects of annealing at 500°C for 30 mins at 10^{-4} Torr.

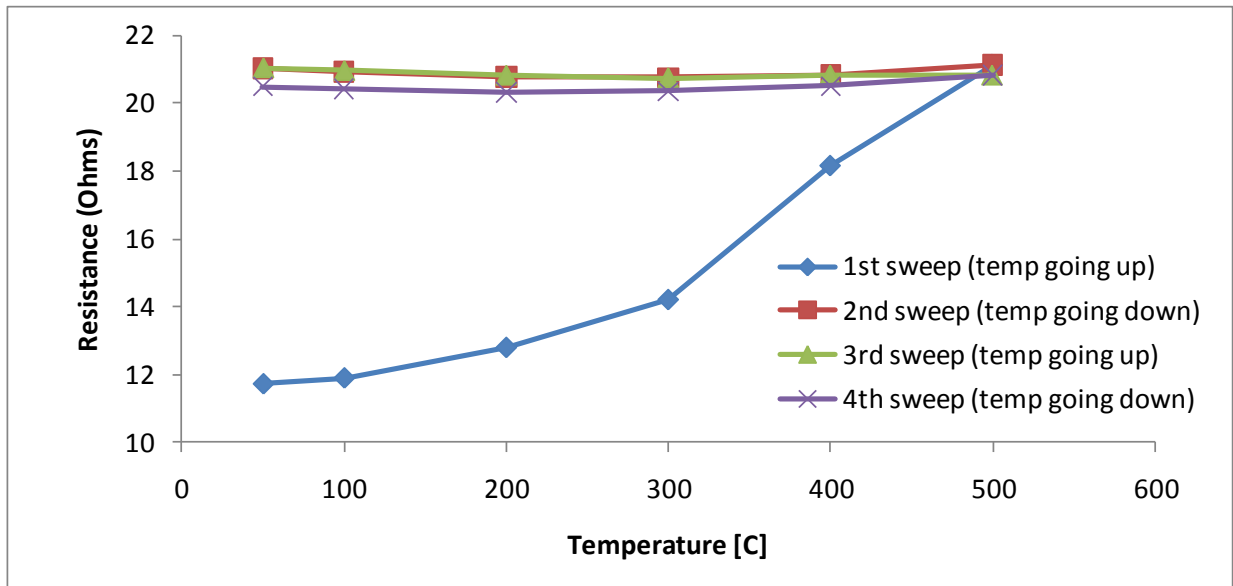


Figure 22. Resistance vs. temperature measurement of Cambridge fiber.

A Physical Properties Measurement System (PPMS) was used to conduct a four-probe measurement of the resistance during temperature variation. The four probe system schematic shown in Figure 23 uses two probes to measure current and two to measure voltage as voltage is varied. A CNT film made from condensed Cambridge fibers was used in these measurements. Temperature was ramped up to 500°C and back to the initial starting temperature and then this process was conducted again. These measurements show that after the initial annealing sweep, the irreversible changes were established in the material (Figure 24). Moreover, these measurements showed both semiconducting (lower temperature range) and metallic (higher temperature range) properties of the CNT film, respectively [22].

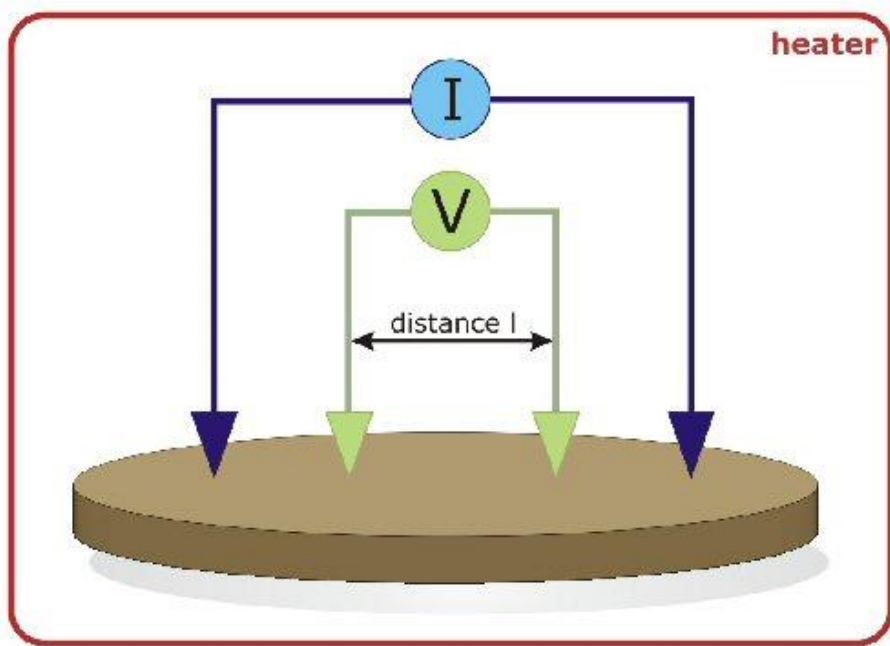


Figure 23. Schematic of a four probe setup.

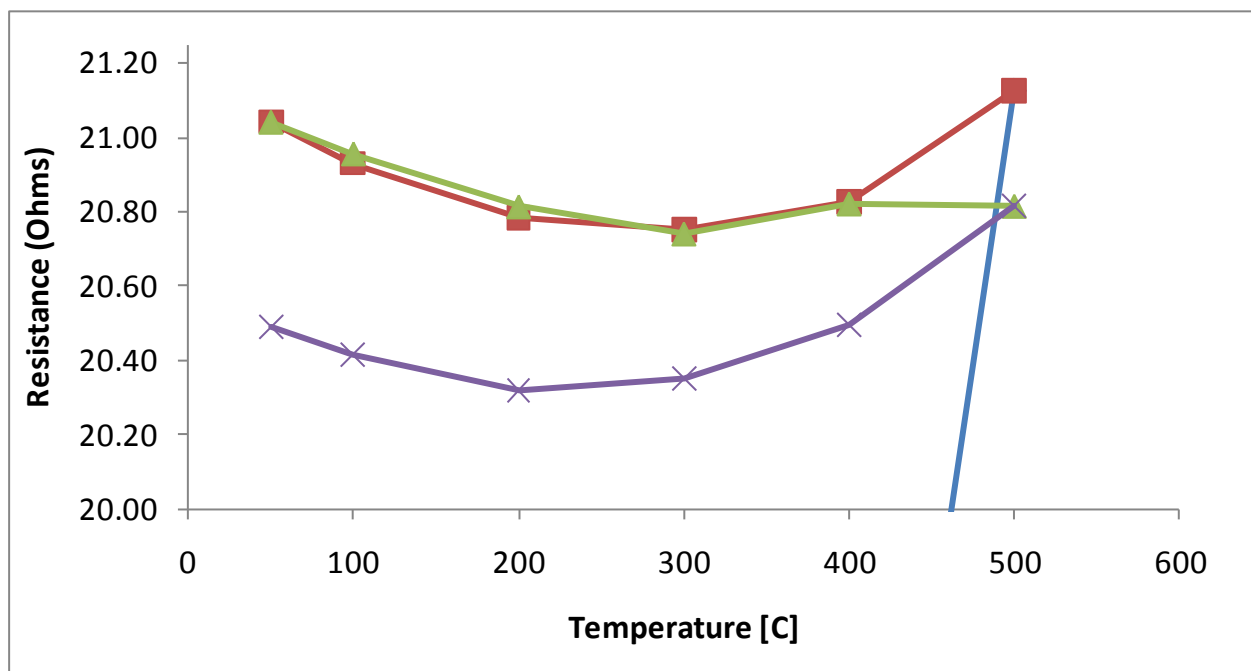


Figure 24. PPMS measurement resistance vs. temperature of Cambridge fiber.

To get a better description what is going on along the CNT tape, localized measurements were done to study the annealing effect. Optical and evanescent microwave measurements can shed some lights on the effect of annealing. Optical measurements were done using Dr. Clark's Optical Characterization setup at Wright State University. A tungsten halogen was the light source optimized for VIS-NIR (360 nm - 2500 nm) range. This signal was detected by a linear silicon CCD-array operating in 200 nm - 1100 nm range. Using setup similar to the schematic diagram in Figure 25, reflectance of the CNT tape was measured.

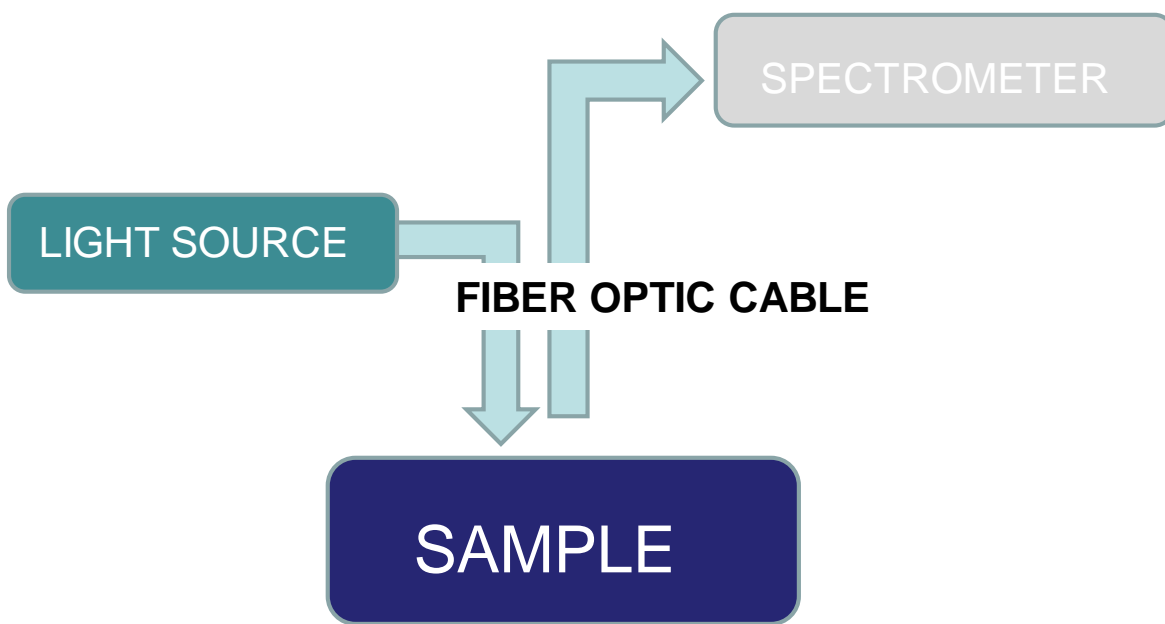
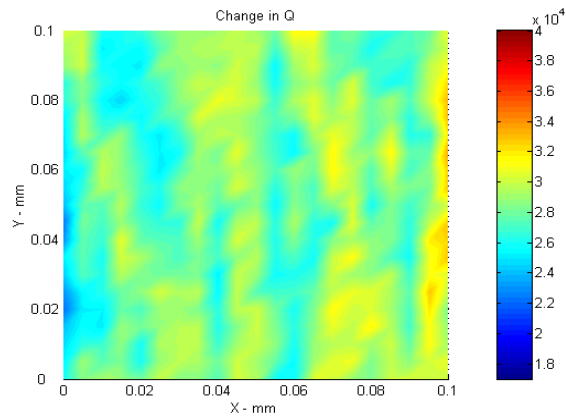
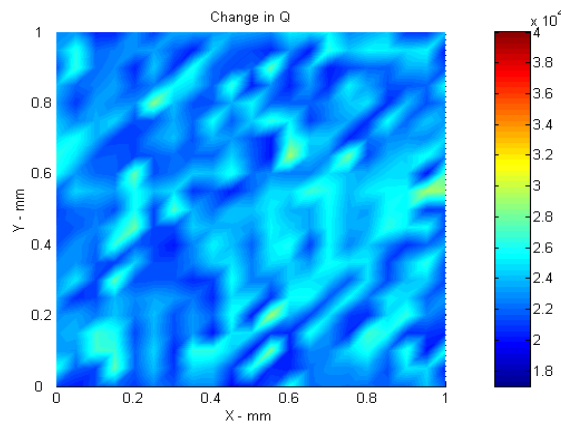


Figure 25. Optical characterization set-up.

The CNT tape 3 cm wide and 10 cm long was divided on small square areas (1 cm x 1 cm). A grid was established in the tape to identify designated areas (3 rows and 10 columns). For example, the designated area "1-3" is located in the first row and the third column (1 cm² area in size). 14 different areas of the CNT tape using both optical and evanescent microwave microscopy were studied.



A. 1-3 before annealing



B. 1-3 after annealing

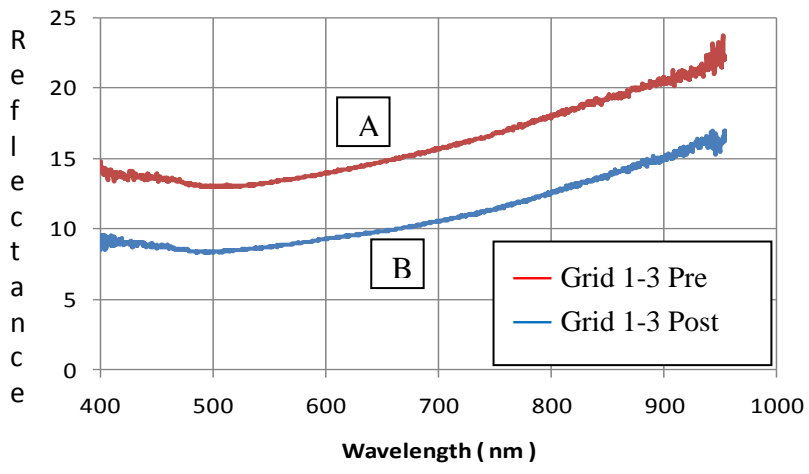
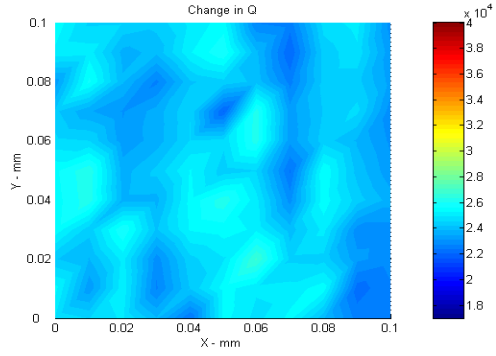
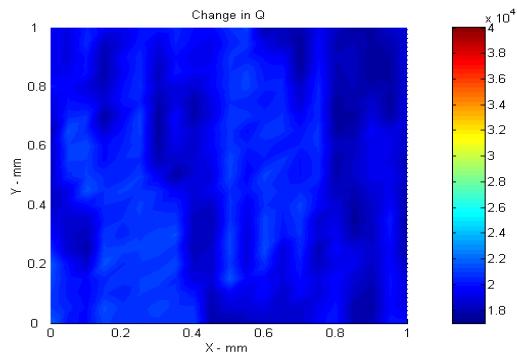


Figure 26. Evanescent microwave microscopy (A,B) and optical measurements of CNT



A. 2-3 before annealing



B. 2-3 after annealing

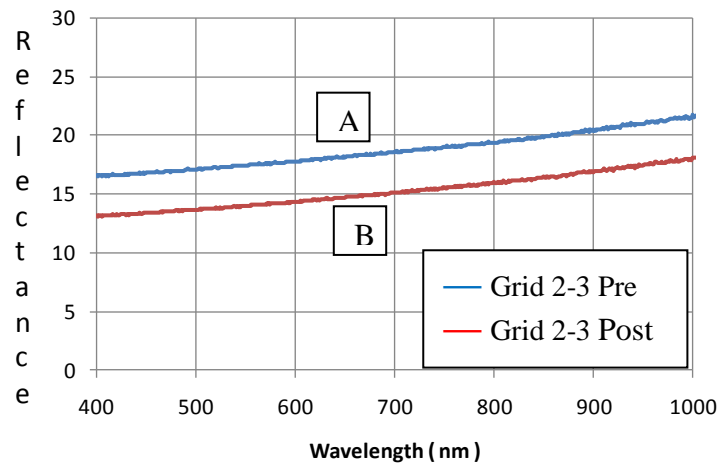
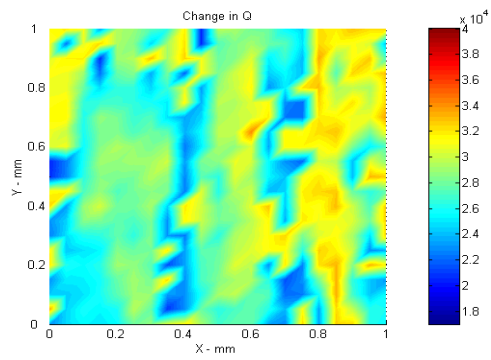
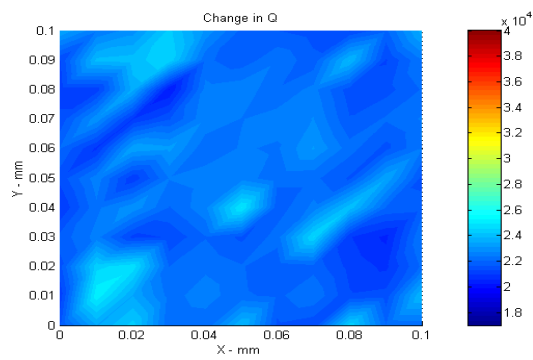


Figure 27. Evanescent microwave microscopy (A,B) and optical measurements of CNT film in designated area “2-3”.



A. 1-5 before annealing



B. 1-5 after annealing

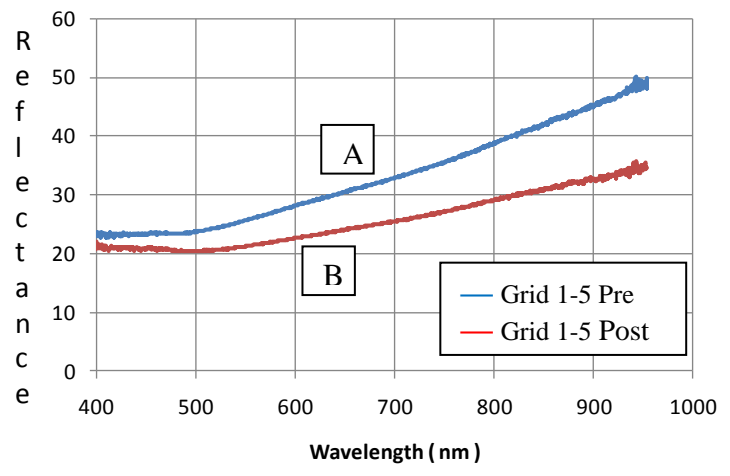


Figure 28. Evanescent microwave microscopy (A,B) and optical measurements of CNT film in designated area “1-5”.

The Q-Factor (Quality factor) of a material is directly proportional to the conductivity of the material. The evanescent microwave measurements show plots of quality factor in designated areas. Both the evanescent measurements and optical measurements are show the same conductivity change in the designated areas (Figure 27, Figure 28, Figure 26). In some areas of the carbon nanotube material conductivity is increase and in some areas conductivity is decrease. However, throughout the whole material there is a general shift towards higher resistivity due to annealing. This suggests surface conductivity decreases in CNT tape due to the annealing process.

CHAPTER 4: FABRICATION OF GRAPHENE FROM SiC

4.1 GROWTH FROM SiC

This chapter will discuss decomposition of SiC to create carbon nanomaterials. One of the main goals is to establish a standardized process where repeatable high quality material can be grown. The following sections will outline impurities encountered in the fabrication process and how those risks were mitigated using various surface modifications. Subsequently, graphene grown will be studied in using electron beam induced spectroscopy to correlate electron mobility to physical uniformities.

4.1.1 SURFACE IMPURITIES

The formation of graphene have been observed after annealing SiC wafers at high temperatures, 1200°C – 1700°C, at pressures ranging from 10^{-3} to 10^{-5} Torr. Exact growth mechanisms are debated, and there are even contradicting results in literature claiming growth of CNT from different faces (Si and C) or both faces of SiC [13].

The beginning of this study is to ensure that the commercial grade 6H and 4H silicon carbide wafers are properly treated before decomposition. Traditionally a RCA treatment was used to clean the wafers. This cleaning process is a two part process; the first step is to clean the wafer with heated deionized water, hydrogen peroxide and ammonium hydroxide in a 5:1:1 ratio. This step is followed by cleaning with a solution of deionized water, hydrogen peroxide and hydrochloric acid in a 6:1:1 ratio. Though this process is widely accepted as an industry standard, AFM studies of surface topology after RCA treatment showed irregularities in cleanliness [9].

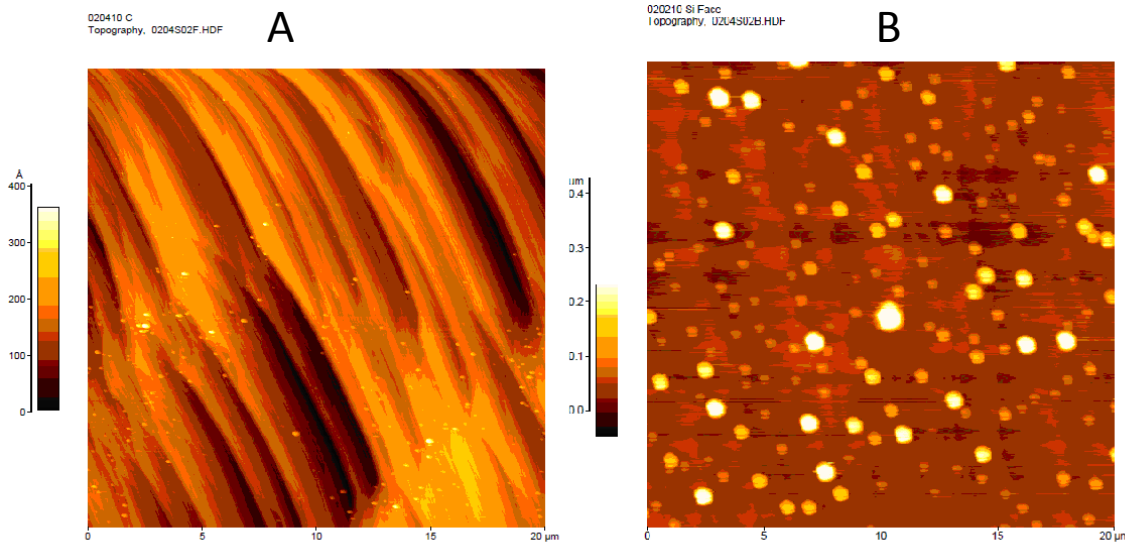


Figure 29. AFM of C-face (A) and Si-face (B) of RCA treated SiC wafers.

Figure 29 are 20 μm x 20 μm AFM micrographs of the C-face (A) and Si-face (B) of SiC film. The unknown spherical particles were not removed during the standard RCA treatment, and most likely they are oxidized particles or heavy metal impurities. These however were not the only surface defects that were seen.

Recently there have been reports of other structure defects in epi-layers of SiC grown on low off-angles (0001) SiC wafers after annealing. Nanoscale control of surface topology is imperative in decomposition of SiC, since the end products are also nanoscale. This phenomenon called Step Bunching has been shown theoretically and experimentally to depend on the temperature gradient during sublimation or growth of SiC. This process of step bunching on the surface is called the Ehrlich-Schwoebel effect (ESE) [12]. This effect explains how extremely small thermal fluctuations during SiC growth process can dominate mass flow to the lowest thermodynamically states which tend to create steps and terraces on the surface of SiC.

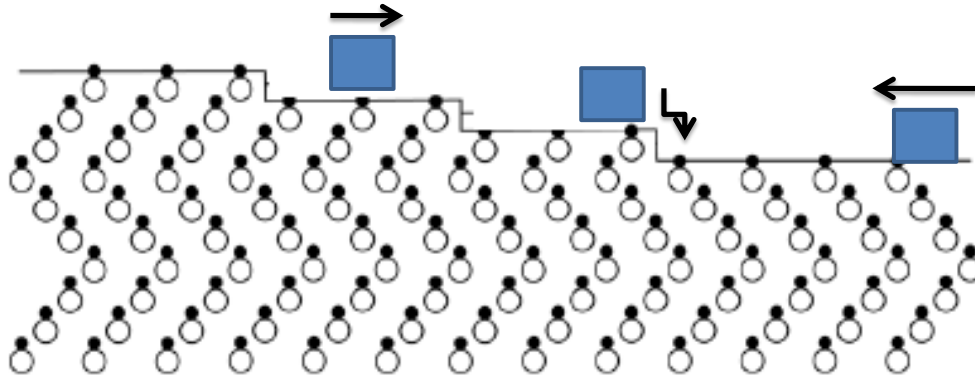


Figure 30. Mass current flow on SiC during sublimation.

Figure 30 is an illustration of mass current flow on the surface of SiC during sublimation. There is going to be a drift of mass to the lowest energy position often directed by small thermal fluctuations on the surface. These surface potential barriers cause steps to be formed, and since each step is created independently, the steps begin to meander without regularity.

There are two dimensions of concern, L which are the step heights and l the terrace lengths. For our purposes, control of the terrace lengths is more important than the step heights. These lengths are shown in Figure 31.

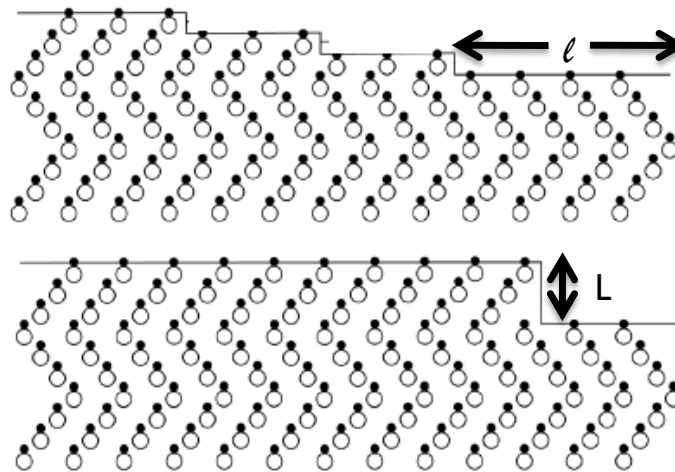


Figure 31. Illustration of terraces and step heights.

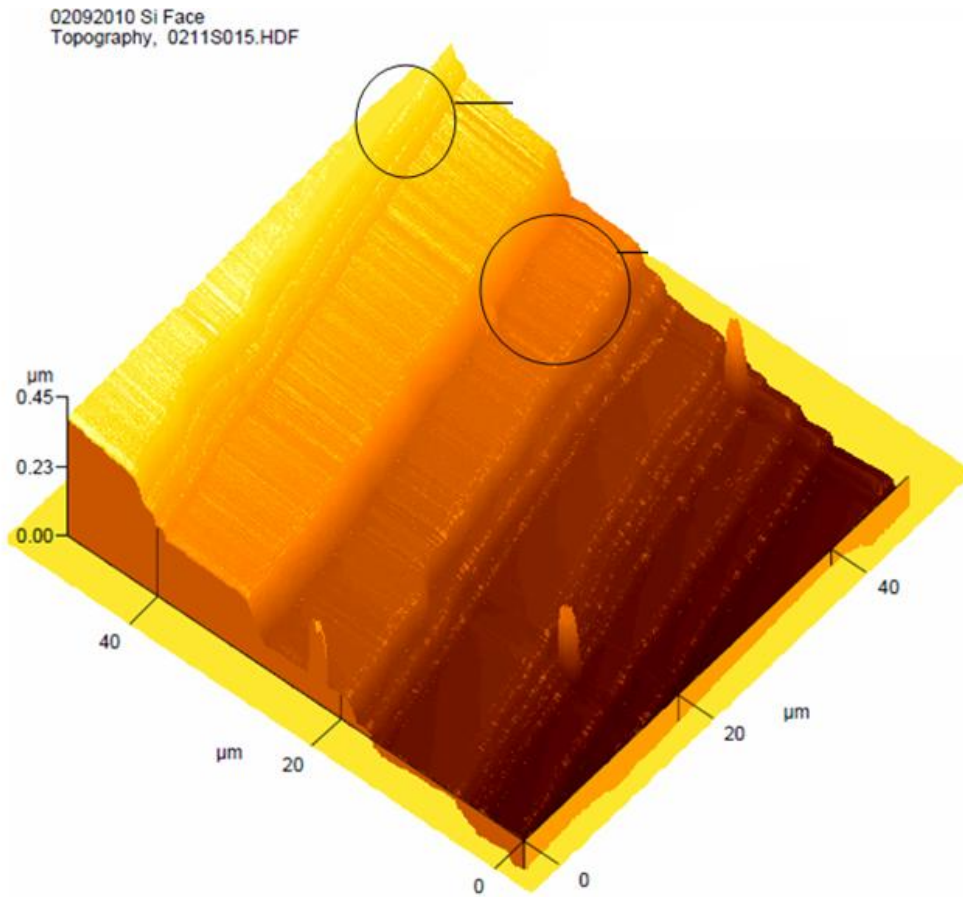


Figure 32. AFM of SiC surface depicting step-bunching.

Figure 32 is an AFM scan of Si-face of SiC substrate, showing the terrace and stepping on the surface. The goal now becomes how decrease the step length L , and increase the terrace length l .

4.2 SURFACE MORPHOLOGY CONTROL

As explained earlier, control of quality growth is dependent on the elimination of particulate accumulation on the surface and step bunching. First to remove these extra contaminates the SiC was annealed in the OxyGon Industrial Inc. furnace at 700°C under argon for 1 hour in hopes to remove any surface contaminates held on the surface after the RCA treatment by weak van der Waals forces.



Figure 33. OxyGon furnace at AFRL.

The furnace at Wright Patterson Air Force Base Air Force Research Laboratory Materials and Manufacturing Directorate is the Oxy-Gon Universal Application furnace FR Series with modified chamber. The chamber has a maximum operating temperature of 3000°C (5432°F) and will operate in vacuum, ambient pressure, wet or dry environments. The chamber has a turbomolecular pump to achieve stable high vacuum pressures, 10^{-6} Torr, as well as all internal electropolished components to ensure stable pressures during runs. There are two ports for thermocouples, a small window, as well as additional ports for gas control systems.

Initially the heating chamber had been a graphitic heating element, which became an issue of concern considering that there could be cross graphitic contamination. This problem was solved by stripping out the graphitic element and replacing it with tungsten based heating elements.



Figure 34. Tungsten heating elements.

The tungsten heating elements shown in Figure 34 are a single phase tungsten mesh elements with a split construction. The heating element is shown to demonstrate two points (1) that there are no carbon sources located in the chamber other than the SiC and (2) since it is a split construction design with two independent current connections, there could be a possibility of a small temperature gradient in the oven itself. As previously discussed, any small thermodynamical fluctuations in the furnace would play an effect when growing nanoscale materials, in this case, single layers of graphene [13].

Moreover, it is important under growth run to characterize both Si and C face of the material. In the past, SiC was simply placed planar on the stage in the chamber – effectively not allowing one side to be decomposed at the same rate. Due to this, a new stage and sample holder were designed and built to center the samples in the center of the heat zone as well as to expose both Si and C faces.

After making these modifications to the furnaces, post annealing treatment of SiC showed to remove surface particulates left even after the RCA treatment and AFM studies post annealing returned the surface within the accepted range of $\sim 1 \mu\text{m}$.

A technique that would further normalize the surface is called the Chemical Mechanical Polishing (CMP) process. This process is widely used in the semiconductor industry to smooth wafers to create uniform surfaces. Since this technique uses both physical and chemical forces, the chances of surface damage are minimized while still achieve sub-micron global planarization.

The CMP machines and their respective polishing stage such as the ones depicted below are capable of various surface finishes with resolutions up to $.28 \mu\text{m}$. The most common types of finishes are shown in Figure 35.



Figure 35. Pictures of CMP.

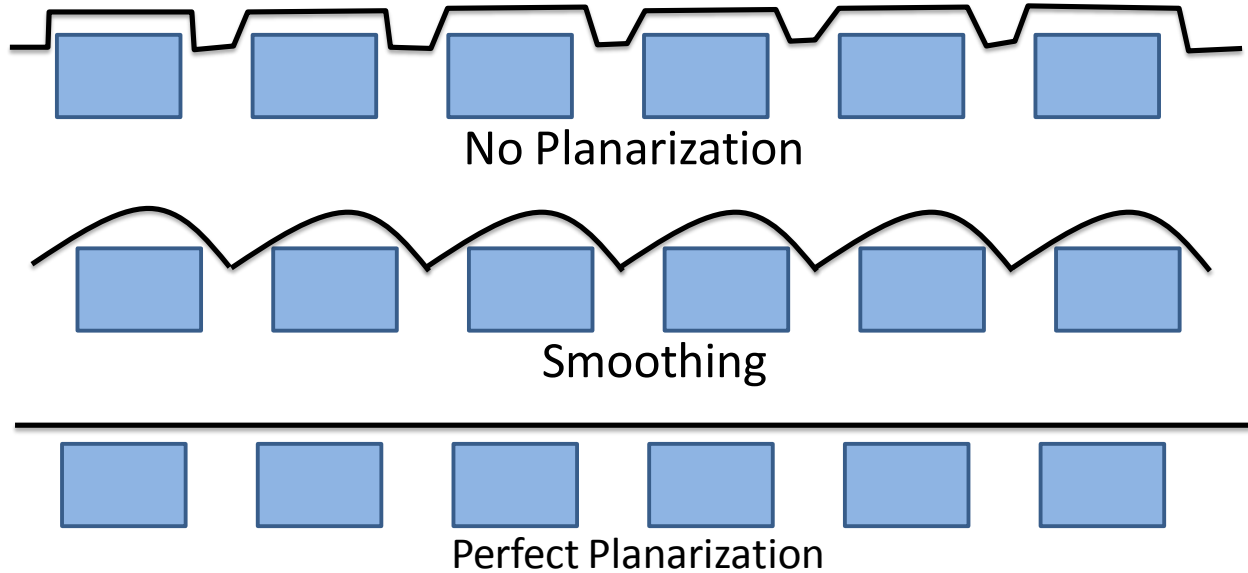


Figure 36. Possible planarization can be accomplished by CMP.

Once standardized method of preparation of SiC is accomplished, decomposition of samples in the Oxy-gon furnace under variable pressures, atmospheric content, temperatures, and ramp rates is done.

4.3 PHYSICAL CHARACTERIZATION

Structural and chemical characterization of the graphene films grown by surface decomposition was performed at Wright Patterson Air Force Base. This was achieved by transmission electron microscope (TEM), atomic force microscope (AFM) and X-ray diffraction analyses.

4.3.1 TRANSMISSION ELECTRON MICROSCOPE ANALYSIS

Transmission electron microscope is often used in studying atomic structures. The resolutions of traditional TEM systems are below .5 nm. However, this technique is considered a destructive analysis techniques since it requires the sample to be destroyed to make very thin

cross sectional wafers. The sample must be cut and polished to a thickness less than 300 μm as well as have coating of conducting metal.

The samples were formed using a Ga focused ion beam to mill out cross section from SiC wafers. The wafers are initially protected with a Pt using an in-situ e-beam deposition. These wafers are then thinned to electron transparency and then polished in an argon ion mill to remove any damaged areas. Images were taken on the FEI Titan TEM at Wright Patterson AFB. All the images were taken under 300 KeV.

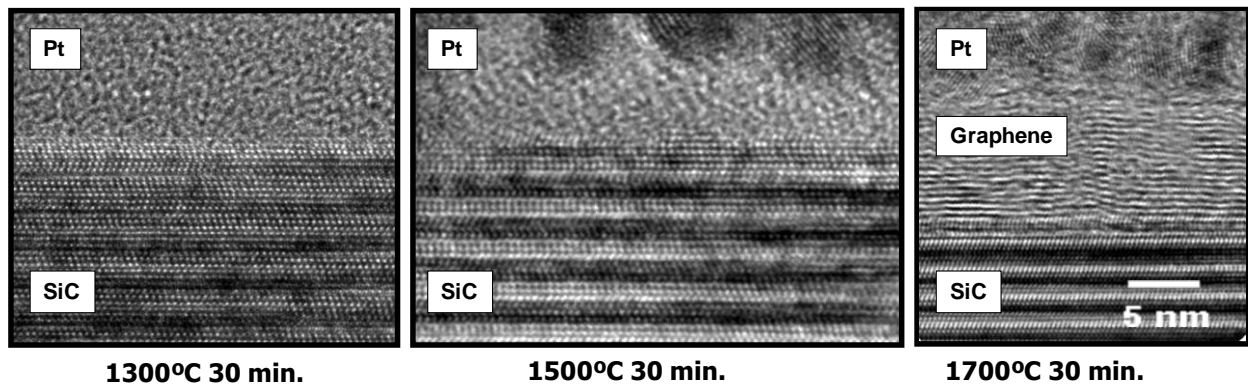


Figure 37. TEM of decomposed SiC at various annealing temperatures.

These images in Figure 37 are for samples of the Si-face of 6H-SiC annealed in argon atmospheric pressure. These samples are non-CMP, which were epi-growth and prepared by applying a layer of nitride masking. At temperatures below 1400°C, there is little change on the surface of SiC. From 1400°C to 1600°C there is noticeable region at the surface that begins to change, however, no uniform graphene layers are present. Above these temperatures, graphene layers are formed and depending on temperature and growth times, layer control can be achieved.

Epitaxial graphene growth only occurs due to epi-growth nitride masking applied. If the nitride layer is not present, carbon nanotubes begin to grow on the surfaces. The actual growth mechanism is not well known. The TEM images (Figure 38) are CNT material decomposed from non-CMP treated Si-face of 6-H SiC annealed at 1700°C under high vacuum.

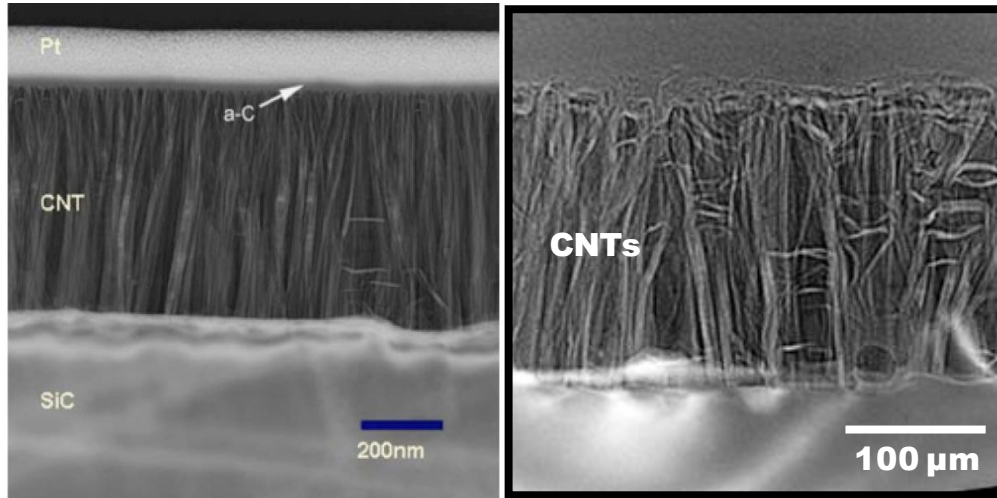


Figure 38. Cross-section of CNT decomposed from SiC wafer [13].

4.3.2 ATOMIC FORCE MICROSCOPY

Atomic Force Microscopy (AFM) is a nondestructive technique that can provide accurate surface measurements well into the nanometer regime. AFM measures the interaction between the sample and the tip of the AFM probe. By measuring small fluctuations in the position of the probe as it is dragged across the surface, AFM can generate surface topologies.

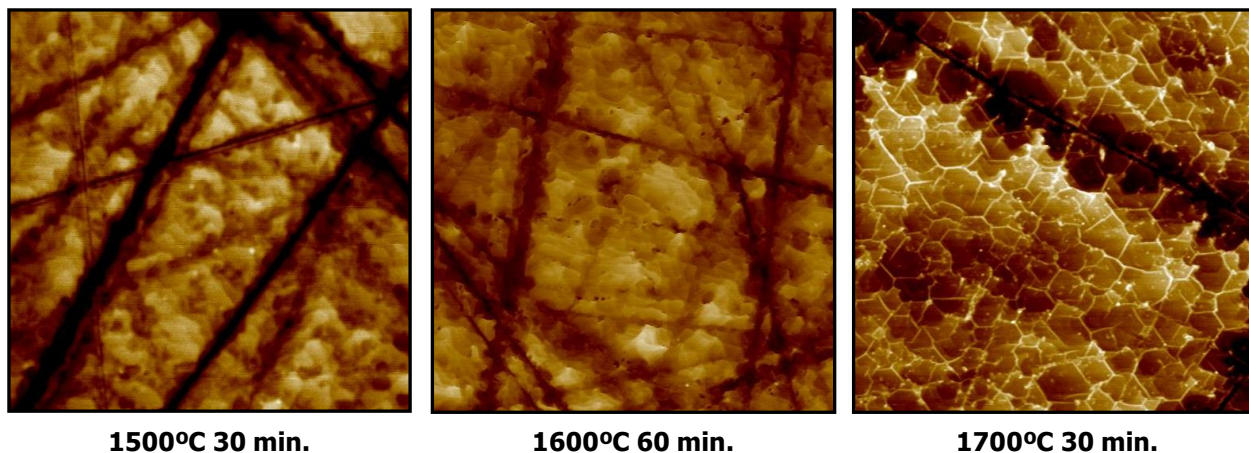


Figure 39. AFM of graphene on SiC without CMP treatment at various annealing temperatures (2 μm x 2 μm).

Figure 39 represents Si-Face of 6H-SiC that has been decomposed without undergoing CMP treatment under atmospheric argon. SiC wafers were annealed in the Oxy-Gon furnace at 1500°C, 1600°C and 1700°C for 30 minutes. The ramp rate of the temperature was about 20°C/minute.

As seen in the AFM, surface morphology is irregular, with deep scratches visible in all the images. At 1500°C, some irregular shaped flake like structures appear, at 1600°C graphene flakes are observed over the whole surfaces and finally at 1700°C highly organized atomically flat domains are observed.

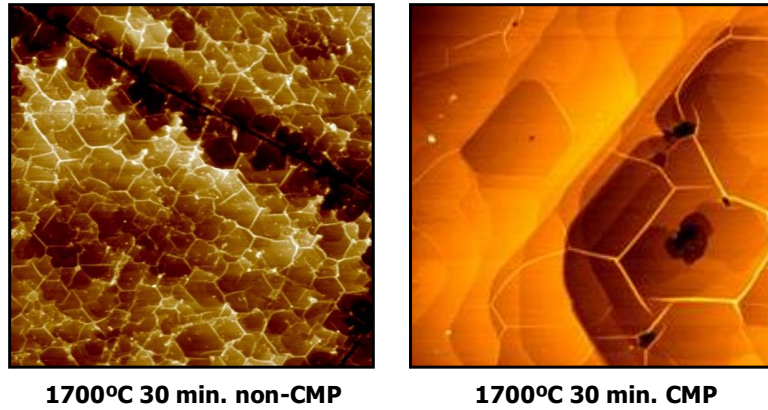


Figure 40. Comparison between non-CMP and CMP treated wafer (2 μm x 2 μm).

Under the same growth conditions, wafers that are CMP treated show drastic improvement in graphene quality. In Figure 40, films grown at 1700°C for 30 minutes for CMP and non-CMP wafer are compared. Step heights measured by Raman spectroscopy showed similar graphene thickness. Conclusions from comparing these samples are the CMP treated wafers result in larger domain sizes, less wrinkles, and smoother surfaces. Graphene layer thickness can be achieved by control of annealing times. In Figure 41, samples that were allowed to be annealed longer showed increasing thickness of graphene grown.

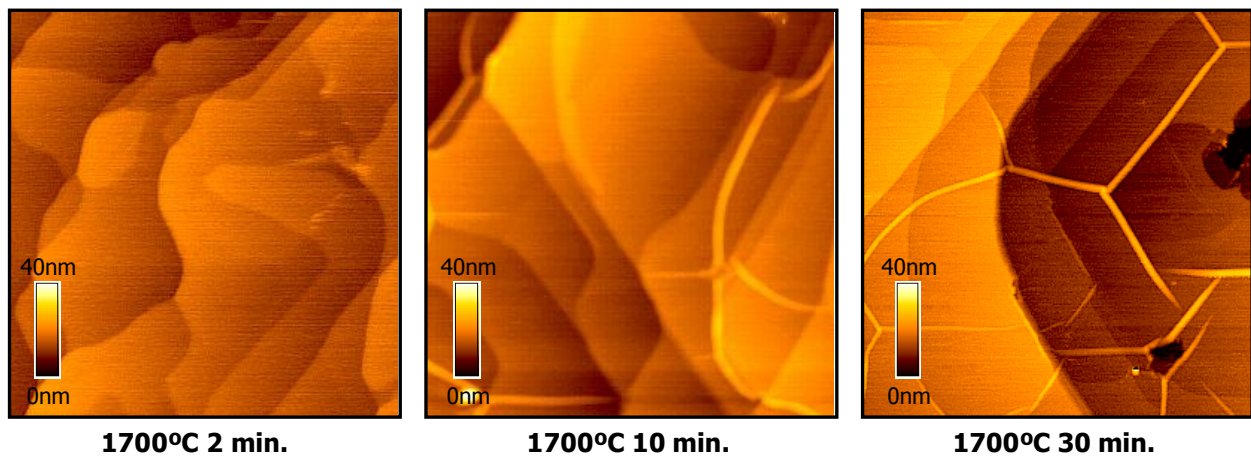


Figure 41. AFM showing increase of graphene thickness as a function of dwell time.

4.3.3 X-RAY DIFFRACTION

X-ray diffraction is a useful technique when studying crystalline films. X-ray diffraction exploits Bragg's law to generate diffraction patterns as a function of incident angle, distance between crystal planes and wavelength of incident X-ray. Bragg's Law relates the interatomic spacing between two crystalline lattices to incident wavelength and angle of incidence. A Rigaku XRD system located at Wright Patterson AFB was used to collect data.

This technique is useful in characterization of film quality from SiC decomposition. Intensity peaks at various 2θ degrees can be correlated to either SiC or crystalline C. XRD measurements was taken on nanotubes grown on the Si-face at 1700°C for 30, 60, and 120 minutes. Over the XRD measurements, several peaks begin to emerge that have been identified as pure crystalline carbon (CNT).

In the XRD for 30 minute annealing, two main peaks are present that correspond to SiC. As time of annealing are increased carbon signals being to appear in the XRD. For example, at 120 minute annealing times, both carbon and SiC signals are present, confirming that only a small fraction of the silicon carbide substrate is converted into CNT materials.

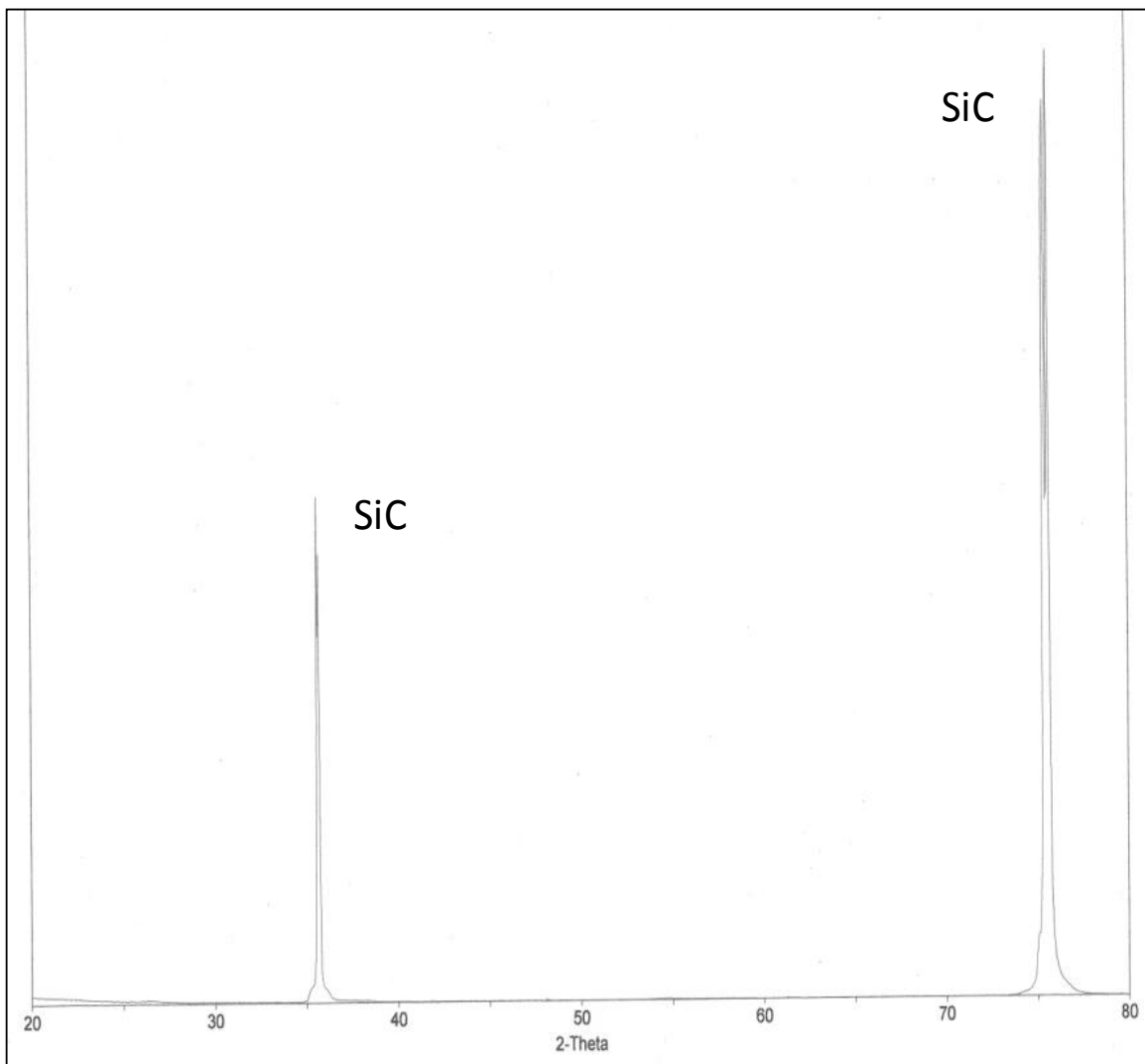


Figure 42. SiC Si-face after annealing at 1700°C for 30 minutes.

The XRD only shows peaks around 35° and 75° of 2θ scan that correlate with SiC peaks (Figure 42).

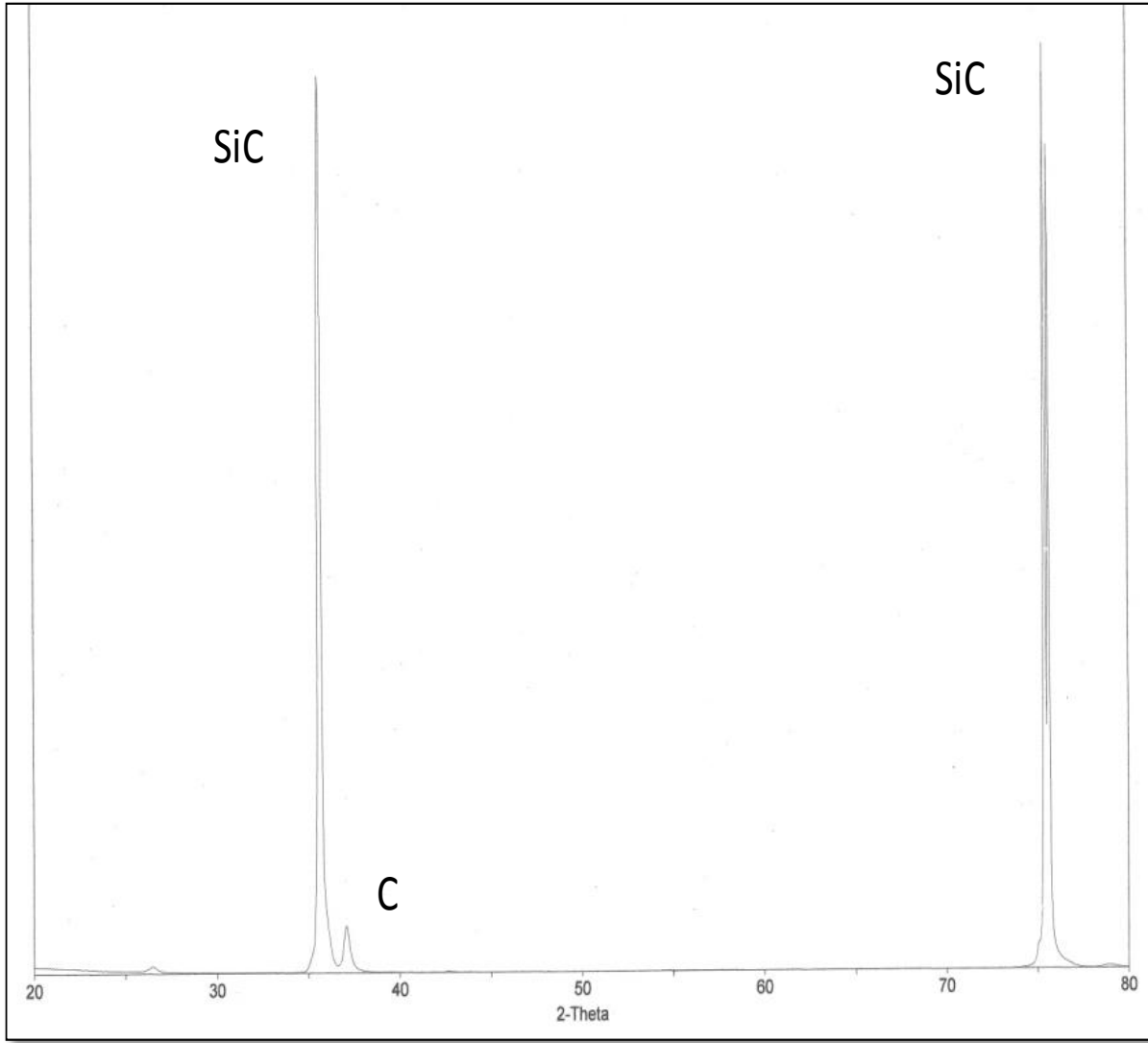


Figure 43. SiC Si-face after annealing at 1700°C for 60 minutes.

The XRD (Figure 43) shows peaks that correlate with SiC as well as crystalline carbon (CNTs).

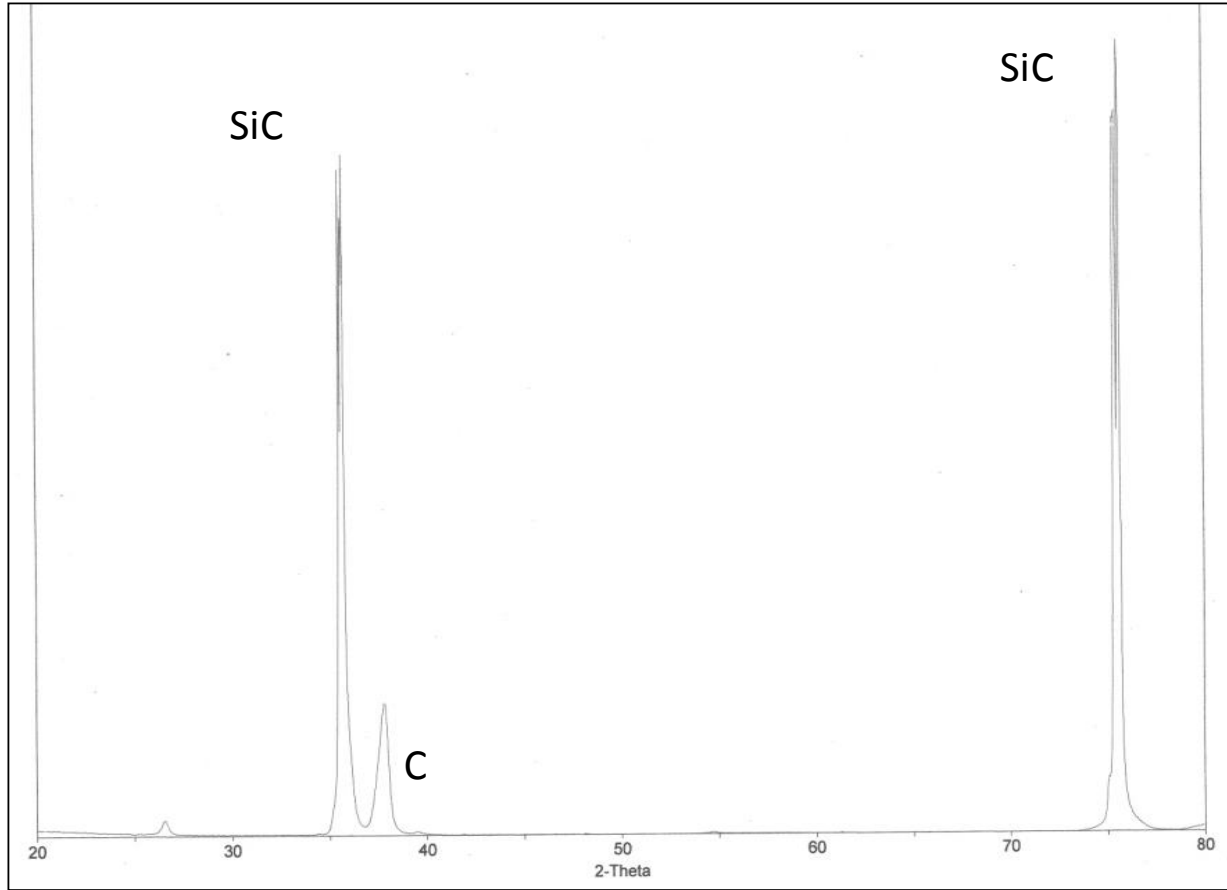


Figure 44. Si-face after annealing at 1700°C for 120 minutes.

The XRD (Figure 44) shows peaks that correlate with SiC as well as crystalline carbon. Intensity counts of carbon peaks begin to become more pronounced when compared to 60 minute annealing. Even with two hours of annealing full decomposition of SiC is still incomplete.

4.3.4 EVANESCENT MICROWAVE MICROSCOPY

Evanescent microwave microscopy spectroscopy is a non destructive technique that can be used to extract important material properties. Since both CNT and graphene can be decomposed from SiC substrates, SiC decomposition can be used to characterize local areas of patterned substrates and compare material properties of both CNT and graphene simultaneously.

Figure 45 represents measurements of SiC where graphene is grown surrounded by a forest of CNTs. Graphene has conductivity values higher than carbon nanotubes and it is easy to relate the measured Q-factor to the difference in their properties. The higher quality factor of the material results in its higher conductivity. The region boxed in red is a strip of graphene. The box in green is carbon nanotube region. The Q-factor is significantly higher in the graphene region, which corresponds to the higher conductivity values. Figure 45B shows a close up of the region between graphene and CNTs. The Q-values show presence of an intermediate material that is neither graphene nor nanotubes. Further studies must be done to unveil an exact property and morphology of the intermediate layer.

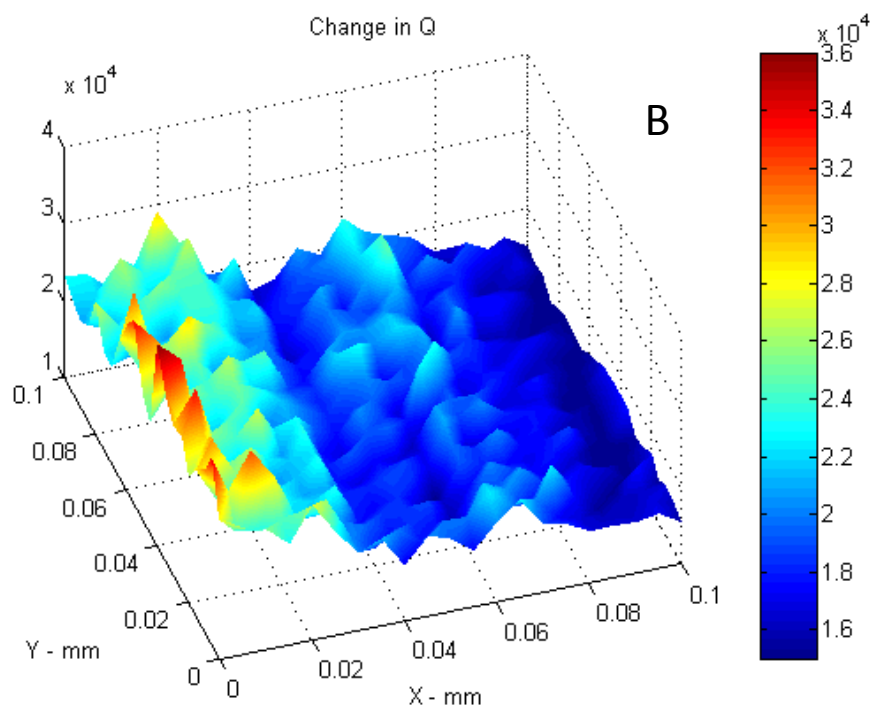
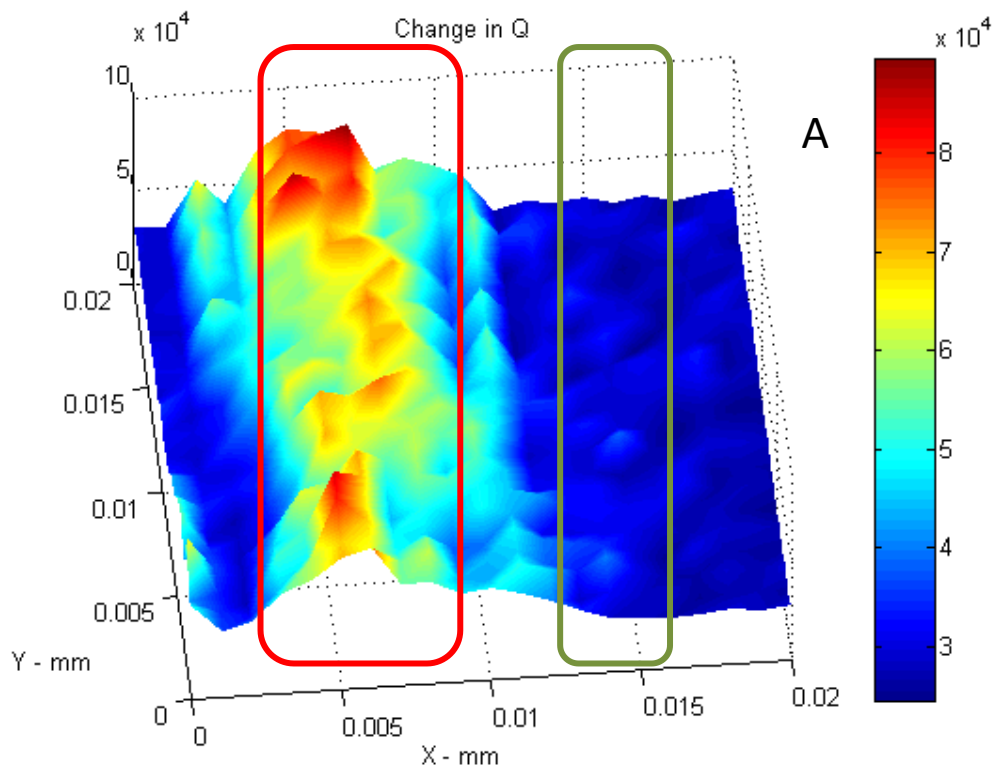


Figure 45. Q-factor plots of graphene - CNT boundary.

4.4 ELECTRON BEAM INDUCED CURRENT SPECTROSCOPY

A key feature of Evanescent Microwave Microscopy is its ability of non-destructive analysis of materials on a micron scale. In the semiconductor industry as the size of electronics become smaller, there has been a growing need for non-destructive failure analysis of devices. To isolate areas in a device of electron failure, there is a need for sub-micron resolution. One technique that has been developed is Electron Beam Induced Current Spectroscopy.

This technique utilizes a Scanning Electron Microscope electron beam to induce a current signal within a sample, which is then logged by various current monitors. Theoretically, the electrons will inelastically collide with the sample lifting the valence electrons into the conduction band and creating electron-hole pairs. In most n-p devices, this effect would cause the electrons and holes to drift in opposite directions generating currents that are much greater than the initial electron beam current. This substantial charge multiplication effect is the basis for the EBIC technique.

The current multiplication is monitored by an extremely low noise current amplifier and this information is used to create a signal image. The image qualitatively shows the electronic properties within the sample within the resolution of the SEM electron beam spot size.

This technique is extremely useful in locating junction defects, recombination sites and potential sample degradation areas. For example, in a typical p-n junction, majority carriers would be induced by the electron beam to drift across the space charge region and picked up by the amplifier. If however there are structural defects in the device within the diffusion length of the junction, the electron-hole recombination rates will be quenched and a change in current would be produced. This alternative current is then picked up by the amplifier and would be shown in the image as a contrast. Ideally, this induced current is measured in the form of

$$I_{EBIC} = I_0 e^{-|x|/L} \quad (49)$$

where x is the distance from the junction, I_0 is a constant and L is the minority-carrier diffusion length. Therefore, the contrast within a certain image can be related to the distance from the nearest junction as well as minority and majority carrier diffusion lengths.

Figure 46 represents a schematic of an EBIC measurement system. There is a traditional SEM component which is combined with an external I-V converter system.

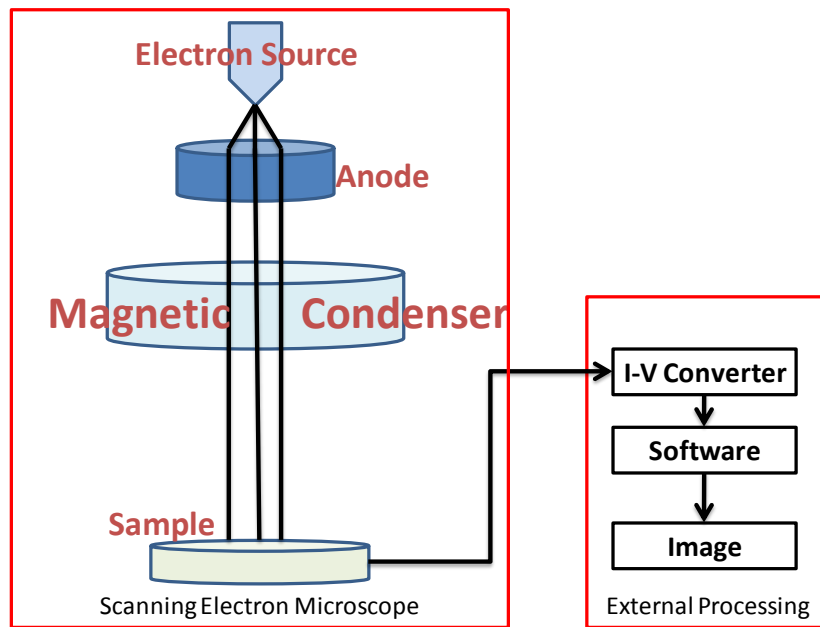


Figure 46. Schematic of EBIC system.

A Scanning Electron Microscope at AFRL (WPAFB) was modified to perform Electron Beam Induced Current (EBIC) studies. SiC was decomposed at 1700°C for 120 minutes to form a graphene multilayer. The graphene was marked off and four probes were connected in as in Figure 47.

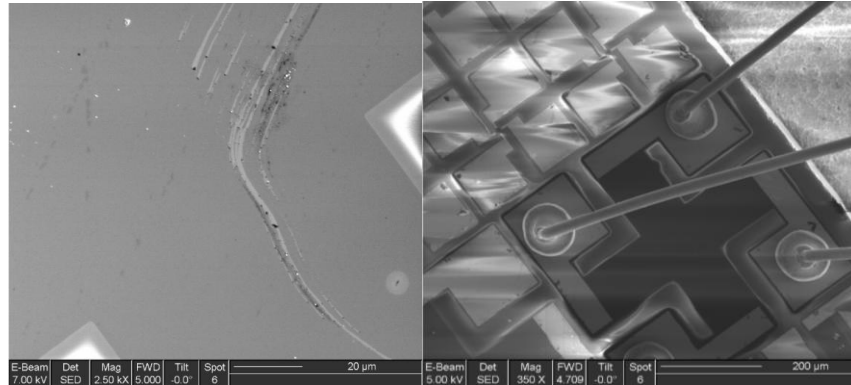


Figure 47. Traditional SEM of graphene in four-probe set-up.

In the traditional SEM image, only structural features of a material can be studied. Figure 47 is the SEM micrograph of a device made with four-probe connections. Structural defects such as scratches on the surface seen in Figure 47 as well as particle debris can be studied by using SEM. However, SEM images cannot describe any junction defects, recombination sites and potential sample electric degradation areas. EBIC images show such junction defects and potential sites of device breakdown. In Figure 48, Figure 49, and Figure 50, the top image corresponds to EBIC images and the bottom image corresponds to SEM images of the same location.

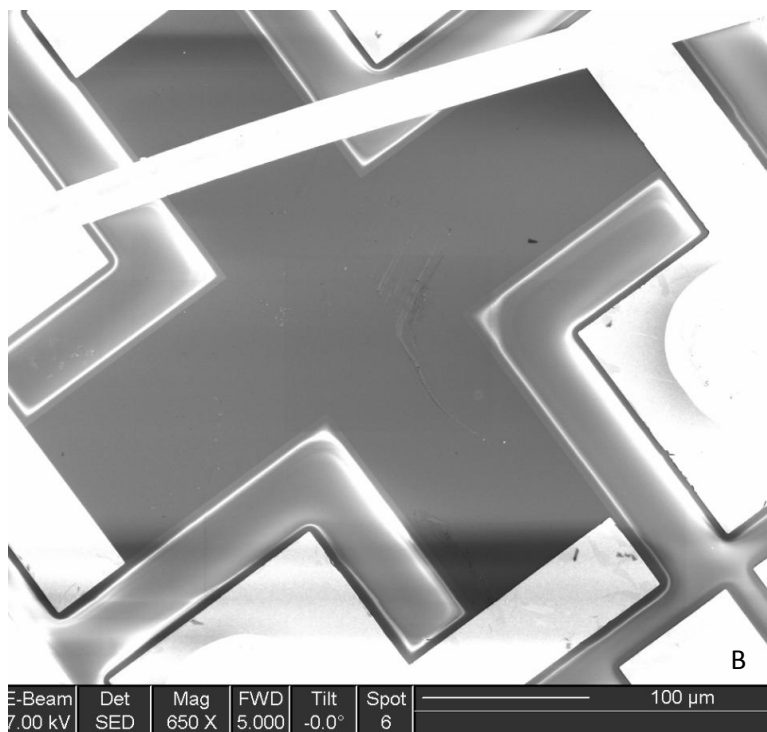
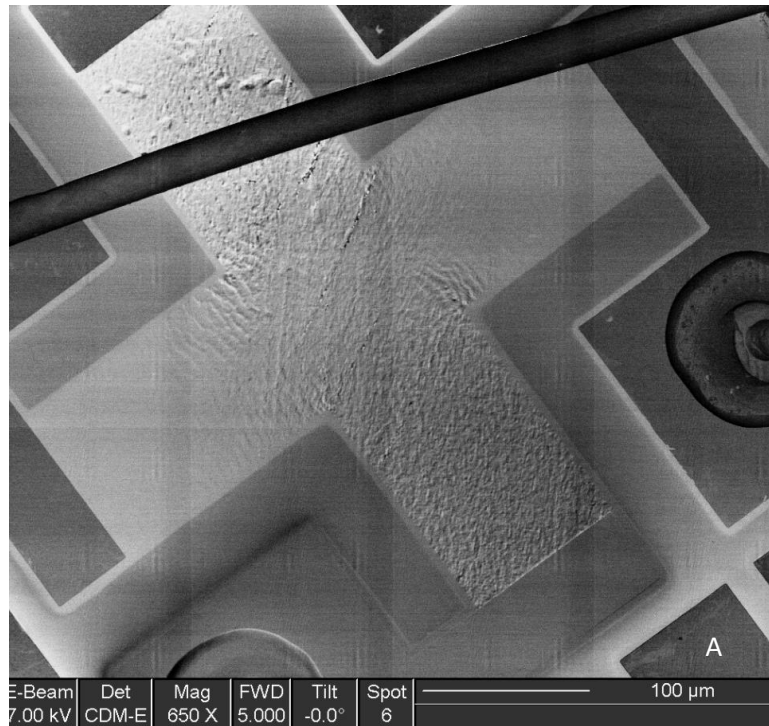


Figure 48. EBIC (A) and SEM (B) image of the same area.

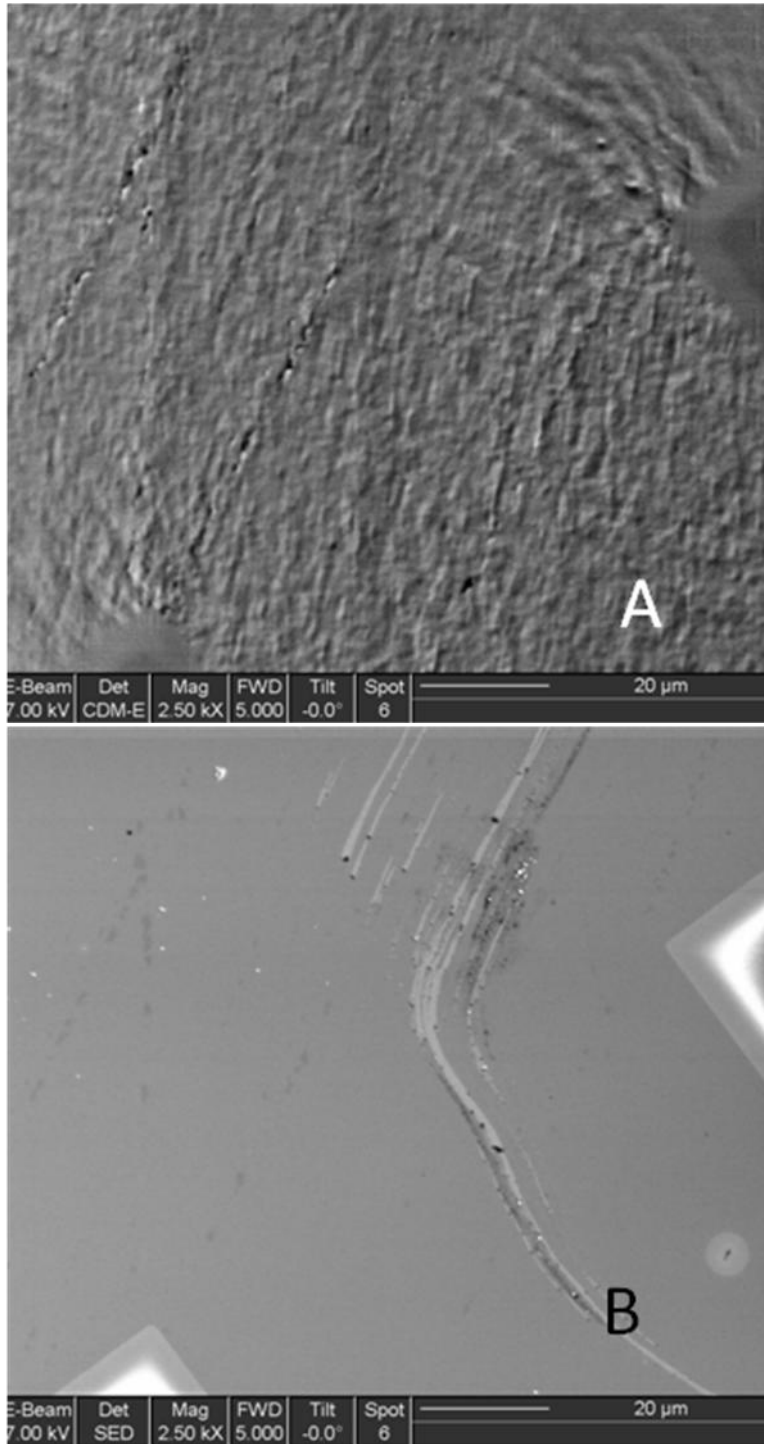


Figure 49. EBIC (A) and SEM (B) image of the same area.

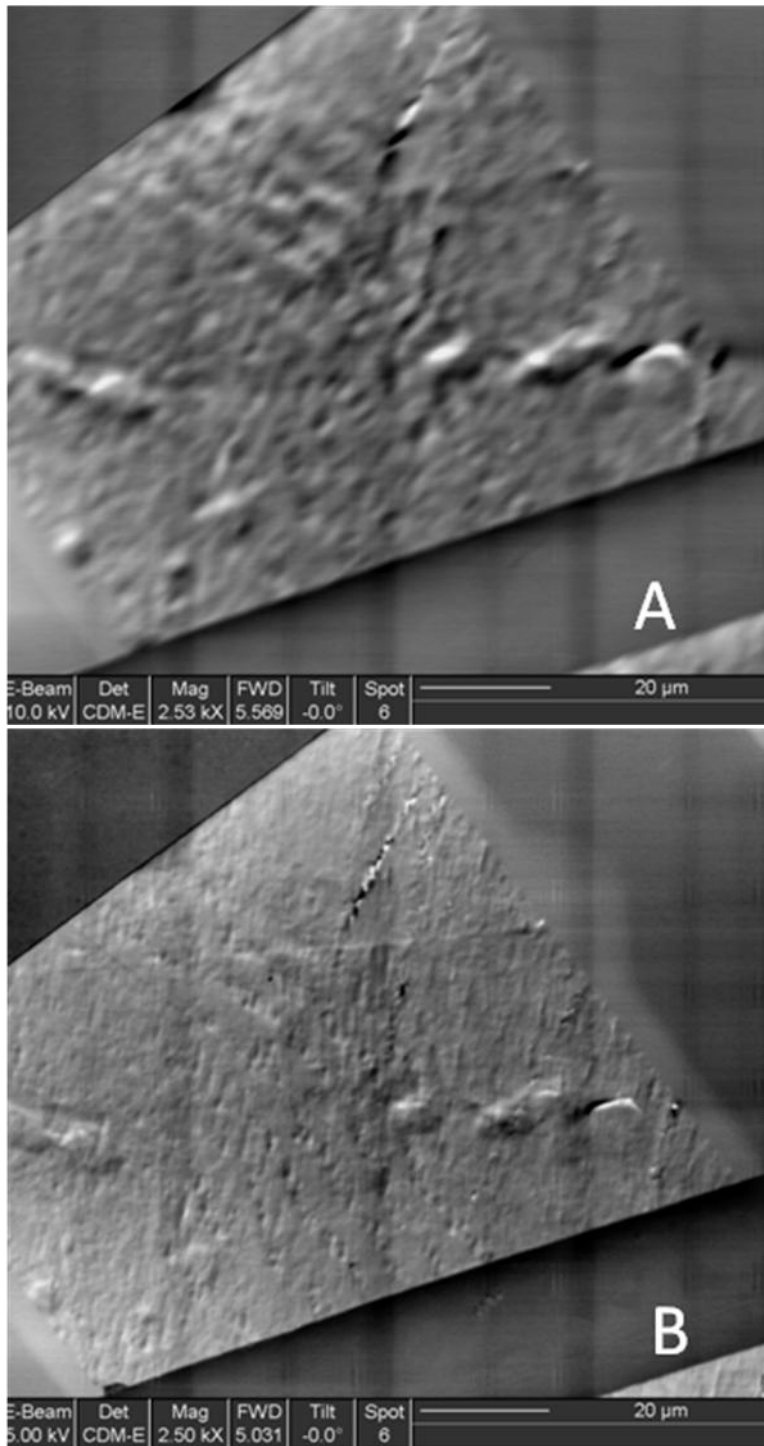


Figure 50. EBIC (A) and SEM (B) image of the same area.

CHAPTER 5: FIELD EMISSION

Using the optimized fabrication process outlined in the previous chapters, carbon nanotube material was fabricated and tested in field emission experiments. This Chapter will discuss the general physics behind field emission from metals. It will also discuss field enhancement factors and various techniques for locally generating high electrostatic fields under voltages. These principles will be used to optimize cathodes constructed from carbon nanotube fibers.

5.1 THEORY OF FIELD EMISSION

In atomic physics, ionization energy is well defined – it corresponds to the work needed to overcome atom's Coulomb force and remove an electron to infinity. Inevitably, after ionization the atom is rearranged due to the loss of an electron and the atom takes on a new configuration.

In the case of solids the work function W is the amount of energy it would take to remove an electron to infinity. Often the work function is defined in terms of a potential, $\phi = W/e$. A more useful definition of the work function potential is the energy needed to remove an electron from a solid to a relative distance away from the surface.

In removing an electron from a solid there are some key interactions that contribute to the work function potential. First there is penetration of the electron wave functions into the vacuum. The tails of the wave function that describe the occupied levels will penetrate some distance outside the solid. This results in an electric dipole layer at the surface of the metal. In order for an electron to escape it must overcome this surface barrier potential.

Having crossed the surface barrier potential, the electron must still overcome the image force. The interaction with the image forces is simply given by the formula

$$U(x) = \frac{-e^2}{16\epsilon_0\pi x} \quad (50)$$

where x is the distance to conducting plane defining a location on the surface. Equation (50) is calculated by computing the work needed to move an electron from x to infinity.

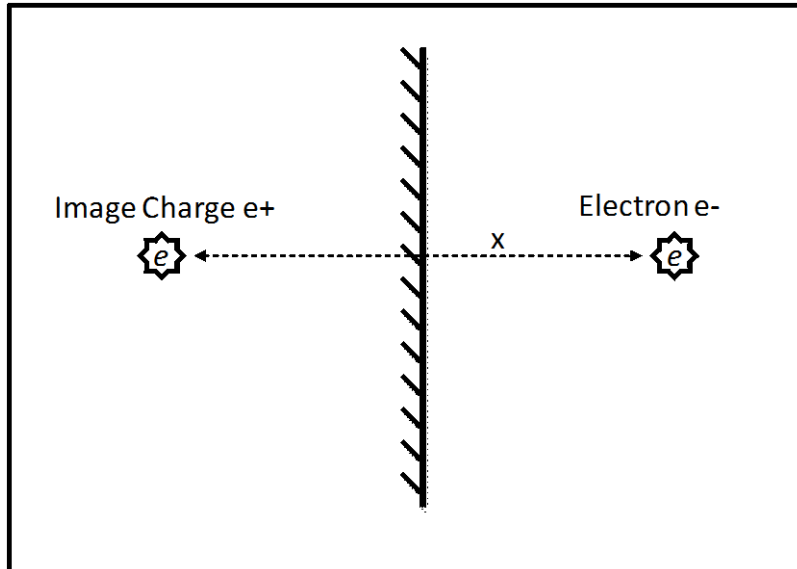


Figure 51. Electron in front of conducting plane e^- is mirrored by the image charge e^+ . Distance between two image charges from the conducting surface is the same.

This method of electron escaping from the solid is very different from ionization. As the electron is pulled away from the solid the positive charge continues to move deeper into the solid. This is equivalent of saying, when an electron is removed another is taken from within the solid to replace the one lost. In general, ionization energies are often greater than the work function. Work function and ionization energy for metals is given in Table III.

Table III. Comparison of work function and ionizations for various metals and metal surfaces [9].

<u>Material</u>	<u>Face</u>	<u>W (eV)</u>	<u>IE (eV)</u>
Li	Polycrystal	2.90	5.39
Na	Polycrystal	2.75	5.14
K	Polycrystal	2.30	4.34
Rb	Polycrystal	2.16	4.18
Cs	Polycrystal	2.14	3.89
Al	(100)	4.41	5.99
	(110)	4.06	5.99
	(111)	4.24	5.99
Ag	(100)	4.64	7.58
	(110)	4.52	7.58
	(111)	4.74	7.58
Cu	(100)	4.59	7.48
	(110)	4.48	7.48
	(111)	4.98	7.48
Au	(100)	5.47	9.23
	(110)	5.37	9.23
	(111)	5.31	9.23
W	(100)	4.63	7.98
	(110)	5.25	7.98
	(111)	4.47	7.98
Ni	(100)	5.22	7.64
	(110)	5.04	7.64
	(111)	5.35	7.64
Mo	(100)	4.53	7.10
	(110)	4.95	7.10
	(111)	4.55	7.10

Currently there are three ways of measuring the work function. One is to heat the material and boil an electron off to stimulate *thermionic emission*. Second is to photons of a specific energy to stimulate *photoemission*. The last way is to apply a strong enough electric field to the metal to lower the potential energy in vacuum below the Fermi energy and have the electron tunnel through the barrier. This process is called *field emission*.

5.2 PRINCIPLES OF THERMIONIC EMISSION

At a finite temperature, a distribution of electrons can be described by Fermi-Dirac distribution

$$f(E_k, T) = \frac{1}{e^{-\beta(E_k - \mu)} + 1} \quad (51)$$

The emitted electrons can be characterized by energy relative to the vacuum level so the zero of E_k is taken to be at vacuum level. The distribution is also dependant on the temperature, where $\beta = 1/k_B T$. The μ as used above is the chemical potential of the surface of the solid equal to $-W$

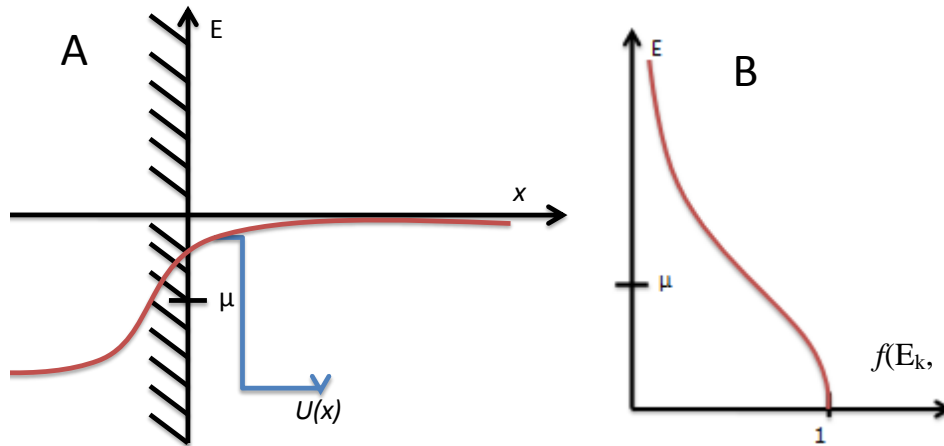


Figure 52. (A) Potential $U(x)$ as a function of position from the surface and (B) Fermi-Dirac distribution as a function of energy.

There will be a certain temperature where there is a finite probability of occupation of energy states that will allow electrons to leave the surface. These electrons contribute to the thermionic emission current. The current density normal to the surface can be given by

$$J(T) = -e \sum_{\mathbf{k}} \sum_s v f(E_k, T) |R|^2 \Theta(v) \quad (52)$$

In Equation (52), e is electron charge, v is the velocity of particle, R represents the surface barrier potential and Θ is a step function to ensure current is only allowed to emit outwards.

Just because an energy state exists, it does not necessarily mean it is occupied all the time. The Fermi distribution gives us the probability that a given energy state will be occupied by a free electron. Multiplying the Fermi distribution by the density of states function, $\rho(E)$, and integrating over all energy above the surface potential gives a more accurate number of free electrons per unit volume per unit energy based on quantum mechanics statistics. Noting that the density of states function can be represented as

$$\rho(E) = \frac{1}{V} \sum_{n,k,s} \delta(E - E_{n,k}) = 2 \sum_{n,k} \frac{d^3k}{(2\pi)^3} \delta(E - E_{n,k}) \quad (53)$$

and J can now be written as

$$J(T) = -e \int_{e(\phi_\mu)}^{\infty} \rho(E) f(E, T) v |R|^2 \Theta(v) dE \quad (54)$$

Using the density of states function for three dimensions and approximating the Fermi-Dirac equation by assuming $\beta(E_k - \mu) \gg 1$ we have

$$J(T) = \frac{-e}{2\pi^2} \left(\frac{2m}{\hbar^2} \right)^{\frac{3}{2}} e^{-\beta\mu} |R|^2 \int_{e(\phi_\mu + \phi_F)}^{\infty} \sqrt{E} e^{-\beta E} v \Theta(v) dE \quad (55)$$

Recognizing that $E = \frac{1}{2} m \mathbf{v}^2 = \frac{1}{2} m (v_x^2 + v_y^2 + v_z^2)$ and $4\pi \mathbf{v} d\mathbf{v} = dv_x dv_y dv_z$, the limits can be changed from $\frac{1}{2} m v_z^2 \geq e(\phi_\mu)$ to ∞ and integrated over all momenta. The result is known as the *Richardson-Dushman formula*[9]:

$$J_z(T) = -\frac{emk_B^2}{2\pi^2 \hbar^3} |R|^2 e^{-\frac{\mu}{k_B T}} \quad (56)$$

Notice that the Richardson-Dushman formula is a function of temperature T and surface chemical potential μ . For a large thermionic emission, the surface chemical potential must be small and temperature must be high.

Often to decrease the surface chemical potential, thin layers of low work function materials are used to coat emission surface of cathodes. Materials like cesium or other alkali metals have been used in the past to lower the work functions for thermionic emission cathodes.

Using monolayer coverage on metals, the dipoles that are formed by the transfer of electrons from the individual Cs atoms are very strong. The surface dipoles experience strong electric fields due to neighboring dipoles and the direction of these electric fields can reduce the dipole moments. It has been shown in certain semiconductors such as GaAs, depositing Cs can actually make the work function negative [9].

5.3 PRINCIPLES OF FIELD EMISSION

Field emission is a quantum mechanical phenomena that occurs when an electron tunnels through a reduced surface potential from a static electric field. This can be pictured by Figure 53.

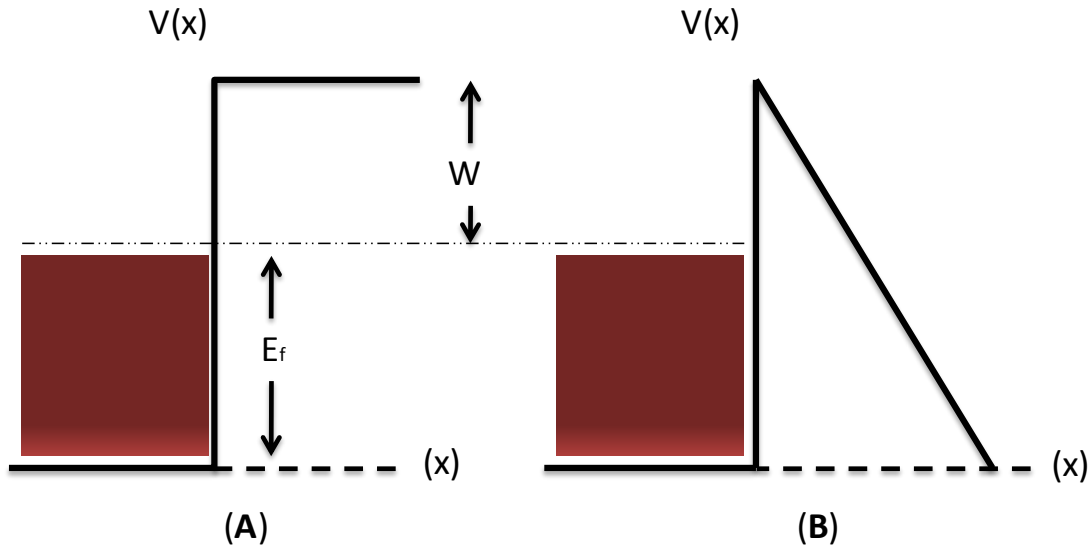


Figure 53. Potential barrier field emission (A) without and (B) with an imposed electric field.

With an incident electric field D , the potential can be written as

$$V(x) = \begin{cases} 0 & x < 0 \\ V - eDx & x > 0 \end{cases} \quad (57)$$

Applying this potential into the one dimensional Schrödinger equation,

$$-\frac{\hbar^2}{2m} (d^2 \phi(x)/dx^2) + V(x)\phi(x) = E\phi(x) \quad (58)$$

the wave function in both regions can be solved. For the $x < 0$ case, the solution is described by

Equation (59), where B is the reflection amplitude

$$\phi(x) = e^{ik_x x} + B e^{-ik_x x} \text{ where } k_x = \left(\frac{2mE}{\hbar^2}\right)^{\frac{1}{2}} \quad (59)$$

For the case of $x > 0$, the Schrödinger equation is slightly more complex

$$-\frac{\hbar^2}{2m} (d^2 \phi(x)/dx^2) + (V - eDx)\phi = \frac{\hbar^2 k_x^2}{2m} \phi \quad (60)$$

By making the substitution of

$$u = \left(\frac{2m}{\hbar^2 D^2}\right)^{1/3} \left(V - Dx - \frac{\hbar^2 k_x^2}{2m} \right) \quad (61)$$

the resulting equation becomes a differential equation whose solution is a linear combination of two Airy functions, $Bi(u)$ & $Ai(u)$

$$\frac{d^2 \phi}{du^2} - u\phi = 0 \quad \phi_{II}(u) = N\{Bi(u) + iAi(u)\} \quad (62)$$

where the Airy functions and their derivatives are

$$Ai(u) = \frac{1}{2\sqrt{\pi} u^{\frac{1}{4}}} e^{\left(\frac{-2}{3u^{3/2}}\right)}, \quad Ai'(u) \propto \frac{-1}{2\sqrt{\pi}} u^{\frac{1}{4}} e^{\left(\frac{-2}{3u^{3/2}}\right)} \quad (63)$$

$$Bi(u) = \frac{1}{\sqrt{\pi} u^{-\frac{1}{4}}} e^{\left(\frac{-2}{3u^{3/2}}\right)}, \quad Bi'(u) \propto \frac{1}{\sqrt{\pi}} u^{\frac{1}{4}} e^{\left(\frac{-2}{3u^{3/2}}\right)} \quad (64)$$

Due to continuity, the following conditions must be made true

$$\phi_I(x=0) = \phi_{II}(x=0) \quad (65)$$

$$\phi_I'(x=0) = \phi_{II}'(x=0) \quad (66)$$

Taking into account Equations (59) and (62), we can solve Equations (64) and (65) for the normalization constant N

$$N = \frac{2ik_x \sqrt{\pi} e^{\frac{-2}{3u_o^{3/2}}} R^{-3/2}}{(ik_x/u_o^{1/4}) - Du_o^{\frac{1}{4}}(2m/\hbar^2 E^2)^{1/3}} \quad (67)$$

where $u_o = \left(\frac{2m}{\hbar^2 D^2}\right)^{1/3} \left(V - \frac{\hbar^2 k_x^2}{2m} \right)$ and R^3 is the volume of the metal. Using Equation (62) with

the solved normalization constant, the current density can be calculated as

$$J = \frac{e\hbar}{m} \operatorname{Im} \left(\phi^* \frac{d\phi}{dx} \right) = \frac{e\hbar D |N|^2}{m} \left(\frac{2m}{\hbar^2 D^2} \right)^{\frac{1}{3}} \quad (68)$$

This current is a function of the incident electric field \mathbf{D} . To get a complete answer the current density must be summed over all energies that are able to penetrate the potential barrier. Making the substitution $V \approx E_f + \mu$, we have

$$J = \frac{2me}{\pi^2 \hbar^3 (E_f + \mu)} \int_{-\infty}^{E_f} dE (E_f - E) \sqrt{E (E_f + \mu - E)} e^{-\frac{4\sqrt{2m}}{3D\hbar} (E_f + \mu - E)^{3/2}} \quad (69)$$

Finally, the total current I is attained, also known as the Fowler-Nordheim formula

$$I = \frac{e^3 D^2}{4\pi^2 \hbar (E_f + \mu)} \sqrt{\frac{E_f}{\mu}} e^{-\frac{4\sqrt{2m}\mu^3}{3eD\hbar}} \quad (70)$$

The Fowler-Nordheim formula demonstrates some key features of field emission, the most notably that field emission is not temperature dependent [9]. It also makes the assumptions that electron emission is near the Fermi energy level, the emission surface is flat, and the image charge potential takes on the form $-e^2/16\epsilon_0\pi x$.

5.4 GEOMETRY EFFECTS

Equation 70, the Fowler-Nordheim formula does not explicitly have a term for the actually geometry of the emission surface. However, geometry terms are embedded into the electric field, \mathbf{D} . To see the effects of various cathode shapes clearly, a simple demonstration of field enhancement is shown in this section. To increase emission current, local emission surface geometry can be modified to enhance the local electric field. To demonstrate field enhancement due to geometry a three-dimensional case similar to the one example by Kosmahl [10]. Starting with an ellipsoidal surface defined by Equation (71),

$$\frac{x^2}{a^2} + \frac{y^2}{b^2} + \frac{z^2}{c^2} = 1 \quad (71)$$

and assuming that the surface of the ellipse is equipotential. The electric field in between the two plates can be solved by satisfying the Laplace equation for the electric potential together with appropriate electric field boundary conditions

$$\nabla^2 \Phi = 0 \quad (72)$$

Making the assumption that c is the largest axis and two minor axes are set to be equal, $a=b$, the problem can be converted into a coordinate system that can be described as a prolate spheroidal system. The transformation from rectangular coordinates (x,y,z) can be made to a new coordinates basis (ξ, η, ϕ)

$$x = a \sinh \xi \sin \eta \cos \phi \quad (73)$$

$$y = a \sinh \xi \sin \eta \sin \phi \quad (74)$$

$$z = a \cosh \xi \cos \eta \quad (75)$$

The Laplacian in the prolate spheroidal system becomes,

$$\nabla^2 \Phi = \frac{1}{(\sin^2 \eta + \sinh^2 \xi)} \times \left[(\csc^2 \eta + \operatorname{csch}^2 \xi) \frac{\partial^2 \Phi}{\partial \phi^2} + \cot \eta \frac{\partial \Phi}{\partial \eta} + \frac{\partial^2 \Phi}{\partial \eta^2} + \coth \xi \frac{\partial \Phi}{\partial \xi} + \frac{\partial^2 \Phi}{\partial \xi^2} \right] \quad (76)$$

Equation 29 can further be simplified by assuming that the $\partial/\partial \phi$ terms equal 0 since we are only looking for the constant Φ surfaces. The solution to Laplace equation becomes a combination of Legendre functions that are dependent on the ellipsoidal shape. The solution becomes [11]

$$\Phi(\xi, \eta) = \frac{kV_0 \xi \eta}{d} \left(1 - \frac{\frac{1}{2} \ln \frac{\eta + 1}{\eta - 1} - \frac{1}{\eta}}{\frac{1}{2} \ln \frac{\vartheta + 1}{\vartheta - 1} - \frac{1}{\vartheta}} \right) \quad (77)$$

where $\vartheta = c/k$, c is the constant ξ converted back into rectangular coordinates, and

$k^2 = c^2 + a^2$. V_0 is the potential across the two plates and d is the distance between the electrodes.

To calculate the actual field enhancement factor, the ratio of average field V_0/h is compared with $d\Phi(\xi, \eta)/dz$. Simplifying this results, the equation (78) for field enhancement factor β is

$$\beta \approx \frac{2c/\rho}{[\ln(4c/\rho) - 2]} \quad (78)$$

where $\rho^2 = b^2 - c^2$, or the radius of curvature of the ellipsoid. In general, (c/ρ) can be considered as the aspect ratio of the device (carbon nanotube).

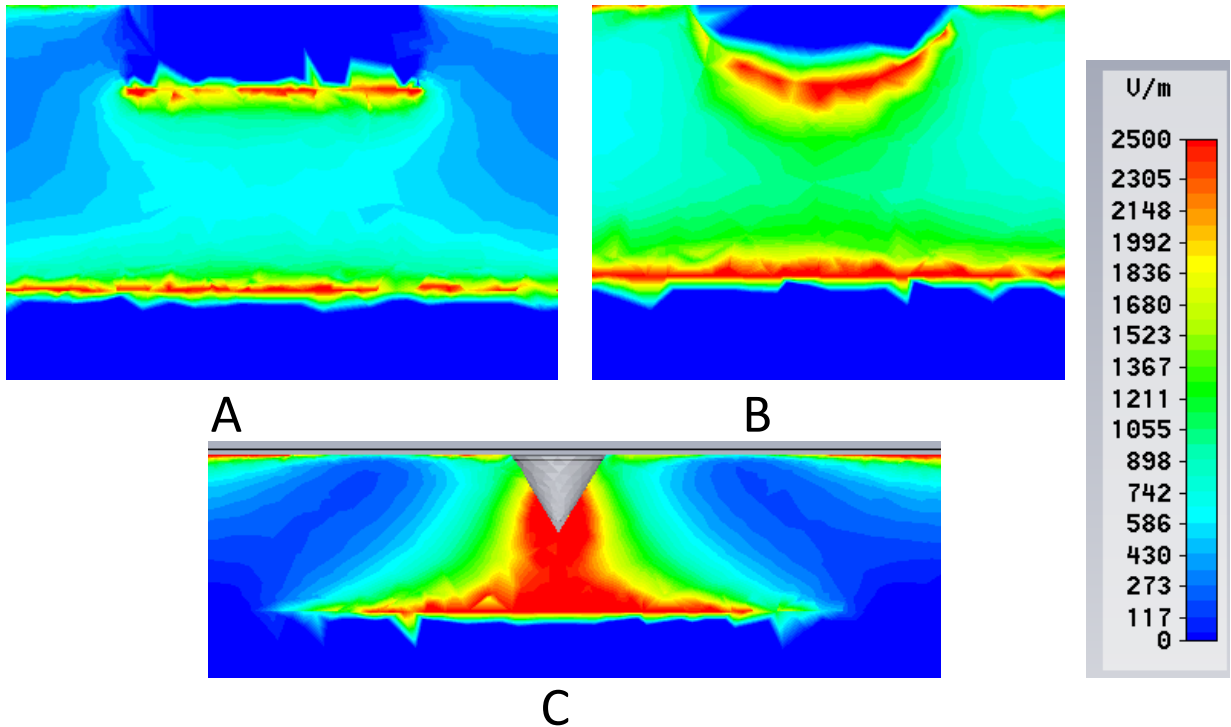


Figure 54. 2-D absolute E-field values for three different geometries. (A) Flat rectangular surface, (B) curved surface of radius R, and (C) cone

Figure 54 represents a computer simulation of electric field intensity for different geometry of cathode from the flat surface (Figure 54A) to the sharp cone (Figure 54C) imitating different aspect ratio for carbon nanotubes. Using the DC electrostatics package of CST Microwave Studio, geometries were constructed from perfect electrical conductor. There were held a fixed

distance from a ground plane. A potential was then applied to the cathode and field lines were modeled by the software. The conclusion is field lines tend to condense around sharp edges. Therefore, a cathode that is tapered like a cone will have the high field enhancement factor.

5.5 FIELD EMISSION RESULTS

The field emission setup is located at AFRL in Wright Patterson AFB. A rough schematic of the test chamber is shown in Figure 55.

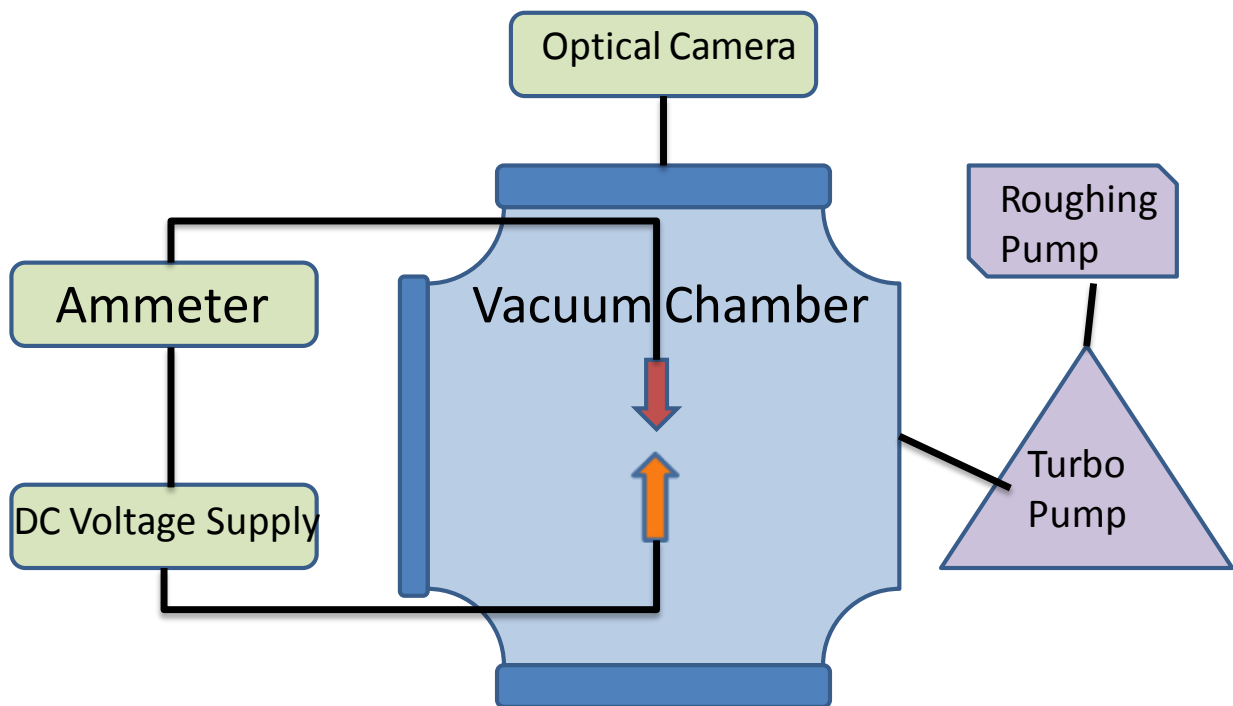


Figure 55. Schematic of field emission chamber set-up.

The chamber is sealed and hooked to a turbo-pump to ensure ultra high vacuum during testing. The anode and cathode are connected to external systems to measure current as a function of voltage applied. The anode is staged on electronically controlled motor which allows accurate stepping in one direction approximately $5 \mu\text{m}$. In addition, a camera is focused onto the cathode for live images of the field emission process. Previous studies have been conducted on

CNT material grown on SiC. Figure 56 depicts field emission results of CNT decomposed from annealing 4H-SiC 1700⁰ C under 10⁻³ Torr for 3 hours (Figure 57). From each consecutive run there was a drastic change in current density [20]. This could be explained by the presence of absorbed impurities on the surface of the carbon nanotube film.

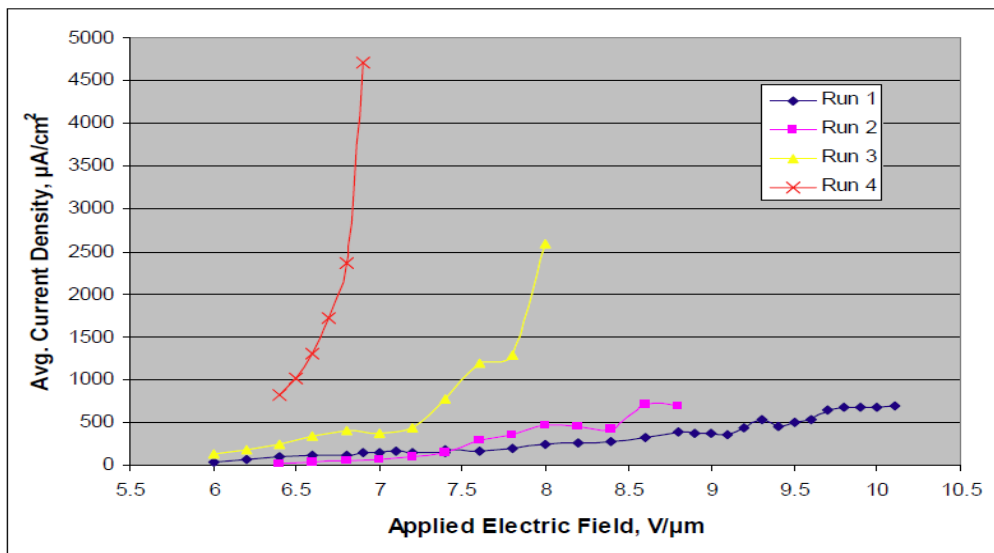


Figure 56. Field emission of CNT film [20].

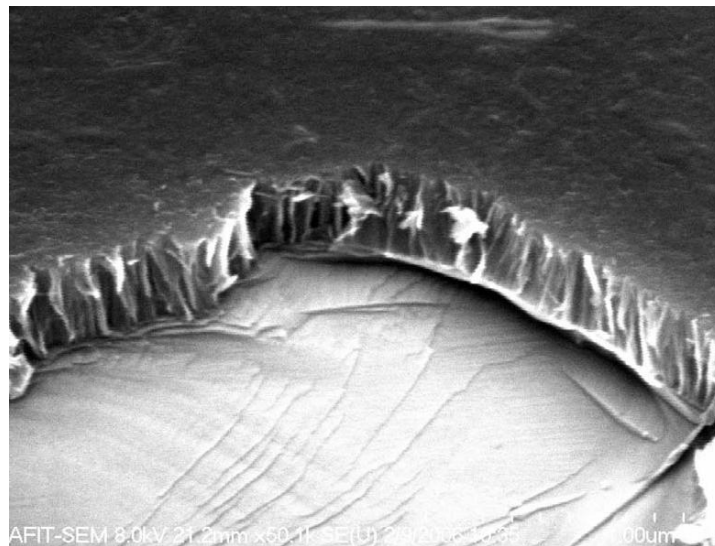


Figure 57. SEM of CNT film grown at 1700⁰C under 10⁻³ Torr for 3 hours [20].

The one of the main focus of this thesis from experimental point of view was to find carbon material with the best field emission properties. High quality CNT material were used with the intent of stable and repeatable emission patterns. Rice SWNT fiber with a radius of about 85 μm was made using Rice's super acid spinning technique. This technique creates a fiber with uniform thickness and no residual iron or sulfur catalysts. Because of this, Rice fibers should exhibit much higher current densities than SiC CNT films.

All Rice fibers were mechanically clipped to create a flat surface and initial conditioning was performed to ensure standardized measurements. This initial conditioning consisted of a three hour voltage ramp from 0 V to 1000 V, with 1 hour dwell at 1000 V and three hour ramp down to 0 V. These fibers were all about 1 cm long and mounted on copper impregnated graphene pucks. A small hole was drilled into the puck and the fibers were threaded through the hole and cemented into place using silver paste. In Figure 58, SEM image represents a fiber mounted on a graphite puck. The shiny reflections are silver paste.

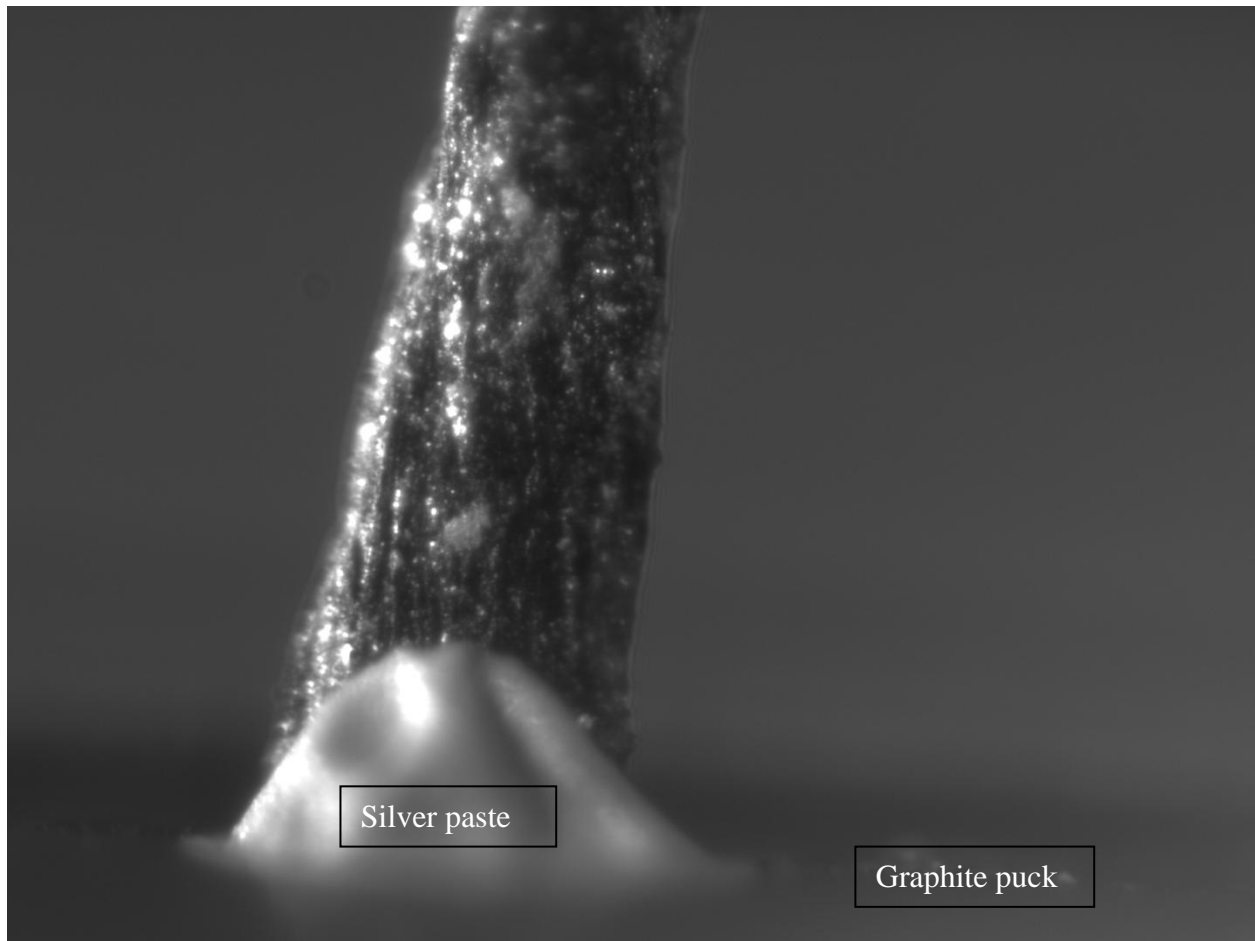


Figure 58. Image of SWNT fiber mounted on a graphite puck.

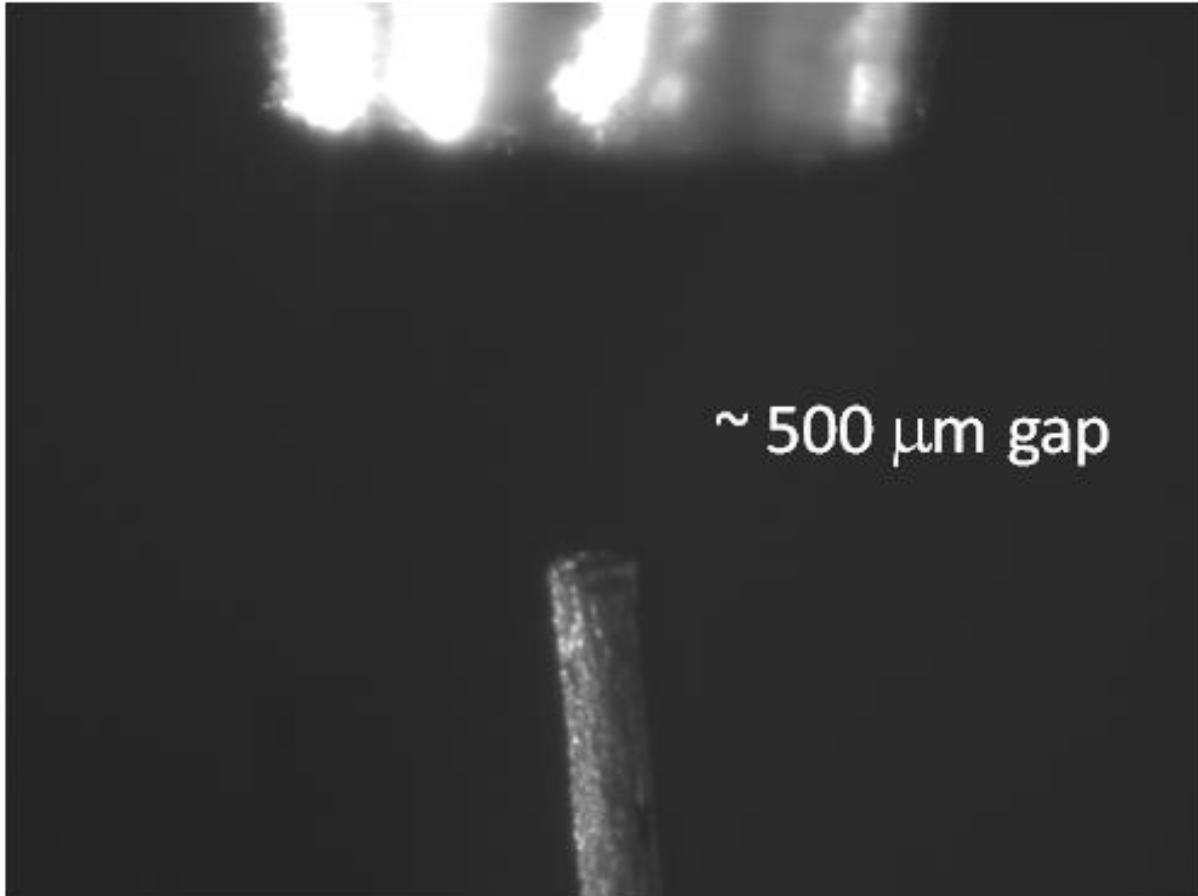


Figure 59. SWNT Rice fiber in field emission chamber. The fiber is placed about 500 μm from anode.

A SWNT Rice fiber with the diameter of about 85 μm is tested with an anode spacing of about 500 μm . Figure 60 and Figure 61 should show this fiber is capable of having high field emission currents. At 1000 V maximum current reached was 200 μA . However, current during the dwell period was not constant and declined significantly.

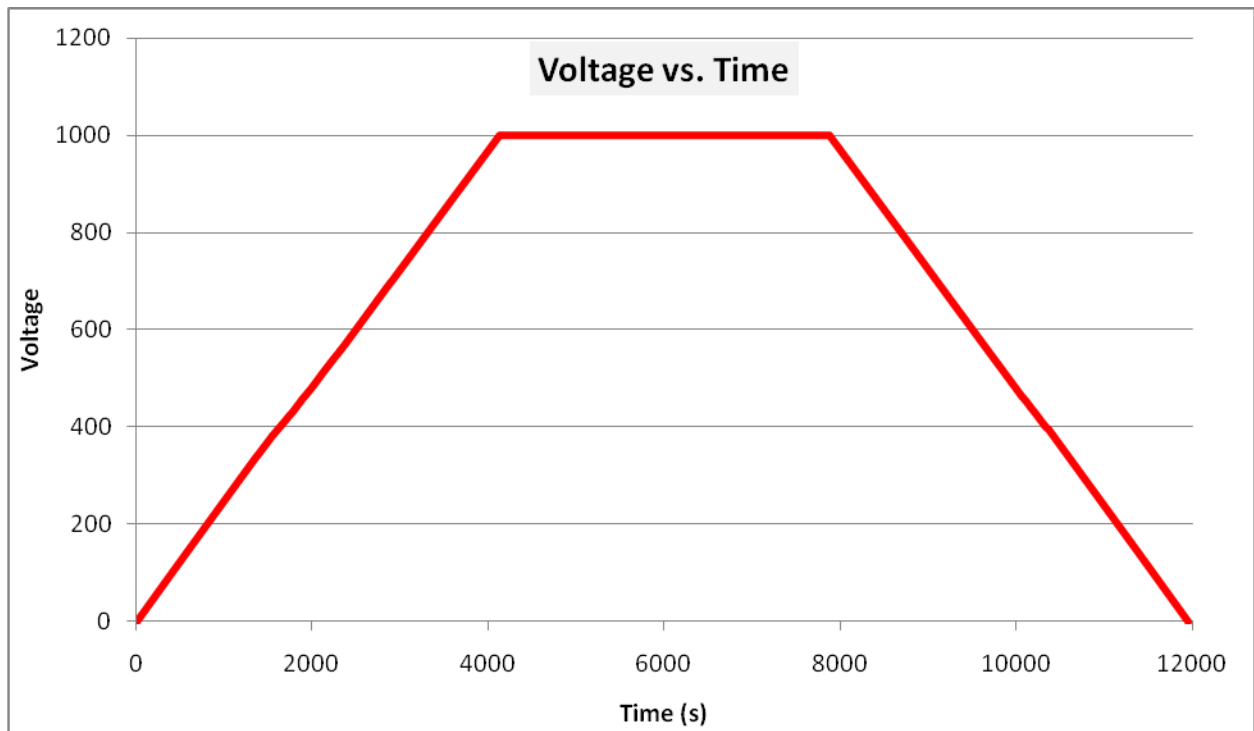


Figure 60. Voltage vs. time of SWNT Rice fiber test with a 500 μm gap distance.

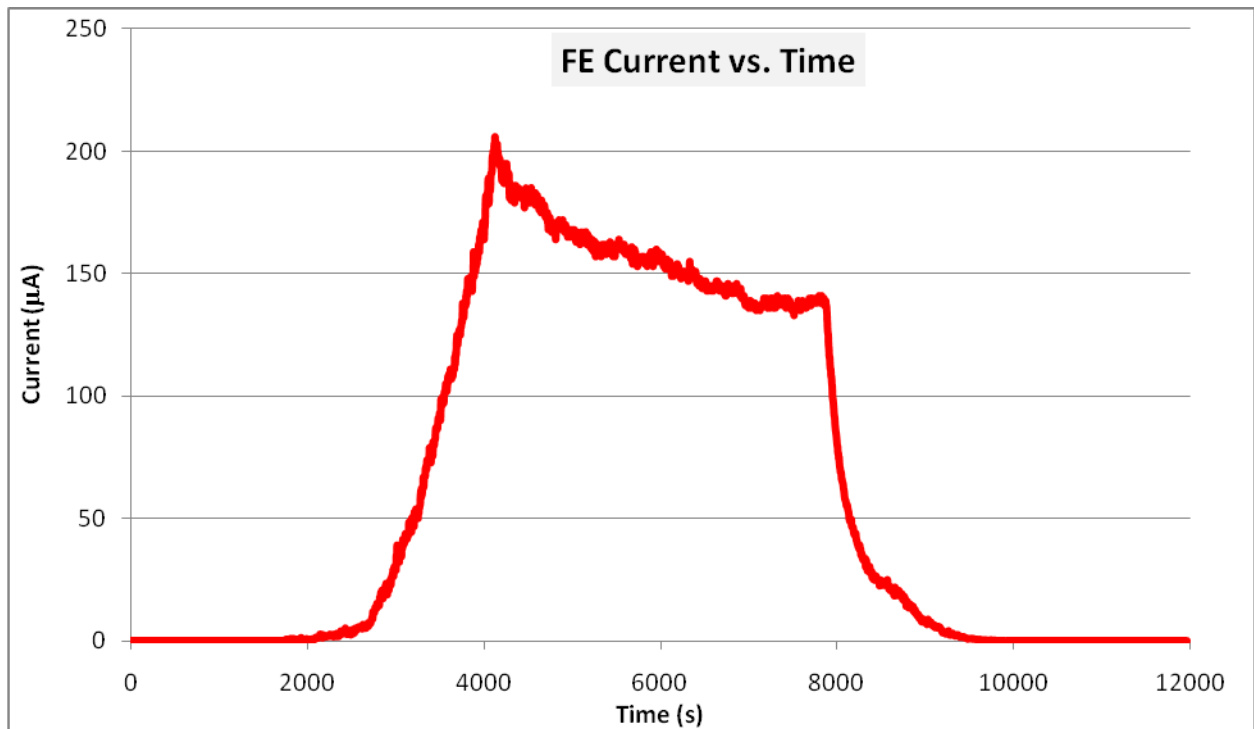


Figure 61. Field emission current vs. time of SWNT Rice fiber test a 500 μm gap distance.

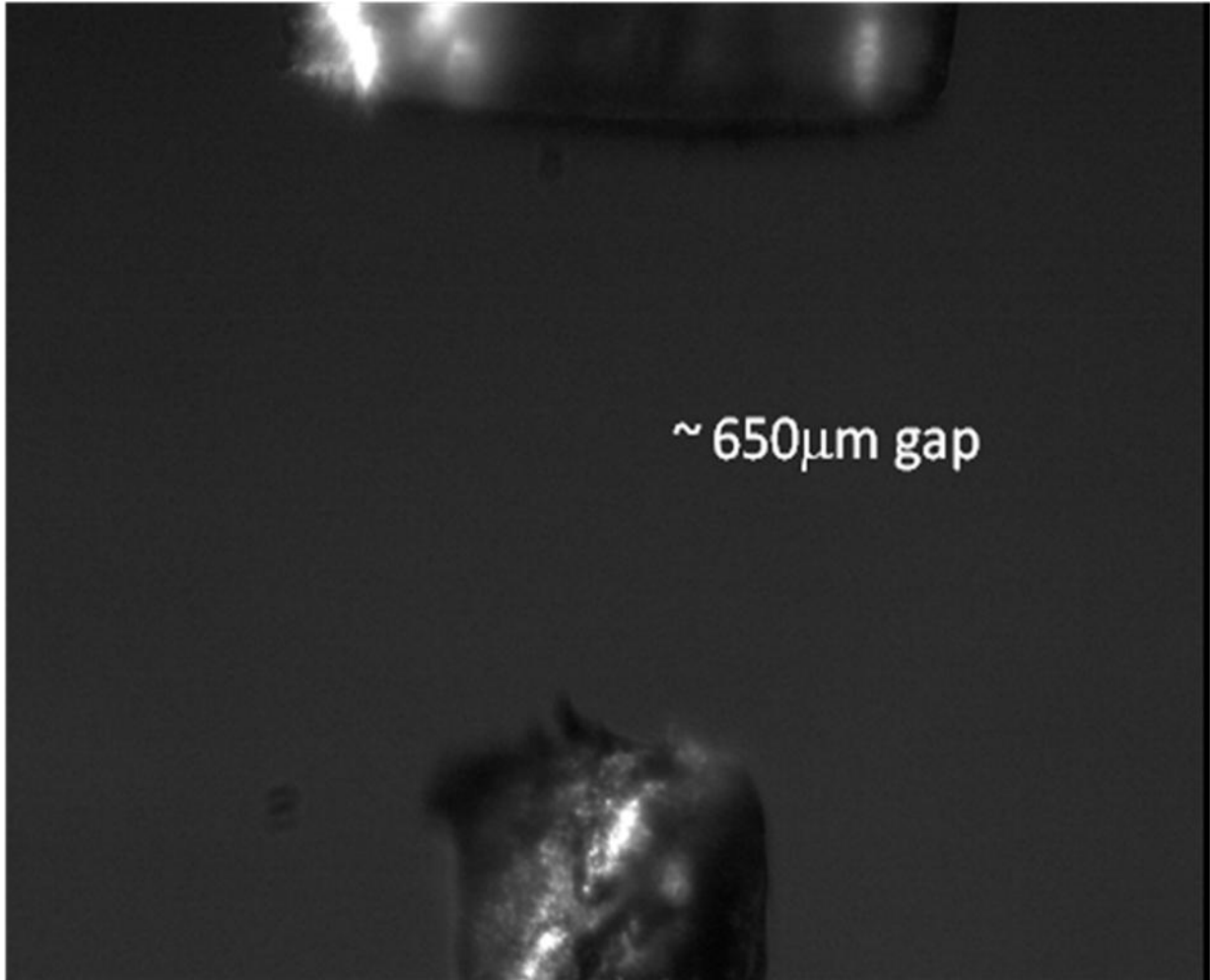


Figure 62. MWNT Cambridge fiber in field emission chamber. The fiber is placed about 650 μm from anode.

To make an accurate comparison in SWNT Rice fiber, MWNT Cambridge fiber should be about the same diameter and the same gap distance. However, due to current limitations of the equipment these measurements could not be taken. The anode used in these experiments was constructed from copper and shaped to a 750 μm tip. With excessive currents plasma formation on the anode jeopardized accurate current measurements. MWNT Cambridge fiber at the same fiber radius over-saturated the amp-meter at gap distance 650 μm (Figure 60 and Figure 61). Even at a gap distance 60% greater, MWNT Cambridge fiber generated a higher average current density than SWNT Rice fiber.

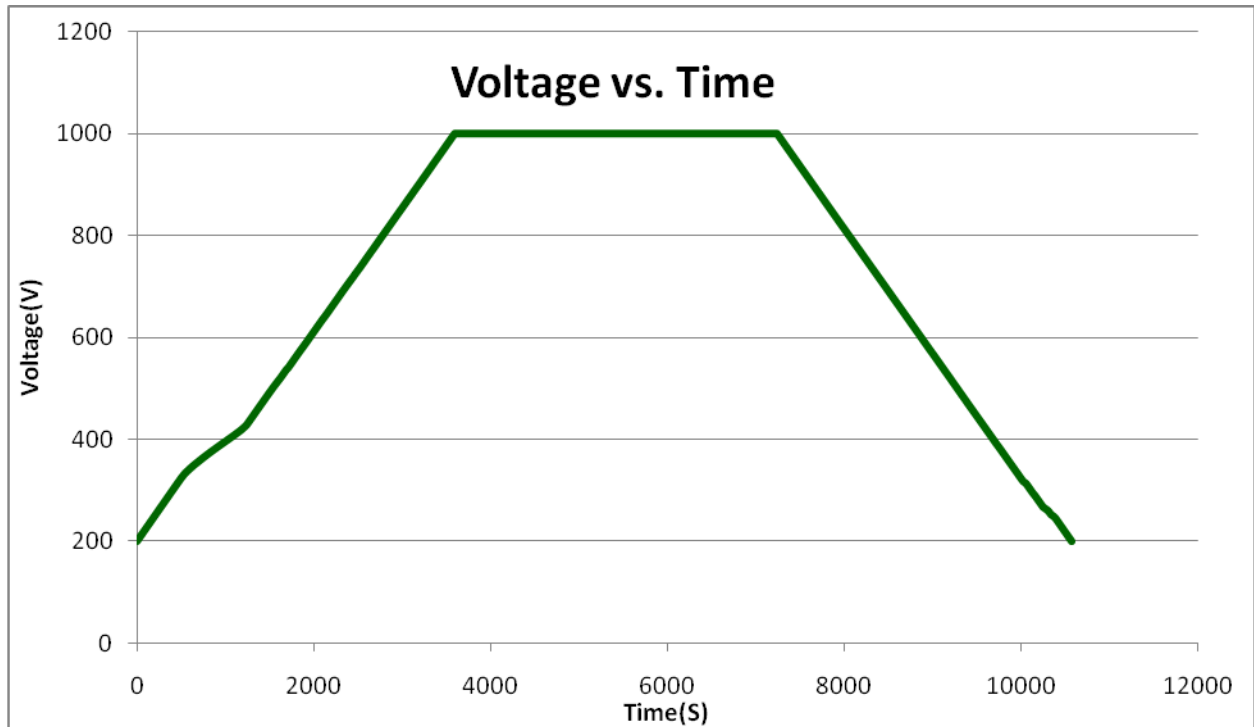


Figure 63. Voltage vs. time of MWNT Cambridge fiber test with a 650 μm gap distance.

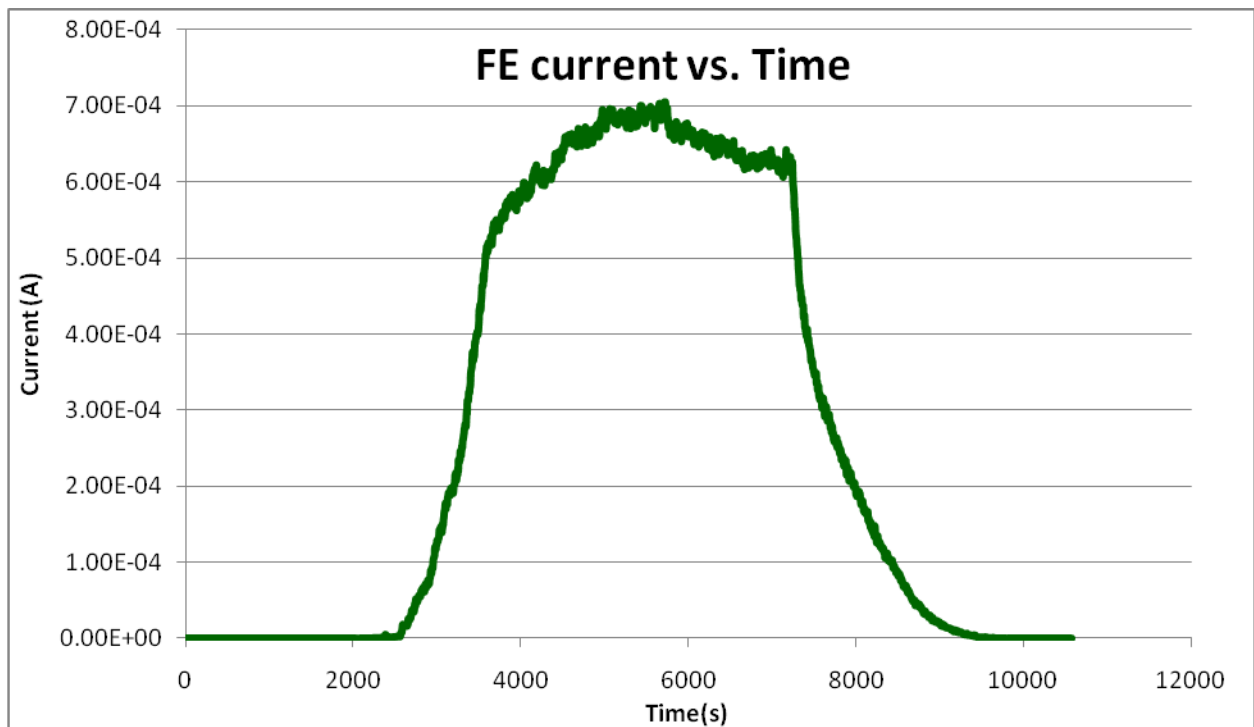


Figure 64. Field emission current vs. time of MWNT Cambridge fiber test with a 650 μm gap distance.

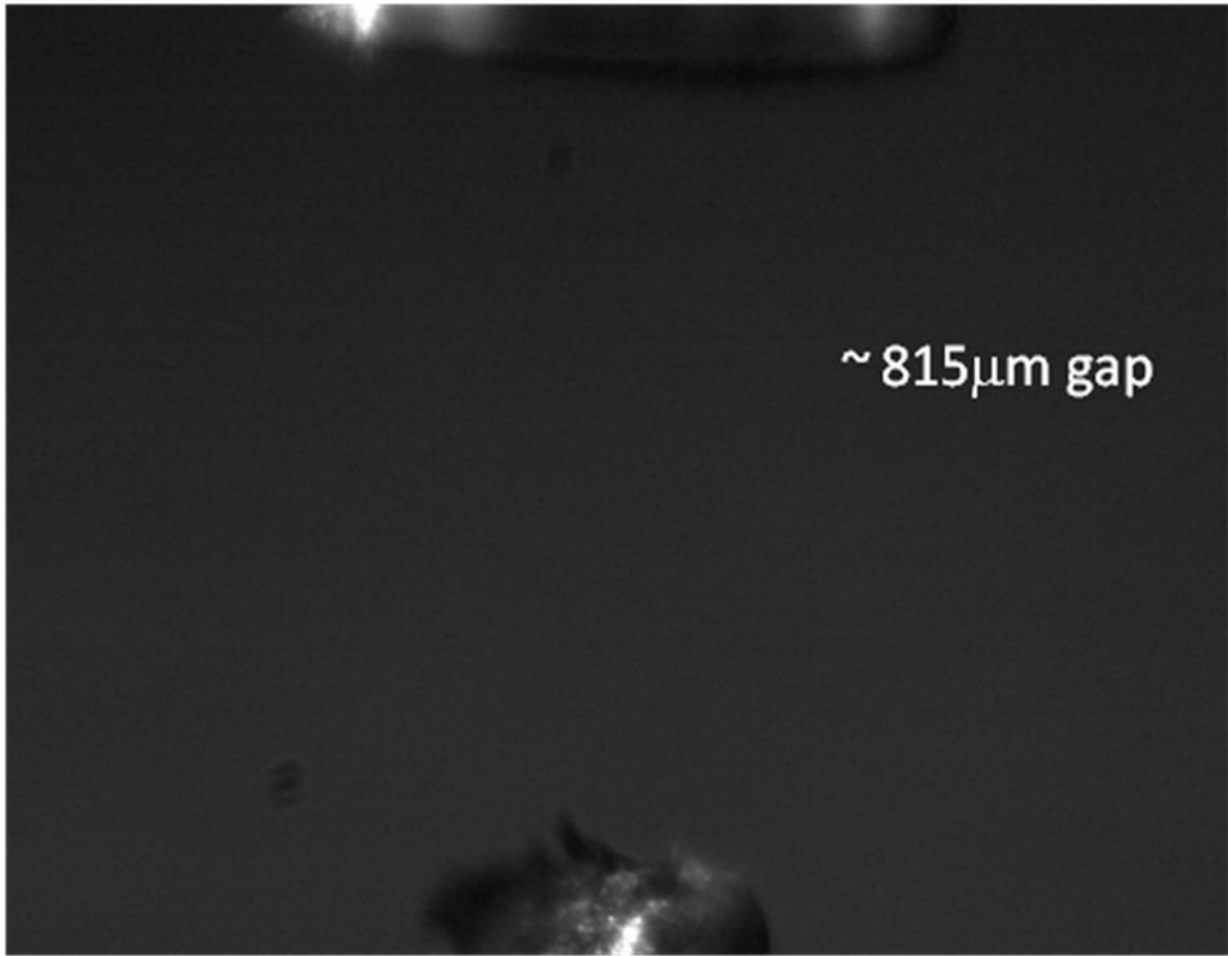


Figure 65. MWNT Cambridge fiber in field emission chamber. The fiber is placed about 815 μm from anode.

MWNT Cambridge fiber was also placed in emission chamber (Figure 65) at the distance 815 mm from anode and tested with respect to its emission capability. The results of these measurements are presented in Figure 66 and Figure 67.

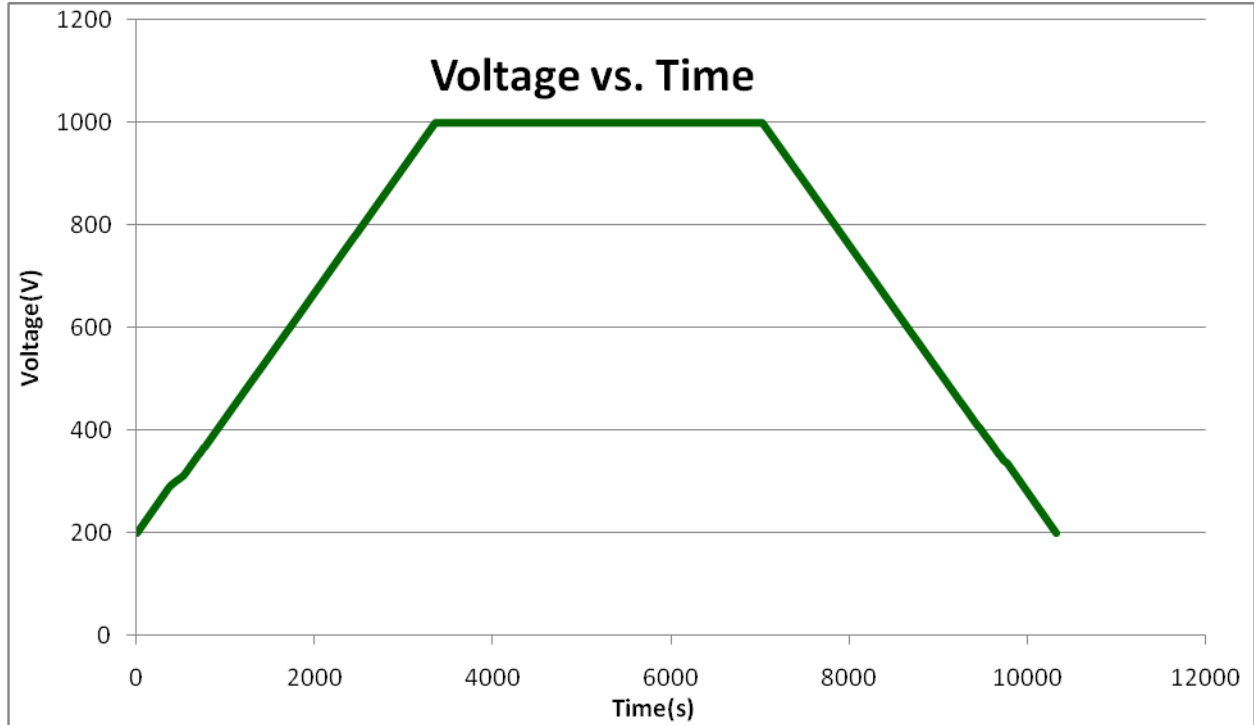


Figure 66. Voltage vs. time of MWNT Cambridge fiber test with an 815 μm gap distance.

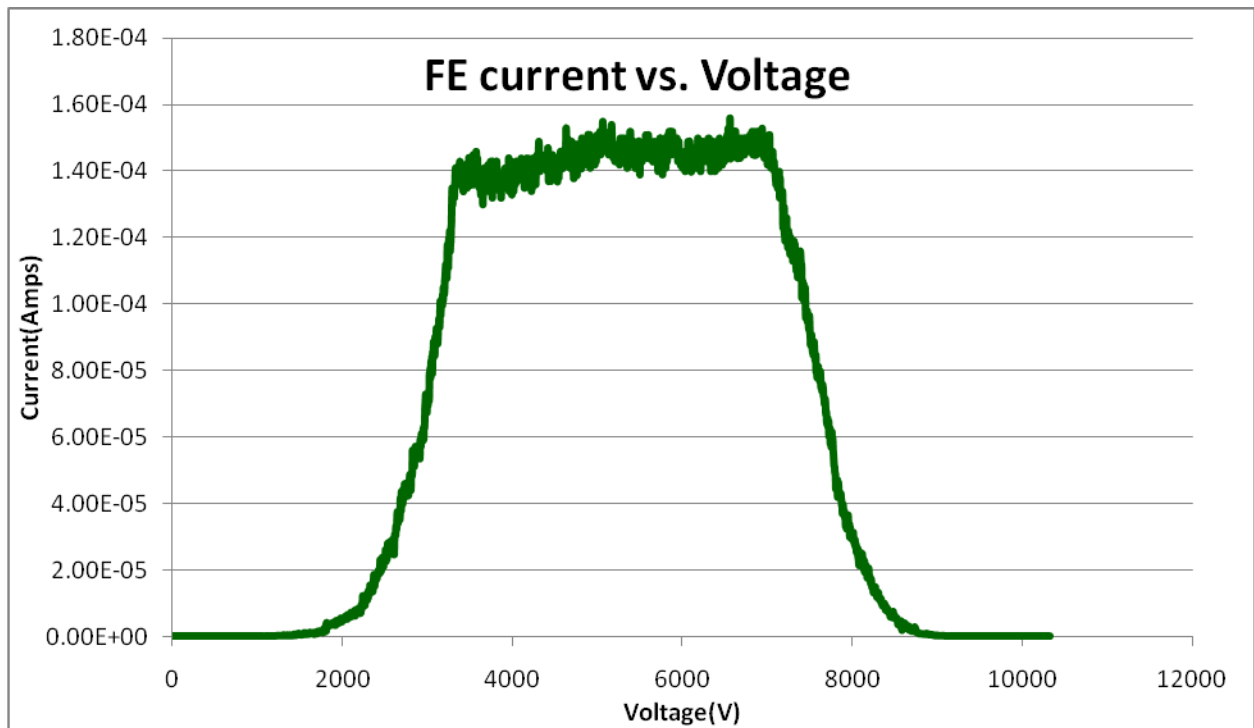


Figure 67. Field emission current vs. time of MWNT Cambridge fiber test with an 815 μm gap distance.

On the other hand, MWNT Cambridge fiber showed relatively stable current during dwell periods (Figure 68 and Figure 69) in contrast to SWNT Rice fiber.

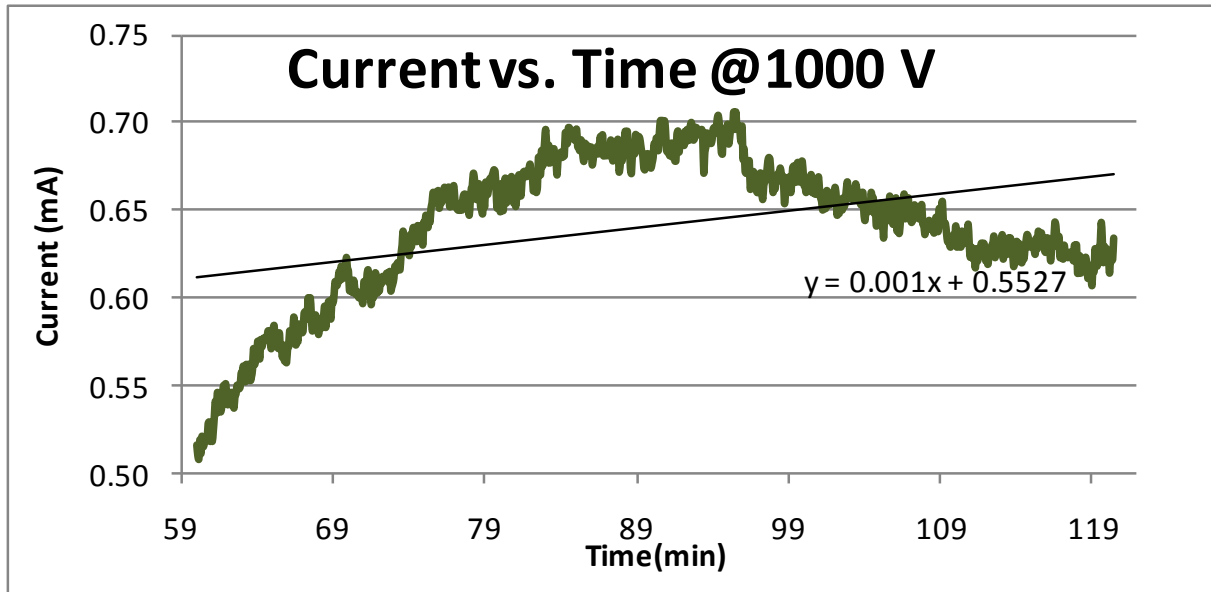


Figure 68. Current vs. time of MWNT Cambridge fiber field emission 615 μm at 1000 V.

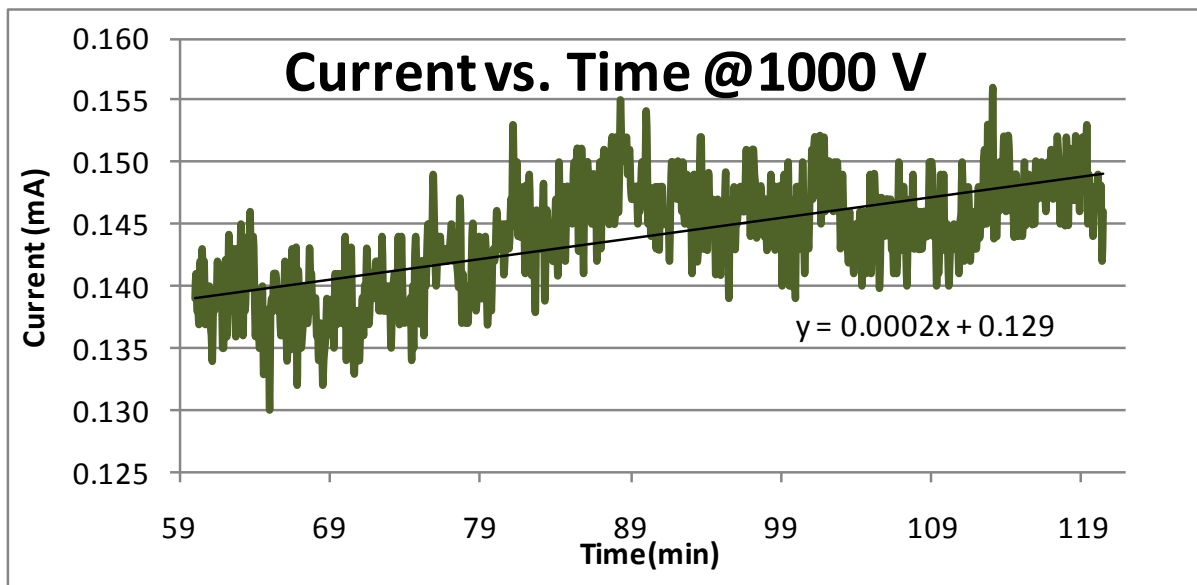


Figure 69. Current vs. time of MWNT Cambridge fiber field emission 815 μm at 1000 V.

In addition, morphology of the fiber tip after clipping and alignment of carbon nanotubes in MWNT Cambridge fiber is depicted in Figure 70.

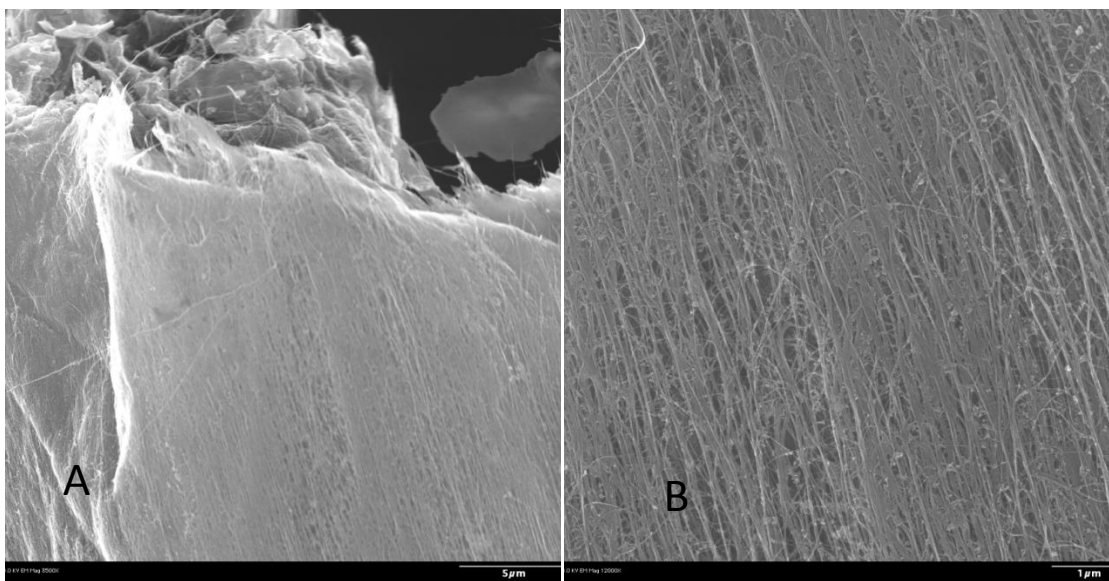


Figure 70. SEM of MWNT Cambridge fiber. (A) Fiber tip after mechanical clipping and (B) alignment of CNTs in fiber.

An interesting feature of the AFRL chamber set-up is the utilization of an optical camera to optically record the fiber in-situ during field emission. Images of the field emission showed evidence of localized field emission sites. Small areas of fiber tips under high voltages began to glow. These glowing areas changed during testing cycle, giving evidence of percolation of field emission sites. These images show fibers that “glow” (Figure 71). The images were taken with the room light on but the image in Figure 71D was taken with the room light off.

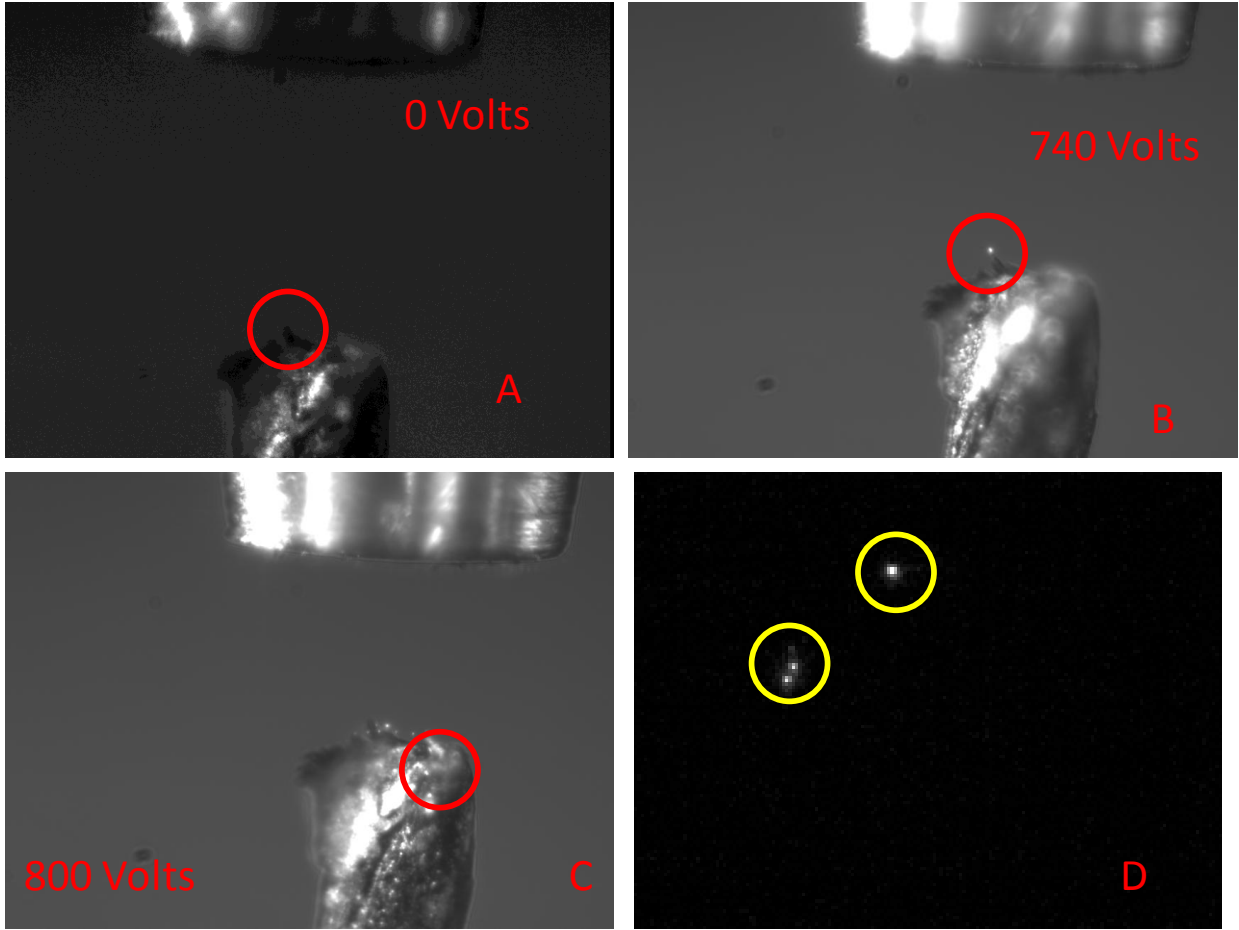


Figure 71. Live images of field emission process.

CHAPTER 6: CONCLUSION

Optimization of silicon carbide decomposition to generate graphene or carbon nanostructures was studied. The formation of tightly packed and vertically arranged carbon nanotubes structures or graphene sheets were achieved by decomposition of SiC single crystal substrates (wafers) at elevated temperatures (above 1600⁰C) in argon atmospheric pressure or in vacuum. Prior to this decomposition, a standard cleaning process of SiC wafer's surface called RCA treatment was applied. Some spherical particles (the most likely heavy metal impurities) have been seen still after treatment on the surface of SiC but there were easily removed by subjecting SiC wafer to the high temperature annealing (700⁰C) in argon atmosphere for 1 hour. Our research initially concentrated on nanoscale control of wafer surface topology. It appears that small thermal fluctuations during growth process can create steps and terraces on SiC surface (step bunching phenomenon). To avoid the step bunching, a planarization process of SiC wafer was done called chemical mechanical polishing (CMP) to guarantee a decrease in the step length and an increase in the terrace length on the surface of SiC wafer. After initial RCA cleaning steps of wafer, a decomposition of non-CMP silicon carbide took place at different temperatures 1300⁰C, 1500⁰C and 1700⁰C. Uniform graphene layers were observed when epi-growth nitride mask was applied subjected to temperatures above 1600⁰C in argon atmosphere. In turn, carbon nanotubes were seen when SiC single crystal substrate was annealed without mask at 1700⁰C under high vacuum. CMP treated silicon carbide wafers showed to have high quality graphene growths measured by increased domain sizes and uniformity of material. Various physical characterization techniques were used to study effects of temperature, pressure and surface treatments on carbon nanomaterials growths.

In addition, optimization of carbon nanotubes grown from the “Cambridge” process was presented. It is shown through evanescent microwave spectroscopy as well as optical spectroscopy measurements that temperature annealing MWNT Cambridge fibers up to 500⁰C in argon will have the same effect on local electrical properties of CNT materials. In Figs. 48-50, measurements of pre and post annealed MWNT Cambridge fibers show that the relative Q-factor and reflectance of the fibers decrease after annealing. It suggests that a surface conductivity of fibers decreases which is confirmed by I-V curve measurements (an increase in resistance of fiber shown in Figure 22). One of the possible explanations of this behavior is a removal of oxygen and water from the sample due to temperature annealing.

The main goal of our studies was primarily to optimize growths and corresponding post treatments to achieve the highest performing materials for practical applications. The graphene device presented in the EBIC study is a device constructed using optimized growth techniques discussed in Chapter 4. The device is intended to be a sample device to study the quantum Hall effect. In addition, initial studies using EBIC spectroscopy show some interesting results on the effects of irregular graphene growths. Physical deformations can easily be seen by an SEM on the surface of a graphene device. However, physical deformations may not correspond to electric barriers. In Figure 49, SEM micrograph shows clearly a physical surface defect, however, different intensities on the EBIC indicate that the surface defect may not correspond to site of electric defects. Correlation between electric and physical deformation will improve the quality of future graphene based devices. Future studies must be done to translate the EBIC data into information characterizing the carrier properties in graphene.

The focus in the case of carbon nanotube materials was to study their field emission properties. As summarized in Table IV, a drastic improvement of field emission current was

found for MWNT Cambridge fiber when compared to SWNT Rice fiber measurements (see Figure 60). On the initial stage of our studies, field emission from silicon carbide decomposed carbon nanotubes was measured (Figure 56). However, these studies show the inconsistencies of current densities from consecutive tests.

CNT fiber, similar to the MWNT Cambridge fibers, has a higher potential of scalability into high power applications. Even with poor fiber condensation, and high level of growth catalysts, MWNT Cambridge fibers outperformed the SWNT Rice fibers (see Table IV). The MWNT Cambridge fibers can be further optimized in future studies. Future field emission studies of Cambridge MWNT has been given additional funding based off results presented in this thesis.

Table IV. Summary of field emission results.

	Current Density (mA/cm ²)	Description
SiC CNT	5.00	1000 V at 150 μm gap
Rice SWNT	8.81	1000 V at 500 μm gap
Cambridge MWNT	30.84	1000 V at 615 μm gap
	7.05	1000 V at 815 μm gap

REFERENCES

1. Dresselhaus, M., 2002, Raman Spectroscopy on Isolated Single Wall Carbon Nanotubes, *Carbon* 40: 2043-2061.
2. Ericson, L.M., 2004, Macroscopic, Neat, Single-Walled Carbon Nanotube Fibers, *Science* 305: 1447-1450.
3. Huang, S., Woodson M., Smalley R., Liu J., 2004, Growth Mechanism of Oriented Long Single Walled Carbon Nanotubes Using “Fast-Heating” Chemical Vapor Deposition Process, *Nano Letters* 4: 1025-1028.
4. Kozlov, M.E., Capps R.C., Sampson W.M., Ebron V.H., Ferraris J.P., Baughman R.H., 2005, Spinning Solid and Hollow Polymer-Free Carbon Nanotube Fibers, *Adv. Materials* 17: 614-617.
5. Kusunoki, M., Suzuki T., Hirayama T., Shibata N., Kaneko K., 2000, A Formation Mechanism of Carbon Nanotube Films on SiC (0001), *Applied Physics Letters* 77: 531-533.
6. Saito, R., Fujita M., Dresselhaus G., Dresselhaus M.S., 1992, Electronic Structure of Chiral Graphene Tubules, *Applied Physics Letters* 60: 2204-2206.
7. Yudasaka, M., Komatsu T., Ichihashi T., Iijima S., 1997, Single-Wall Carbon Nanotube Formation by Laser Ablation Using Double-Targets of Carbon and Metal, *Chemical Physics Letters* 278: 102-106.
8. Zhang, S., Zhu L., Minus M.L., Han G., Jagannathan S., Wong C., Kowalik J., Roberson L.B., Kumar S., 2008, Solid-State Spun Fibers and Yarns from 1-mm Long Carbon Nanotube Forests Synthesized by Water-Assisted Chemical Vapor Deposition, *Journal of Materials Science* 43: 4356-4362.
9. Gersten, J.I., Smith F.W., 2001, *The Physics and Chemistry of Materials*, New York: Wiley.

10. Proposal of Field-Emission Device Surrounded by High-k Dielectric and Performance Prospects, *Optics InfoBase*, Kosmahl, H.G., 2011.
<<http://www.opticsinfobase.org/abstract.cfm?URI=jdt-2-3-300>>.
11. Prolate Spheroidal Coordinates from Wolfram MathWorld, *Wolfram MathWorld: The Web's Most Extensive Mathematics Resource*, 2011.
<<http://mathworld.wolfram.com/ProlateSpheroidalCoordinates.html>>.
12. Transformation of a SiC Nanowire into a Carbon Nanotube (DOI: 10.1039/b9nr00163h)." *Royal Society of Chemistry, the Largest Organization in Europe for Advancing the Chemical Sciences*, 2011.
<http://www.rsc.org/delivery/_ArticleLinking/DisplayHTMLArticleforfree.cfm?JournalCode=NR&Year=2009&ManuscriptID=b9nr00163h&Iss=3>.
13. Harrison, J., Sambandam, S.N., Boeckl, J.J., Mitchel, W.C., Collins, W.E., Lu W., 2007, Evaluation of Metal-Free Carbon Nanotubes Formed by SiC Thermal Decomposition, *J. Appl. Phys.*, 101:104311-104315.
14. Koziol, K.K., Research Discussion, 2010.
15. Tungsten Element Design Fabrication Production, Tungsten Heat Zone Components, *High Temperature Inert Gas Vacuum Furnace Manufacturers, Inert Atmosphere Furnace Systems*, 2011.
<<http://www.oxy-gon.com/wmesh.htm>>.
16. Koziol, K.K., Research Discussion, 2010.
17. Eichhorn F., Jepsen P.U., Schroeder N., Kozlowski G., Deibel J.A., Koziol K.K., Scattering of Terahertz Radiation from Oriented Carbon Nanotube Films, *Conference on Lasers and Electro-*

Optics/International Quantum Electronics Conference, OSA Technical Digest (CD) (Optical Society of America, 2009), paper IThC7.

18. Kozlowski, G., Research Discussion, 2010.
19. Kleismit, R.A., Kozlowski, G., Foy, B.D., Hull, B.E., Kazimierczuk, M., 2009, Local Complex Permittivity Measurements of Porcine Skin Tissue in the Frequency Range from 1 GHz to 15 GHz by Evanescent Microscopy, *Phys. Med. Biol.*, 54: 699-713.
20. Characterization of the Field Emission Properties of Carbon Nanotubes Formed on Silicon Carbide Substrates by Surface Decomposition, Pochet, M.C., *OAI*, 2011.
<<http://oai.dtic.mil/oai/oai?verb=getRecord&metadataPrefix=html&identifier=ADA451105>>.
21. Dresselhaus, M., 2002, Raman Spectroscopy on Isolated Single Wall Carbon Nanotubes, *Carbon*, 40: 2043-2061.
22. Bulmer, J., Personal Discussion, 2010.
23. Koziol K.K., Ducati C., Windle A., 2010, Carbon Nanotubes with Catalyst Controlled Chiral Angle, *Chemistry of Materials*, 22: 4904-4911.
24. R.Martel, T.Schmidt, et al., Single- and Multi-Wall Carbon Nanotube field-effect transistors, *App. Phys.Lett.* 73, 2447 (1998).
25. E.D.Minot et al., Tuning Carbon Nanotube Band Gaps with Strain, *Phys.Rev.Lett.* 90, 2003.
26. Liu Yang, Band gap change of carbon nanotubes, *Phys.Rev. B.*, 13874-13878, 1999.